TEMPERATURE SWING ADSORPTION COMPRESSION AND MEMBRANE SEPARATIONS

By

Joseph R. Moate

Dissertation

Submitted to the Faculty of the

Graduate School of Vanderbilt University

in partial fulfillment of the requirements

for the degree of

DOCTOR OF PHILOSOPHY

in

Chemical Engineering

December, 2009

Nashville, Tennessee

Approved:

Professor M.Douglas LeVan

Professor Kenneth Debelak

Professor G.Kane Jennings

Professor Bridget Rogers

Professor Greg Walker

To my friends and family,

thanks for all of your support and encouragement

ACKNOWLEDGEMENTS

I would like to extend my heartfelt thanks to my adviser, Prof. Doug LeVan, for without his guidance, never-ending patience, and seemingly inexhaustible knowledge of mathematical methods my research would not have been completed. It was truly a pleasure studying adsorption equilibria as a graduate student in his laboratory and it is impossible to thank him enough for his time and effort. He is without a doubt the best teacher I have ever known and I have learned so much through the graduate school experience because of him.

I want to thank all of the members of my Ph.D. committee for helping guide me through the graduate school experience.

I gratefully acknowledge the financial support of the NASA Ames Research Center. I would also like to thank Bernadette Luna, Lila Mulloth, John Hogan, and Mini Varghese for their help and support of my research.

I owe a huge thanks to the staff in the Department of Chemical Engineering. In particular, Mary Gilleran and Margarita Talavera have been a tremendous source of help throughout my time Vanderbilt.

I am grateful to all the members of the LeVan group for the helpful discussions and great friendships. I appreciate the help of Krista, Yuan, Brian, and Yu in answering countless questions when I first joined the group and helping me get started on my research. I also would like to thank Yu and Brian for their countless help with programming in Fortran as well as Jian, Amanda, and Grant in helping me maintain my sanity.

Finally, no one has supported me more over the course of my graduate work than my family and friends, with their constant encouragement and unwaivering belief in me. I want to thank my parents for always taking the time to listen to me and supporting me in all of my endeavors.

TABLE OF CONTENTS

LIST OF TABLES

LIST OF FIGURES

CHAPTER I

INTRODUCTION

In order for manned-space flight to occur it is necessary to have processes to revitalize the spacecraft's cabin air by removing trace amounts of certain airborne contaminants including CO_2. A process is required to remove the 1 kg produced by an average person under normal activity per day to maintain the amount of CO_2 below 10,000 ppm, the level at which CO_2 becomes toxic. Currently, NASA employs an adsorption process that revitalizes the cabin air aboard the International Space Station (ISS) called the carbon dioxide removal assembly (CDRA).[3]

The CDRA is an open-loop 4 bed molecular sieve (4BMS) with 2 desiccant beds to remove water vapor from the feed stream to prevent reduction of the CO_2 capacity due to water contamination in the adsorbent beds. CO_2 is then removed and vented to space and the water vapor is recuperated from the desiccant beds. This is an effective and well understood system, but as the duration of the missions in space increases it is necessary to develop a more energy efficient system that recovers and converts the CO_2 to O_2.

By adding a Sabatier reactor, the CO_2 can be reacted with hydrogen to form O_2 and methane, thus making the overall air revitalization a closed-loop process in regards to water and O_2.[3] However, in order for the Sabatier reaction to occur, the CO_2 feed stream needs to be approximately 95% pure and at a pressure slightly above atmospheric.

To achieve the feed requirements of the Sabatier subsystem, the existing CDRA would be replaced with a two-stage temperature-swing adsorption compressor (TSAC),[1] which would sequester, concentrate, and pressurize the CO_2 from the cabin environment. The TSA compression subsystem would contain an adsorbent

that preferentially adsorbs CO_2 , such as 5A zeolite or NaY zeolite. An exploded view of the conceptual design of a TSAC is shown in Figure 1.1. The first bed would remove CO_2 from the process stream at a temperature of 25°C and a partial pressure of about 2 mmHg, revitalizing the cabin air. The first stage would then be heated to 200°C , and begin bleeding the sorbent's store of CO_2 to the cool second stage until an equilibrium pressure is reached. Once the second stage equilibrates with the first stage, it is closed off and energy is supplied to the electrical resistance heaters. The second stage, operating as a compressor, would then deliver a supply of CO_2 at 1000 mm Hg to the Sabatier Reactor until a final temperature of 200°C is reached. The design of the two stage subsystem will be such that the desorbing first stage and the producing second stage are thermally coupled to reduce heat losses to the surroundings.[2–4] By using a TSA compressor as opposed to conventional compressors, the number of moving parts would be reduced with the compression of CO_2 relying solely on the physical properties of CO_2 and the adsorbent used.

To reduce the energy requirements of the air revitilization system, it is important to replace the existing desiccant beds in CDRA since the majority of energy required is used to desorb the water. A shell and tube membrane composed of a water selective polymer created by DuPont, i.e., Nafion®, could reduce the volume needed for the desiccant beds thus reducing the energy requirement. Representative membrane modules consisting of a single tube or a bundle of 50 tubes have previously been characterized and validated by Ye and LeVan.[5,6] In their papers, they concluded that a fully hydrated membrane module is capable of removing up to 85% of the water in a tube-side feed stream. This would suggest that the size of residual desiccant beds would only need to be 15% of the size of the desiccant beds currently used, which further suggests a savings of 85% in energy.

A schematic of the suggested integrated membrane and TSAC system is shown in Figure 1.2. The cool moist air supplied by the temperature and humidity control

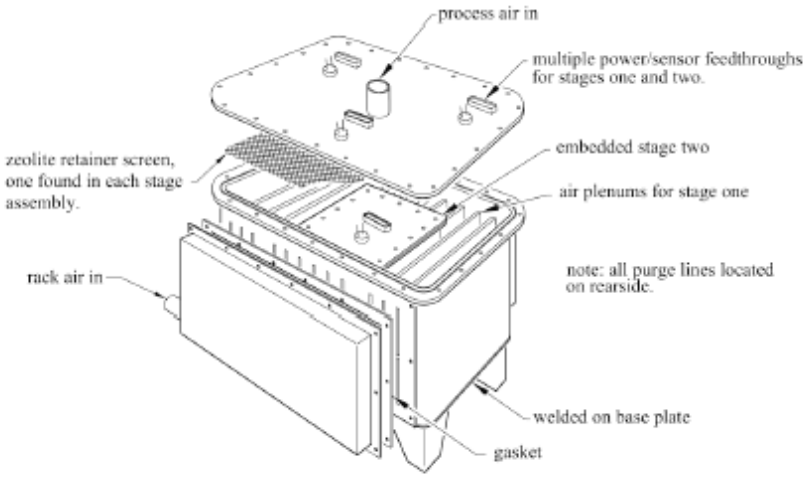

Figure 1.1: Conceptual design of the 2 stage TSA compression subsystem.[3]

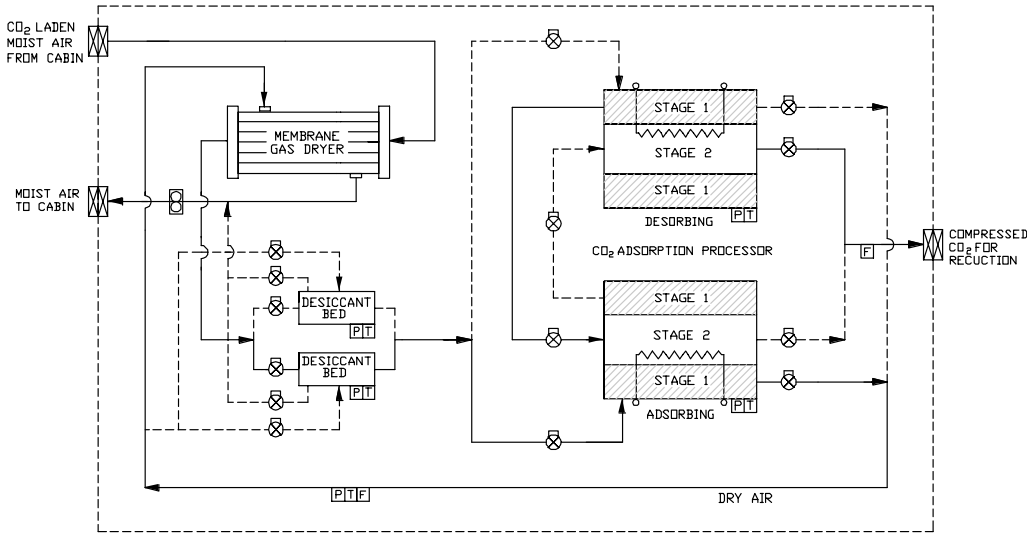

Figure 1.2: Conceptualized schematic of the membrane-integrated CO_2 removal and compression system.[4]

assembly of the spacecraft (this is not shown) enters the Nafion® membrane dryer where 85% of the moisture is removed. The air stream then passes to the desiccant bed, which removes any residual water. Dry air enters stage 1 of the 2 stage adsorption compressor where CO_2 is removed from the process cabin air during a period of 50 minutes. Next a portion of the CO_2-free air stream is pulled back, by means of a vacuum pump, through the shell side of the membrane to be rehumidified before entering the cabin. The other portion of dry air is passed through the residual water adsorber to regenerate the sorbent bed.

The design and optimization of such an adsorption system requires a fundamental quantitative understanding of the adsorption kinetics and dispersive forces

that affect a sorbate's breakthrough behavior. It is common for a plug flow Fickian type model to be used to describe dispersion within a packed bed. However, this does introduce error into the model, since no packed bed has perfect plug flow. By having a better comprehension of the error associated with using plug-flow Fickian models, more rigorous models can be written to better design and optimize adsorption systems.

The objective of this dissertation is to contribute to the design of a new air revitalization system for CO_2 removal and conversion in spacecraft. Results of the research have ground-based applications in development of process improvements for adsorption and membrane devices including enhanced energy efficiencies.

This dissertation is organized as follows. In chapter 2 isotherms are fitted to experimental data for use in sizing a 2-stage TSAC for the capture and pressurization of CO_2 in a packed bed of 5A zeolite, which is then later modeled using Comsol Multi-Physics^{TM}finite element software package. The effects of imbalanced heating loads on the desorption of CO_2 from a packed bed with an expected value of thermal conductivity are investigated in Chapter 3. Chapter 4 examines nonplug flow of a fluid through a packed bed in which a constant pattern wave has developed for an adsorbent with a slightly favorable isotherm. In chapters 6 and 7 the dehydration of a gas stream is analyzed for a shell and tube Nafion® multi-tube membrane module with the shell side exposed to a vacuum and a counter current purge gas, respectively.

References

[1] R.P. Hoover, P. C. Wankat, Gas compression using temperature swing adsorption, Separation Science and Technology 37 (14) (2002) 3187-3199.

[2] L.M. Mulloth, J.E. Finn, A solid-state compressor for integration of CO_2 removal and reduction assemblies, SAE International 2000-01-2352.

[3] L. Mulloth, M. Varghese, B. Luna, J. Hogan, M.D. LeVan, J.R. Moate, Development of a low-power CO_2 removal and compression system for closed-loop air revitalization in future spacecraft, SAE International, Paper 2005-01-2944 (2005) 1-8.

[4] M.S. Rosen, L.M. Mulloth, D.L. Affleck, Y. Wang, M.D. LeVan, Development and testing of a temperature-swing adsorption compressor for carbon dioxide in closed-loop air revitalization systems, SAE International, Paper 2005-01-2941 (2005) 1-6.

[5] X. Ye, M.D. LeVan, Water transport properties of Nafion membranes Part I. Single-tube membrane module for air drying, Journal of Membrane Science, 221 (2003) 147-161.

[6] X. Ye, M.D. LeVan, Water transport properties of Nafion membranes Part II. Multi-tube membrane module for air drying, Journal of Membrane Science, 221 (2003) 163-173.

CHAPTER II

TWO STAGE CO_2 ADSORPTION COMPRESSOR DESIGN AND MODELING

2.1 Introduction

The two-stage CO_2 adsorption compressor is an air revitalization subsystem[6] utilizing the fundamentals of both temperature and vacuum-swing adsorption. The first stage removes CO_2 from the dry process feed stream. The adsorbent bed is then regenerated by being subjected to heat and vacuum, simultaneously feeding the second stage which operates under the principles of temperature swing adsorption (TSA).[4] The second stage is then heated, producing compressed CO_2 regulated by the amount of energy supplied to the adsorbent bed.

TSA compression uses the enthalpy of adsorption to control a sorbent's capacity for the desired separation, compression, and delivery of gases. A TSA adsorbent bed is composed of a material that preferentially adsorbs one component in a process stream. A typical TSA compression cycle, shown in figure 2.1, consists of four stages for the compression of a gas: adsorption, compression, production, and depressurization.

Following the cycle outline in figure 2.1,[7] we begin at a low pressure and low temperature point on an isotherm curve representing a cool regenerated sorption bed. During the adsorption step, a process stream is passed through the bed in which a pure component is selectively adsorbed until the bed is saturated. During this step, the bed is maintained isothermal by a cooling media flowing around it to remove the latent heat of adsorption. When the bed saturates it is closed off from the feed stream.

In the compression step, energy is added to the isolated bed by means of heat. Assuming there is limited volume inside the adsorption bed, the bed is heated and pressurized with a negligible change in loading. Energy is continually added until a

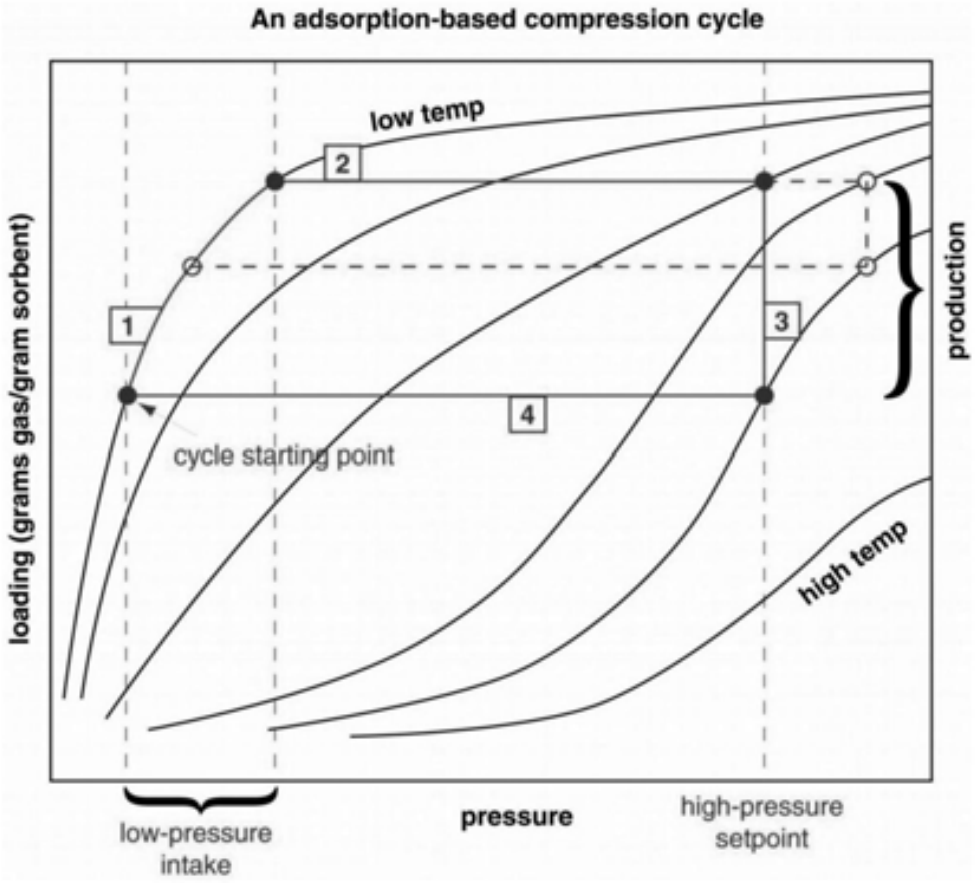

Figure 2.1: Typical work cycle of a TSA compression system.[7]

desired pressure is reached.

The sorbent bed is then opened to allow the sorbate to bleed off the sorbent at a constant pressure by the continuous addition of heat in the production step. Delivery is achieved at the expense of sorbate loading within the bed.

The sorbent bed is then closed off again and cooled, representing the regeneration step of the cycle. As the energy within the bed dissipates, the internal pressure falls and the residual sorbate is then readsorbed. When the bed reaches the original temperature, it is ready to initiate the cycle again.

2.2 Theory

We examine mass and energy transport for TSA as outlined by the generalized equations found in Bird et al.[2] with the following assumptions. The gas phase can be described by the ideal gas law. N_2 and O_2 are inert and can be modeled as a single component, i.e., air. Heat capacities of air and CO_2 are constant, which is consistent with the thermodynamic path, developed by Walton and LeVan,[10] used in writing the energy balance. The isosteric heat of adsorption is constant. Adsorption of N_2 and O_2 are negligible, and therefore adsorption of CO_2 on 5A zeolite is described by a pure component isotherm with the adsorbent properties listed in Table 2.1.

Pure-component adsorption of CO_2 onto 5A was modeled by the multi-temperature Toth isotherm Taqvi et al.[1] developed and given by

$$\overline{n} = n_s \left(1 + \frac{b}{P^m}\right)^{-1/m} \tag{2.1}$$

where P is the partial pressure of CO_2 is in Pa, n_s is the saturation capacity, and b and m are Toth parameters appearing in

$$b = b_0 \exp(-m\lambda/RT) \tag{2.2}$$

with λ representing the isosteric heat of adsorption. The Toth parameters used in our finite element models are listed in Table 2.1.

Table 2.1: Table of adsorbent physical properties and finite element parameters.

n_s	4.07 mol/kg sorbent
m	0.518
ΔH	41.8 kJ/mol
b_o	1.74×10^5
ρ_b	700 kg/m^3
χ-particle porosity	0.5
ϵ-void fraction of packing	0.4
ϵ'-total bed voidage	0.7
k	0.135 W/m K
C_{ps}	960 kJ/kg K
$C_{p,air}$	40.3 J/mol K
$C_{p,\mathrm{CO_2}}$	29.25 J/mol K
D	0.05 m^2/s
feed flow rate	0.02633 m^3/s
air mole fraction in feed	0.9974
CO_2 mole fraction in feed	0.0026
feed temperature	298 K

We write an overall material balance of the form

$$\rho_b \frac{\partial \overline{n}}{\partial t} + \epsilon' \frac{\partial c}{\partial t} + \epsilon \nabla \left(\vec{v} c\right) = 0 \tag{2.3}$$

where ρ_b is the bulk density of the adsorbent, ϵ and ϵ' are the void-fraction of packing and total bed voidage, respectively, and the fluid-phase velocity is described by Darcy's law[2] for packed beds

$$\vec{v} = -k_d \nabla P \tag{2.4}$$

We develop a component material balance for CO_2 by applying equation 2.3 for a single component which yields

$$\rho_b \frac{\partial \overline{n}}{\partial t} + \epsilon' \frac{\partial c_i}{\partial t} + \epsilon \nabla \left(\vec{v} c_i\right) = -\epsilon \nabla J_i \tag{2.5}$$

with the component molar flux described by

$$J_i = -c D_i \nabla y_i \tag{2.6}$$

We assume that the concentration of CO_2 does not measurably change after leaving the bed and therefore a Danckwert's[3] boundary condition given by

$$\frac{\partial c_i}{\partial z} = 0 \quad \text{at} \quad z = L \tag{2.7}$$

is applied to the bed outlet. Depending on whether an adsorption or desorption half cycle is being modeled, either a constant feed concentration or a no-flow boundary condition is used at the bed inlet, respectively.

The energy balance for this system is written

$$\rho_b \frac{\partial u_s}{\partial t} + \epsilon' \frac{\partial c_f u_f}{\partial t} + \epsilon \nabla \left(\vec{v} c_f u_f \right) + \epsilon \nabla q_f + \epsilon P \cdot \nabla \vec{v} = 0 \tag{2.8}$$

where the energy flux, internal energies of both the fluid and solid-phase, and the enthalpy of the fluid-phase are represented by

$$q_f = -k \nabla T \tag{2.9}$$

$$u_f \equiv h_f - P \overline{V}_f \tag{2.10}$$

$$u_s = \left(C_{ps} + C_{px} \overline{n} \right) \left(T - T_{ref} \right) - \lambda \, \overline{n} \tag{2.11}$$

$$h_f = C_{py} \left(T - T_{ref} \right) \tag{2.12}$$

where

$$C_{px} = \sum_i x_i C_{pfi} \tag{2.13}$$

and

$$C_{py} = \sum_i y_i C_{pfi} \tag{2.14}$$

The walls of the adsorbent bed are assumed to be insulated, and the bed inlet is modeled as either insulated or having a constant feed temperature depending on the half-cycle being simulated. At the bed outlet the boundary condition for the energy balance is

$$\nabla T = 0 \quad \text{at} \quad z = L \tag{2.15}$$

Table 2.2: Table of Equilibrium, Delivery, and Differential Loadings for CO_2 .

Loadings Using Only 5A Zeolite (mol/kg sorbent)			
Stage 1 Equilibrium @ 200°C, 47 mmHg	0.0637	Stage 2 Equilibrium @ 25°C, 47 mmHg	2.45
Stage 1 Feed @ 25°C, 1.9 mmHg	0.67	Stage 2 Outlet @ 200°C, 1000 mmHg	0.662
Stage 1 Differential	0.606	Stage 2 Differential	1.79
Loadings Using 5A Zeolite for Stage 1 and NaY Zeolite for Stage 2 (mol/kg sorbent)			
Stage 1 Equilibrium @ 200°C, 152 mmHg	0.172	Stage 2 Equilibrium @ 25°C, 152 mmHg	2.37
Stage 1 Feed @ 25°C, 1.9 mmHg	0.67	Stage 2 Outlet @ 200°C, 1000 mmHg	0.491
Stage 1 Differential	0.498	Stage 2 Differential	1.88

2.3 Discussion

Adsorbent modeling

The adsorption of CO_2 onto 5A zeolite was measured gravimetrically using a Cahn balance and modeled using equation 2.1. Figures 2.2 and 2.3 show measured adsorption equilibrium data along with corresponding fit isotherms for various temperatures. These demonstrate that the multi-temperature Toth isotherm describes the adsorption equilibrium well for modeling purposes. [Note the single data point in Figure 2.2 at low loading that is far removed from the fitted curve. This point is likely not accurate, with the error caused by inaccuracy in the pressure measurement or a lack of attainment of equilibrium.]

Adsorption bed sizing

Using a basis removal rate of 4 kg/day and a 60 min half cycle, the amount of CO_2 needed to be removed per cycle was calculated to be 167 g. The loadings

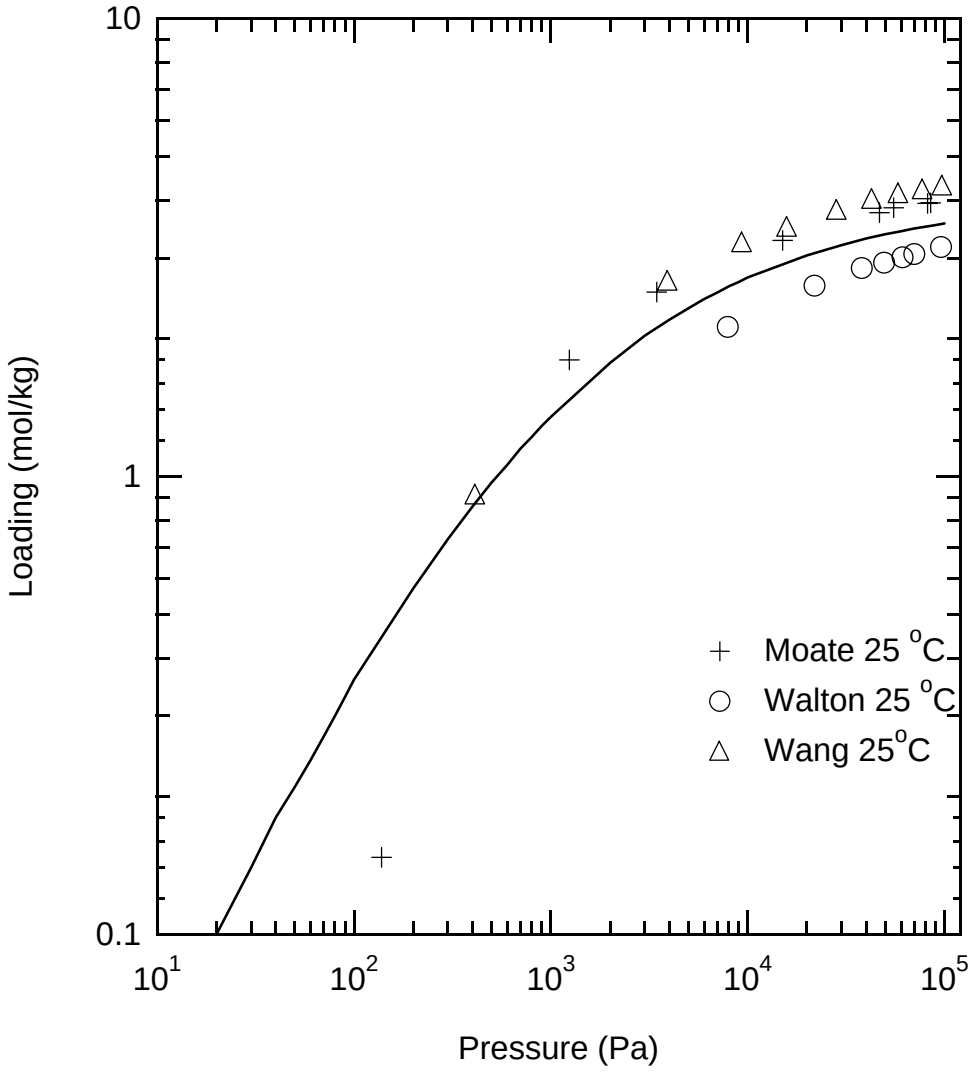

Figure 2.2: Pure-component isotherm of CO_2 on 5A at 25°C. Symbols are experimental data and the solid line is adsorption equilibria predicted by equation 2.1.

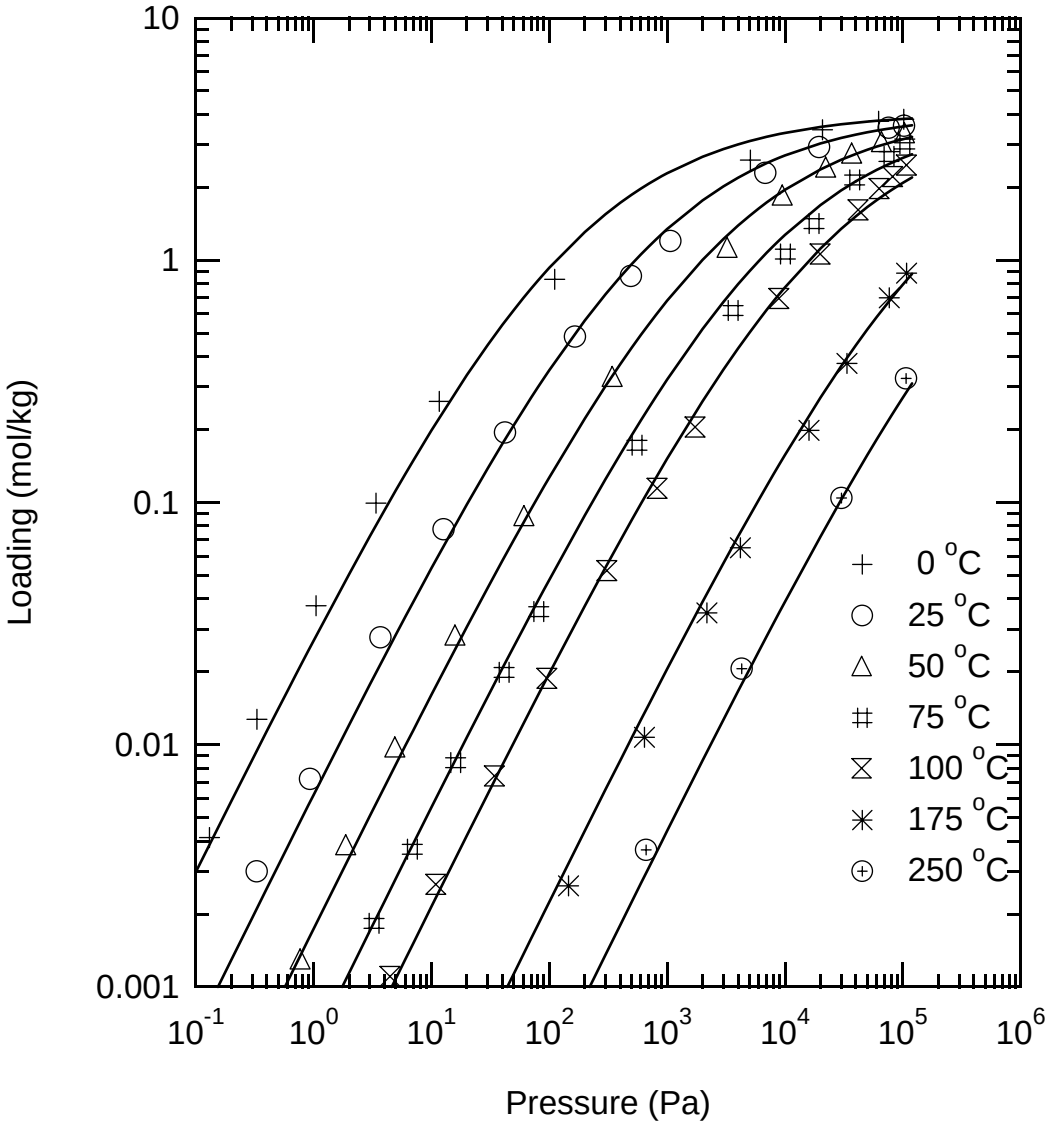

Figure 2.3: Pure-component isotherms of CO_2 on 5A. Symbols are experimental data taken from Linde and Davison, and solid lines are are adsorption equilibria predicted by equation 2.1.

in Table 2.2 were then calculated using equation 2.1 for the appropriate conditions. The loading that is calculated with this isotherm is an equilibrium loading. However, a dynamic system such as the one being used for stage 1 never reaches equilibrium. Therefore, a percent bed utilization term, η, is multiplied by the loading to account for this. Based on previous experience, the percent bed utilization of the system is very dependent on the partial pressure, ranging from 70% to 90%. For this system a conservative bed utilization of 79% was chosen based on prior experience at NASA Marshall. The estimated bed volume is then

$$V = 167\text{g } CO_2 * \frac{1\text{mol } CO_2}{44\text{g } CO_2} * \frac{1}{\left[\left(n_i \rho_b \eta + \epsilon\prime \frac{P}{RT}\right) - \left(n_f \rho_b \eta + \epsilon\prime \frac{P}{RT}\right)\right]} \tag{2.16}$$

Using the properties in Table 2.1 and the equilibrium loadings calculated from equation 2.1, volumes were calculated from equation 2.16, where n_i is the loading calculated based on a temperature of 25°C and the corresponding feed pressure, and n_f is the loading calculated for a temperature of 200°C and various equilibrium pressures. In the equation above, bed utilizations of 79% and 100% were used for stages 1 and 2 respectively. Residual loadings as well as the mass of gas in the vapor phase are also taken into account.

From equation 2.16, a comparison of the volumes of adsorbent for each stage and their sum was made for different equilibrium pressures for the cases using only 5A zeolite in both stages and using 5A zeolite in stage 1 and NaY zeolite in stage 2. As seen in Figure 2.4, a minimum is reached for the sum of the adsorbent volumes at an equilibration pressure of about 47 mm Hg when only 5A zeolite is used. In the situation when 5A and NaY are used in stages 1 and 2 respectively, a minimum for the sum of the adsorbent volumes occurs at an equilibration pressure of 152 mm Hg, as shown in Figure 2.5.

Contrary to what is seen in Table 2.2, Figure 2.5 indicates that it is not beneficial to use NaY in stage 2. Closer inspection of Table 2.2 reveals that the bulk density of NaY is much lower than that of 5A, and the low bulk density would drive

the volume of adsorbent needed to adsorb 167 g of CO_2 much higher than what would be required if only 5A were used.

Finite element modeling

To investigate breakthrough behavior of CO_2 flowing through a packed TSA bed, we solve the coupled mass and energy balances using Comsol Multi-Physics^{TM} finite element software. We begin by modeling a representative portion of the TSA bed composed of 5A zeolite that Rosen et al.[8] used in experiments which preferentially removed CO_2 from a gas mixture containing N_2, O_2, and CO_2.

The values used for the adsorbent properties and constants in the finite element simulations are shown in Table 2.1. The diffusion constant used in the model is larger than that which theory predicts for molecular diffusion but includes a contribution for dispersion; this was necessary in order for the algorithm to treat sharp transitions properly.

Initially, the bed was assumed to be saturated, simulating a bed after an adsorption half-cycle, then a series of desorption and adsorption half-cycles were simulated. During a desorption half-cycle, heaters in the bed were uniformally maintained at 200°C , and it was assumed that the adsorbent bed was well insulated on all sides except for the outlet. An adsorption half-cycle was then simulated immediately after with the only source of cooling located in the feed stream, at conditions given in Table 2.1.

The CO_2 concentration at the outlet of a bed packed with 5A zeolite is shown in Figure 2.6 for the duration of the adsorption half-cycle. There is an initial peak in the concentration of CO_2 out the outlet as the accumulated gas remaining after a desorption half-cycle is blown out in effect reducing the performance of the bed, after which breakthrough does not occur for another 1,000 seconds. Here it can be seen that any increased bed capacity from the addition of air plenums is negligible when

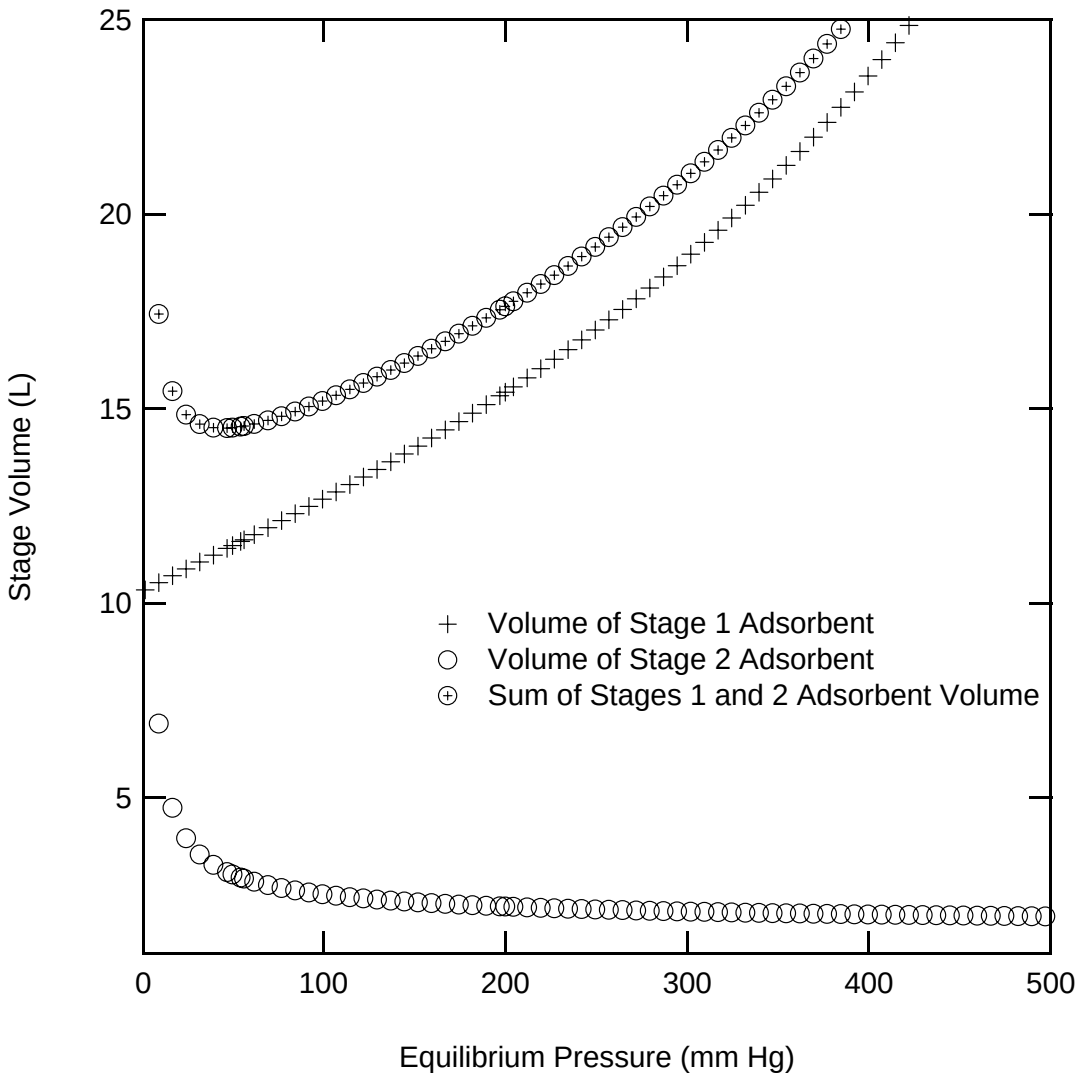

Figure 2.4: Comparison of stage volume vs equilibrium pressure using 5A in both stages and at a regeneration temperature of 473 K.

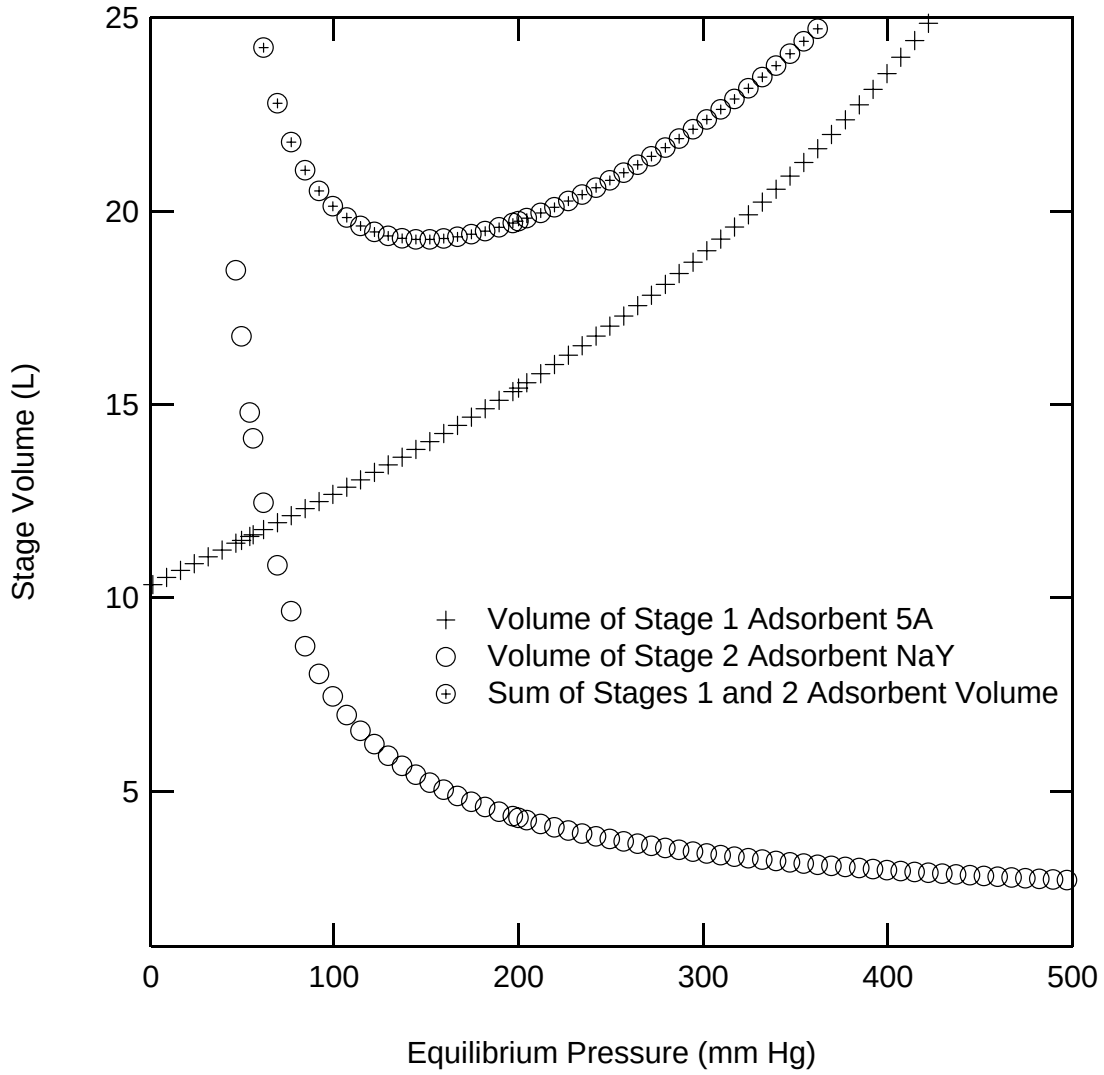

Figure 2.5: Comparison of stage volume vs equilibrium pressure using 5A in stage 1, NaY in stage 2, and at a regeneration temperature of 473 K.

compared with the increased bed capacity of a slightly larger bed, meaning that it is preferable to use the volume required by the air plenums to increase heat transfer for more adsorbent.

Figures 2.7 and 2.8 show an ideal TSA path and the path computed by our model for each stage in the adsorption cycle. From these work cycles it can be seen that the second stage resembles the ideal path more so than the first stage, indicating that stage 2 operates more efficiently. By not cooling the adsorbent bed and initiating an adsorption half-cycle immediately after a desorption half-cycle any CO_2 remaining in the fluid phase is blown out which reduces the effectiveness of the adsorbent bed.

2.4 Conclusions

General algebraic relationships were developed to determine optimum stage sizes for a coupled 2 stage TSA compressor, and modeled using material and energy balances to describe breakthrough behavior. The models were solved for both a desorption and adsorption-half cycle of CO_2 on 5A zeolite.

We determined that an optimum combined volume for the first and second stages occurs at a specific equilibration pressure between the two stages, and is dependent on the properties of the adsorbent used as well as the operating procedure of the TSA beds.

Next finite element models were developed simulating the TSA beds using material and energy balances and solved in order to model the breakthrough behavior of CO_2 for both adsorption and desorption half-cycles. Using these solutions it was determined that following a desorption half-cycle with an adsorption half-cycle without allowing the bed to cool decreases the performance of the TSA bed as the accumulated fluid phase adsorbate is blown out of the adsorption bed in the initial period of the half-cycle. We also discovered that any extra cooling afforded by the addition of air plenums did not affect the adsorption of CO_2 significantly.

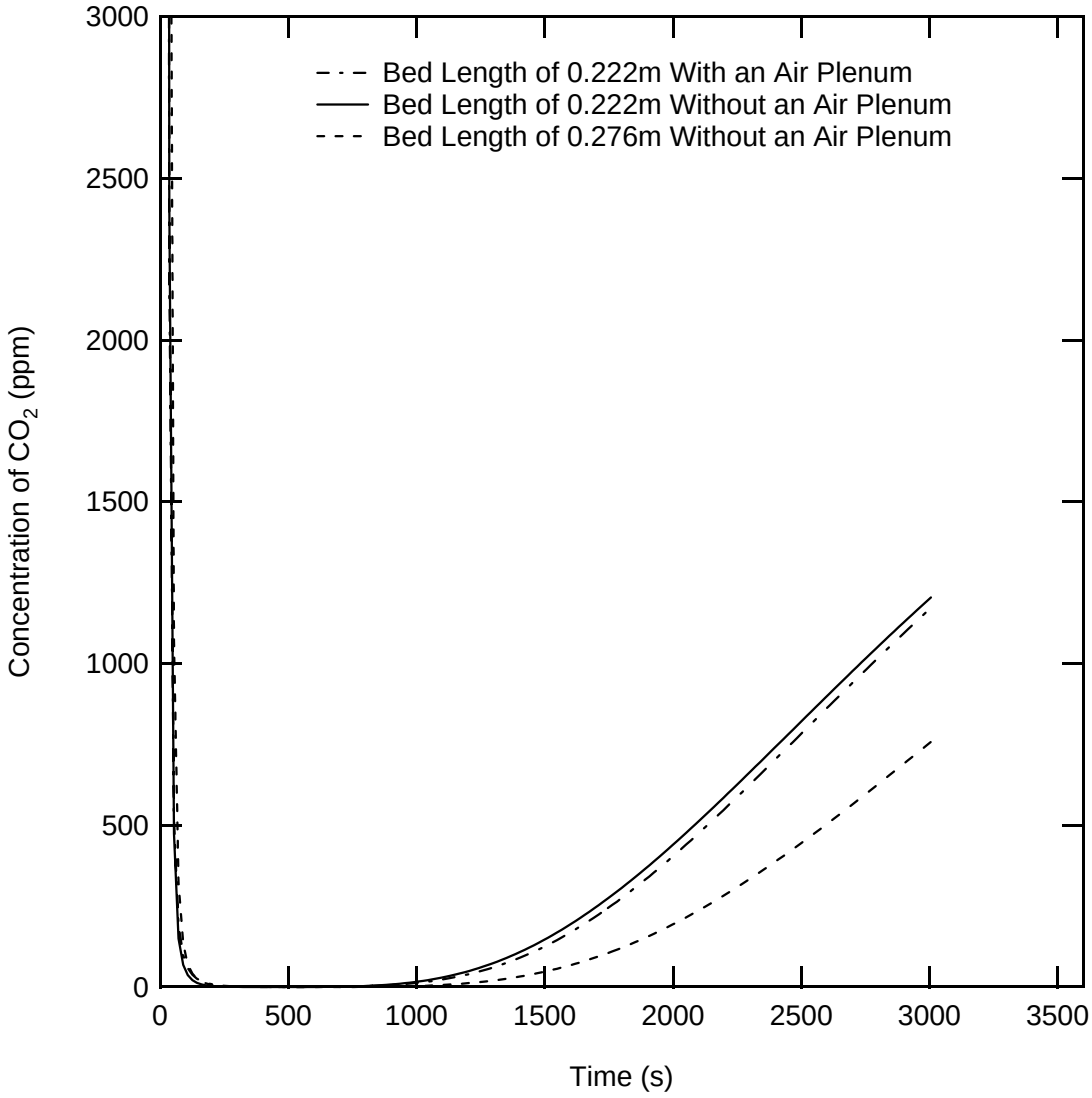

Figure 2.6: Modeled breakthrough curve for CO_2 adsorbed on 5A zeolite for various lengths of sorbent.

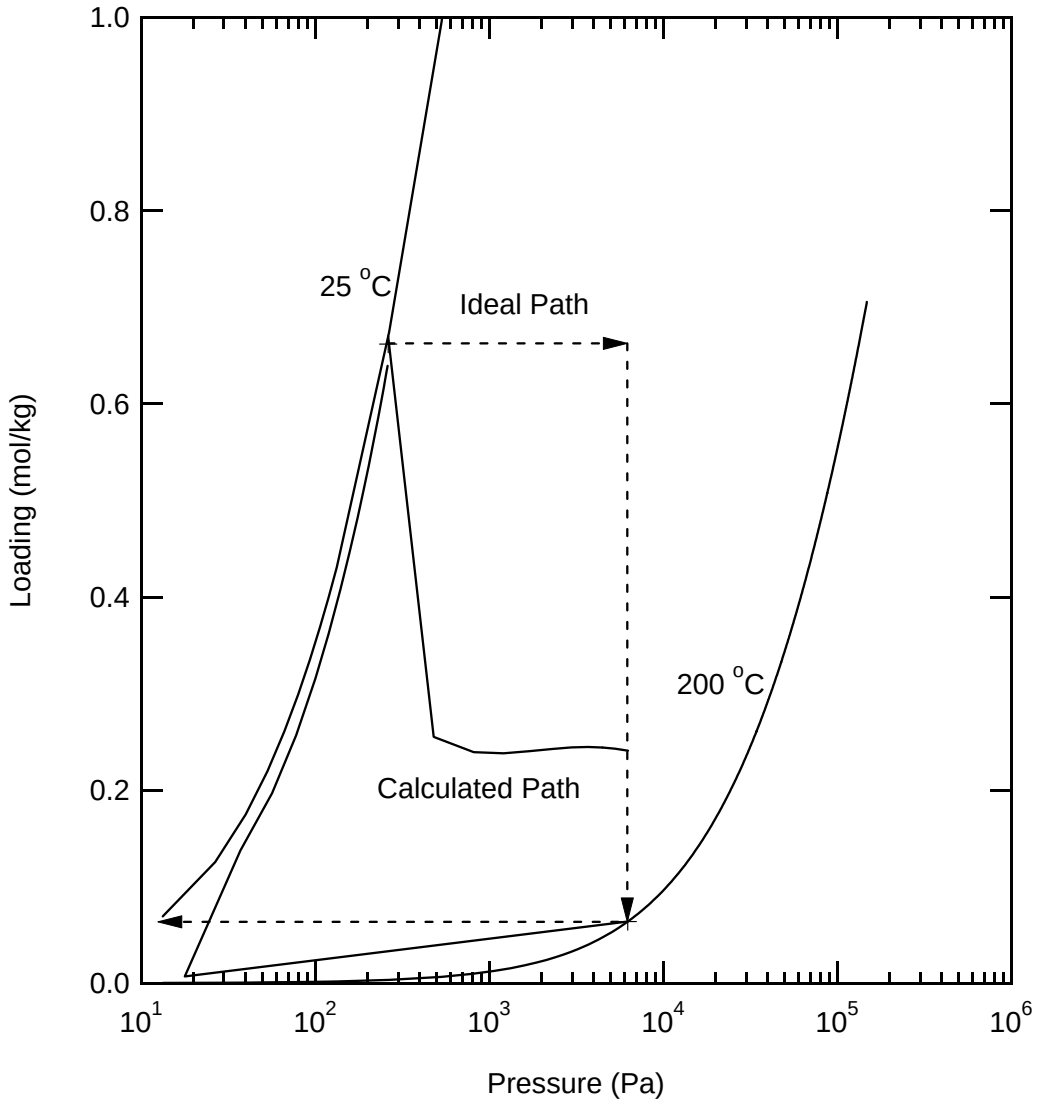

Figure 2.7: Stage 1 work capacity diagram.

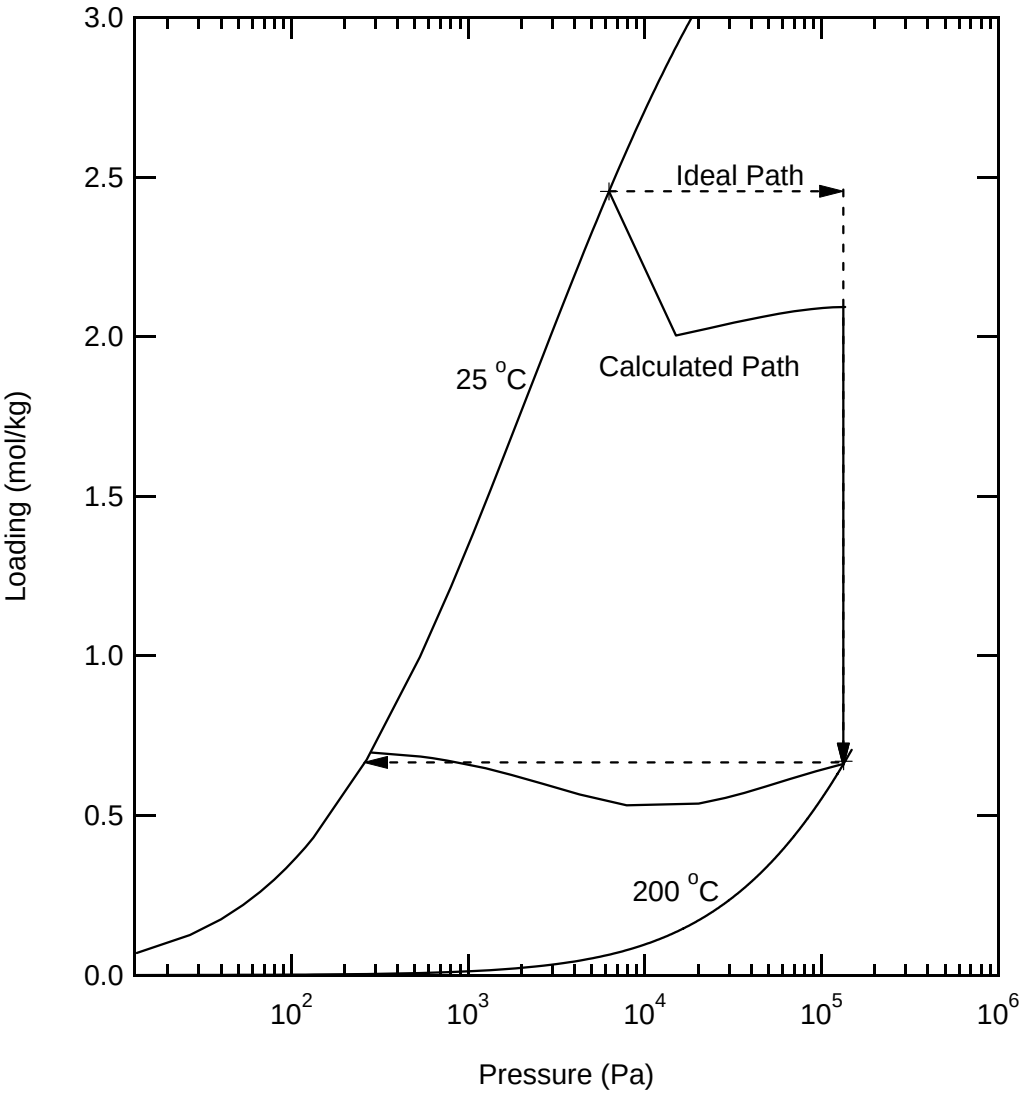

Figure 2.8: Stage 2 work capacity diagram.

Notation:

n	Loading, mol/kg sorbent
n_s	Monolayer capacity
b, b_0, m	Multi-Temperature Toth parameters
H	Isosteric heat of adsorption
R	Ideal gas constant, kPa m^3/mol K
P	Pressure, kPa
T	Temperature, K
y	Mole fraction
k_d	Darcy's law coefficient
k_f	Thermal conductivity coefficient, W/m K
C_P	Specific heat, J/kg K
C_{Ps}	Specific heat of solid, J/kg K
$\vec{v}$	Local fluid velocity, m/s
$\langle\vec{v}\rangle$	Average fluid velocity, m/s
c	Concentration, mol/m^3
K	Equilibrium Constant
D_{eff}	Effective Dispersion Constant
L	Bed Length, m

Greek Letters

ρ_b	Bulk Density
χ	Particle porosity
ϵ	Void fraction of packing
ϵ'	Total bed voidage
λ	Isosteric heat of adsorption

References

[1] Syed M. Taqvi, W. Scott Appel, M. Douglas LeVan, Coadsorption of Organic Compounds and Water Vapor on BPL Activated Carbon. 4. Methanol, Ethanol, Propanol, Butanol, and Modeling, *Ind. Eng. Chem. Res.*, 38 (1999) 240.

[2] R. B. Bird, W. E. Stewart, E. N. Lightfoot, *Transport Phenomena: Second Edition*, John Wiley and Sons, New York, 2002.

[3] P. V. Danckwerts, Continuous Flow Systems Distribution of Residence Times, *Chem. Eng. Sci.*, 2 (1953) 1

[4] R.P. Hoover, P. C. Wankat, Gas compression using temperature swing adsorption, Separation Science and Technology 37 (14) (2002) 3187-3199.

[5] A. Malek, S. Farooq, Comparison of Isotherm Models for Hydrocarbon Adsorption on Activated Carbon, *AIChE J.* 42 (1996) 3191.

[6] L.M. Mulloth, J.E. Finn, A solid-state compressor for integration of CO_2 removal and reduction assemblies, SAE International 2000-01-2352.

[7] L. Mulloth, M. Varghese, B. Luna, J. Hogan, M.D. LeVan, J.R. Moate, Development of a low-power CO_2 removal and compression system for closed-loop air revitalization in future spacecraft, SAE International, Paper 2005-01-2944 (2005) 1-8.

[8] M.S. Rosen, L.M. Mulloth, D.L. Affleck, Y. Wang, M.D. LeVan, Development and testing of a temperature-swing adsorption compressor for carbon dioxide in closed-loop air revitalization systems, SAE International, Paper 2005-01-2941 (2005) 1-6.

[9] B.K. Sward, M.D. LeVan, F. Meunier, Adsorption heat pump modeling: the thermal wave process with local equilibrium, Applied Thermal Engineering 20 (2000) 759-780.

[10] K. S. Walton, M. Douglas LeVan, Consistency of Energy and Material Balances for Bidisperse Particles in Fixed-Bed Adsorption and Related Applications, *Ind. Eng. Chem. Res.*, 42 (2003) 6938.

CHAPTER III

TEMPERATURE SWING ADSORPTION COMPRESSION: EFFECTS OF NONUNIFORM HEATING ON BED EFFICIENCY

3.1 Introduction

There is a growing need to recuperate CO_2 from fluid mixtures in many industrial applications. The separation and capture of CO_2 from flue gas due to the combustion of fossil fuels has received increased attention because of growing concerns of greenhouse gas emissions. The removal of CO_2 is also important in the sweetening of natural gas since it is a frequent contaminant. Captured and purified CO_2 can then be used in many applications such as the food and beverage industry, paper and pulp processes, and waste water treatment. Additionally, a long term goal is the sequestration of excess quantities of CO_2.

Apart from industrial applications, the capture of CO_2 from fluid streams is of interest to NASA for air revitalization in space cabins and future in situ resource utilization (ISRU) programs. Walton and LeVan[1] theoretically and experimentally investigated a novel three-step adsorption cycle for the removal and pressurization of CO_2 from a 50% mixture with CO. This process would be used in the production of oxygen from the Martian atmosphere, which consists of 95% CO_2 . In addition to the Mars ISRU program, CO_2 is captured and removed in the air revitalization system currently employed in the United States On-Orbit Segment (USOS) life support system aboard the International Space Station (ISS), which consists of a 4-bed molecular sieve system called the carbon dioxide removal assembly (CDRA).[5] Although the CDRA successfully maintains the CO_2 concentrations below the guidelines set forth by NASA, it is insufficient for use in long-duration manned space flight missions, since the system is open-loop, i.e., discharging the captured CO_2 out of the cabin into space and thereby losing a potential source of O_2. The ISS then replenishes the lost

O_2 in the space cabin by electrolyzing water.

Finn et al.,[2] Mulloth and Finn,[3] and Hoover and Wankat[4] have introduced the concept of the capture and compression of CO_2 from the environment using temperature swing adsorption compressor to feed a downstream subsystem. An example of this would be the use of a Sabatier reactor to react CO_2 present in a space cabin with hydrogen in order to produce methane and water, which would be electrolyzed into water and hydrogen. This would reduce the launch costs of missions by minimizing the amount of water needed to resupply the ISS. In order to use the Sabatier reactor, the feed pressure of CO_2 must be well above atmospheric. Mulloth et al.[5] demonstrate that by utilizing two beds in series, both the recuperation of CO_2 from the cabin and the compression required for a Sabatier reaction can be accomplished. The first bed would capture the CO_2 from the feed stream, compress it, and feed it into a second bed, which would further compress the CO_2 to the required pressure for the Sabatier subsystem.

Extensive research has been performed on temperature swing adsorption (TSA) processes for use in heat pumps. Miles and Shelton[6] designed and tested a natural gas heat pump employing a high efficiency regenerative cycle for use in residential space heating and cooling. They developed an analytical methodology for prediction of system performance and optimization. Sward et al.[7] developed a model for a TSA heat pump with a partitioned bed for use in adsorptive refrigeration cycles utilizing waste heat to assess wave shapes and study process variations. They found two unexpected results in that velocity reversals occur due to loading increases during desorption and decreases during adsorption, and sections of the bed were not pressurized sequentially with the order instead being dependent on the location of the thermal wave.

Some research has been done on TSA for use in sequestration of an adsorbate from a fluid mixture using various methods for temperature control of the adsorbent bed. Merel et al.[8] performed TSA experiments of CO_2 adsorbed on 13X in order

to determine the performance capabilities of an indirect cooling and heating method. They concluded that the optimal conditions for adsorption were a 50 minute half-cycle and that desorption should be halted after the preheating step with no use of a purge gas. In their work they recognized that the specific heat consumption was slightly higher than that put forth by Bounaceur et al.[9] However, their process configuration (i.e., their choice of adsorbent, number of beds, step duration, etc.) was not optimized. Since there are numerous approaches of supplying energy to the TSA bed during desorption, it is necessary to determine how temperature variations in the bed impact future adsorption cycles.

The scope of this paper is to determine the impact that nonuniform heating has on the performance of the desorption half-cycle in temperature swing compression. We model consecutive desorption and adsorption half cycles of CO_2 for a bed consisting of 5A zeolite for varying degrees of nonuniform heating using material and energy balances developed by Sward et al.[7] and Walton and LeVan.[10] During the desorption half-cycles modeled, the total energy supplied by heaters to the bed remains constant, but the fraction of the total energy that each heater individually supplies is altered in order to study the mass of desorption from the bed per unit energy supplied, i.e., the regeneration efficiency, η. We believe this is the first study performed which considers the impact of nonuniform heating on desorption for a TSA bed.

3.2 Mathematical Model

Sward et al.[7] developed a mathematical model for mass and energy transport to describe the basic principles of the TSA cycle that we use in our simulations by applying the following assumptions to the generalized mass and energy transport equations outlined in Bird et al.[11] The gas phase can be described by the ideal gas law. N_2 and O_2 are inert and can be modeled as a single component, i.e., air. Heat

Table 3.1: Table of adsorbent physical properties and finite element parameters.

n_s	4.07 mol/kg sorbent
m	0.518
ΔH	41.8 kJ/mol
b_o	1.74×10^5
ρ_b	700 kg/m^3
χ-particle porosity	0.5
ϵ-void fraction of packing	0.4
ϵ'-total bed voidage	0.7
k	0.135 W/m K
C_{ps}	960 kJ/kg K
$C_{p,air}$	40.3 J/mol K
$C_{p,\mathrm{CO_2}}$	29.25 J/mol K
D	0.05 m^2/s
feed flow rate	0.02633 m^3/s
air mole fraction in feed	0.9974
CO_2 mole fraction in feed	0.0026
feed temperature	298 K

capacities of air and CO_2 are constant, which is consistent with the thermodynamic path, developed by Walton and LeVan,[10] used in writing the energy balance. The isosteric heat of adsorption is constant. Adsorption of N_2 and O_2 are negligible, and therefore adsorption of CO_2 on 5A zeolite is described by a pure component isotherm with the adsorbent properties listed in Table 3.1.

The isotherm chosen to model CO_2 adsorption is the multi-temperature Toth isotherm given by Taqvi and LeVan[12]

$$\overline{n} = n_s \left(1 + \frac{b}{P^m}\right)^{-1/m} \tag{3.1}$$

where the partial pressure of CO_2 is in Pa, n_s is the saturation capacity, and b and m are Toth parameters appearing in

$$b = b_0 \exp(-m\lambda/RT) \tag{3.2}$$

with λ representing the isosteric heat of adsorption. The Toth parameters used in the finite element modeling are listed in Table 3.1.

Applying the above assumptions, the overall material balance is then written

$$\rho_b \frac{\partial \overline{n}}{\partial t} + \epsilon' \frac{\partial c}{\partial t} + \epsilon \nabla \left(\vec{v} c \right) = 0 \tag{3.3}$$

where the fluid-phase velocity is described by Darcy's law for packed beds

$$\vec{v} = -k_d \nabla P \tag{3.4}$$

and the component material balance for CO_2 is written

$$\rho_b \frac{\partial \overline{n}}{\partial t} + \epsilon' \frac{\partial c_i}{\partial t} + \epsilon \nabla \left(\vec{v} c_i \right) = -\epsilon \nabla J_i \tag{3.5}$$

with the component molar flux described by

$$J_i = -c D_i \nabla y_i \tag{3.6}$$

A Danckwert's boundary condition

$$\frac{\partial c_i}{\partial z} = 0 \quad \text{at} \quad z = L \tag{3.7}$$

is applied to the bed outlet and depending on which half cycle is being modeled either a constant feed concentration or a no-flow boundary condition is used at the bed inlet.

The energy balance for this system is written

$$\rho_b \frac{\partial u_s}{\partial t} + \epsilon' \frac{\partial c_f u_f}{\partial t} + \epsilon \nabla \left(\vec{v} c_f u_f \right) + \epsilon \nabla q_f + \epsilon P \cdot \nabla \vec{v} = 0 \tag{3.8}$$

where the energy flux, internal energies of both the fluid and solid-phase, and the enthalpy of the fluid-phase are represented by

$$q_f = -k \nabla T \tag{3.9}$$

$$u_f \equiv h_f - P \overline{V}_f \tag{3.10}$$

$$u_s = \left(C_{ps} + C_{px} \overline{n} \right) \left(T - T_{ref} \right) - \lambda \, \overline{n} \tag{3.11}$$

$$h_f = C_{py} \left(T - T_{ref} \right) \tag{3.12}$$

where

$$C_{px} = \sum_i x_i C_{pfi} \tag{3.13}$$

and

$$C_{py} = \sum_i y_i C_{pfi} \tag{3.14}$$

The walls of the adsorbent bed are assumed to be insulated, and the bed inlet is modeled as either insulated or having a constant feed temperature depending on the half-cycle being simulated. At the bed outlet the boundary condition for the energy balance is

$$\nabla T = 0 \quad \text{at} \quad z = L \tag{3.15}$$

3.3 Results and Discussion

To determine the effects of nonuniform heating on the temperature swing process, we solve the coupled equations 3.3, 3.5, and 3.8 using Comsol Multi-Physics^{TM} finite element software. We begin by modeling a representative portion of the TSA bed composed of 5A zeolite that Rosen et al.[13] used in their experiments, in which CO_2 is preferentially removed from a gas mixture containing N_2, O_2, and CO_2.We consider the system shown in Figure 3.1, which is a simplified version of the more complex adsorption compressor considered by Rosen et al. Their paper contains photographs of a working temperature swing adsorption compressor as well as our calculations for the performance of the device. The calculations presented here consider the fundamental and important issue of nonuniform heating for a simplified model system using a refined version of our earlier mathematical model.

The values used for the adsorbent properties and constants in the finite element simulations are shown in Table 3.1. The diffusion constant used in the model is larger than that which theory predicts for molecular diffusion and includes a contribution for dispersion; this was necessary in order for the algorithm to treat sharp transitions properly.

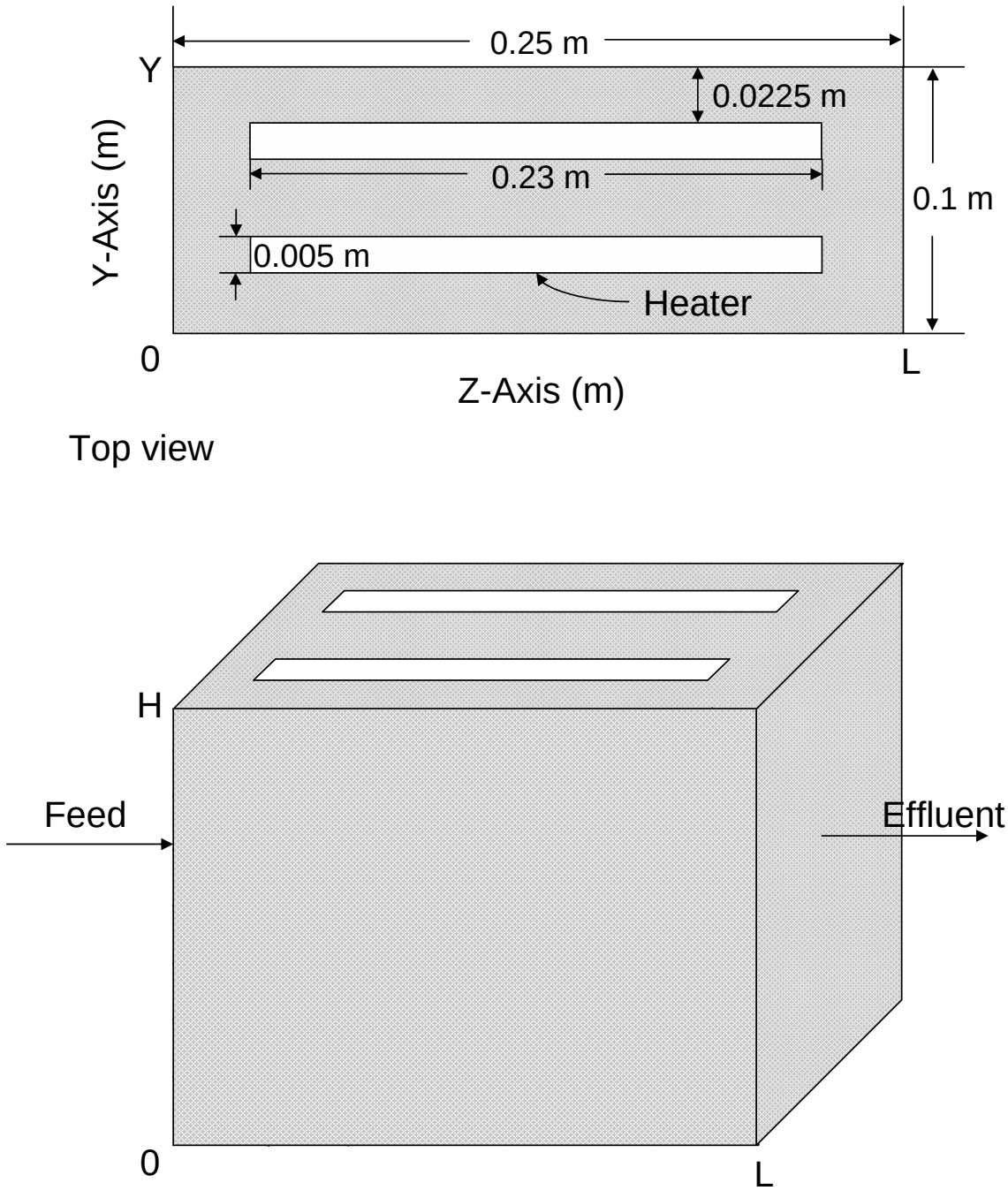

Figure 3.1: Geometry of the adsorption bed used in finite element modeling.

Initially, the bed was assumed to be saturated, simulating an adsorbent bed after an adsorption half-cycle. Sets of hour long desorption half-cycles were then modeled in which a total amount of energy of 4600 kW·h supplied to the system remained constant but was allocated to the heaters differently via a constant flux at the surface of the heaters. During this step, the bed was modeled as being insulated on all sides except for the bed outlet, which was modeled as having a constant pressure. As the desorption process occurs, convection arising due to a pressure gradient caused by CO_2 being released into the gas phase sweeps the fluid out of the bed. The fraction of the total energy supplied by the heaters varies in each simulation, ranging from both heaters supplying half of the total energy of the system to only one of the heaters supplying all of the energy.

Example loading profiles produced by the finite element software are shown in Figures 3.2 through 3.5. Figures 3.2 and 3.3 depict the mass of CO_2 adsorbed at 30 minutes and one hour, respectively, during the uniform heating desorption half-cycle. Figures 3.4 and 3.5 depict the mass of CO_2 at 30 minutes and an hour respectively when only one heater is used during the desorption half-cycle.

Next, one-hour long adsorption half-cycles were modeled with no blowdown of the bed. The feed conditions used are given in Table 3.1. During adsorption the bed is cooled only by the temperature of the feed stream, and essentially all remaining CO_2 in the fluid phase is swept out of the bed in the first minute of the simulation. Desorption and adsorption half-cycles are repeatedly simulated until the system reaches a periodic state at which point the ratio of the mass of CO_2 that is desorbed to the amount of total energy supplied is determined. The simulations were then repeated for two other values of the bed's thermal conductivity to determine the importance of the numerical value of this parameter on performance.

In the second set of simulations, the bed's geometry was altered in a way so as to retain the same total volume, but double the effective thermal conductivity, i.e.,

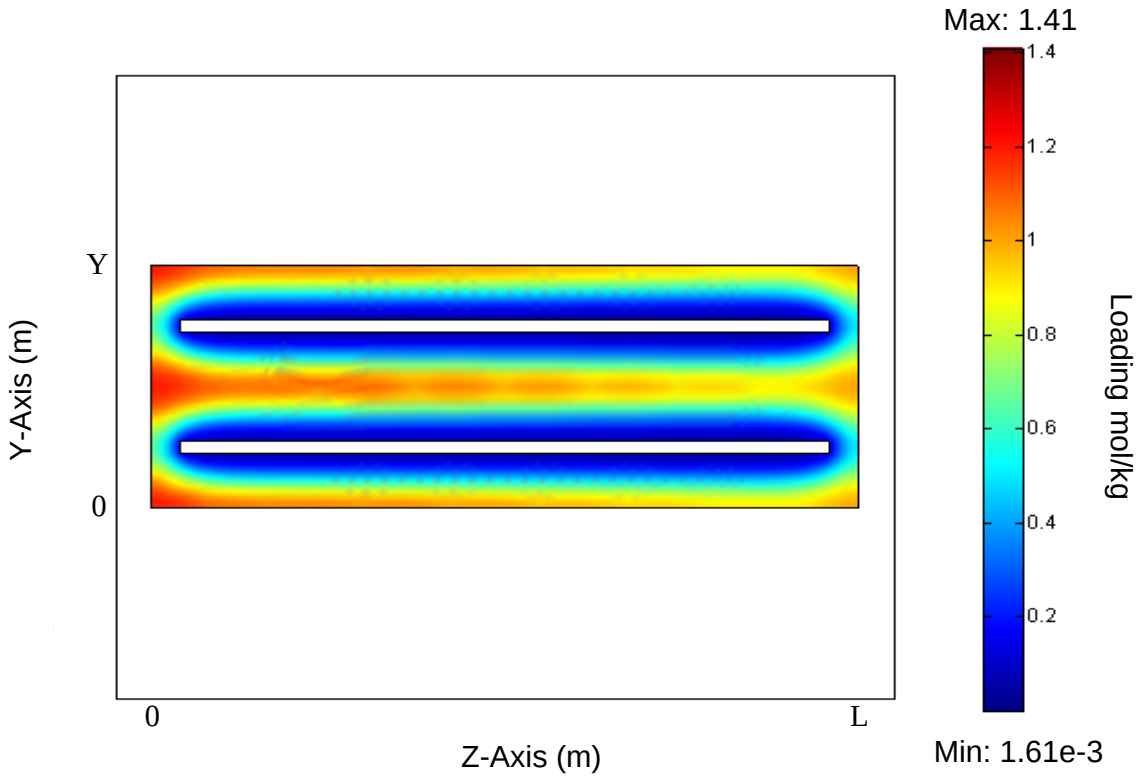

Figure 3.2: Loading profile for the uniform heating model considered 30 minutes into the desorption half-cycle.

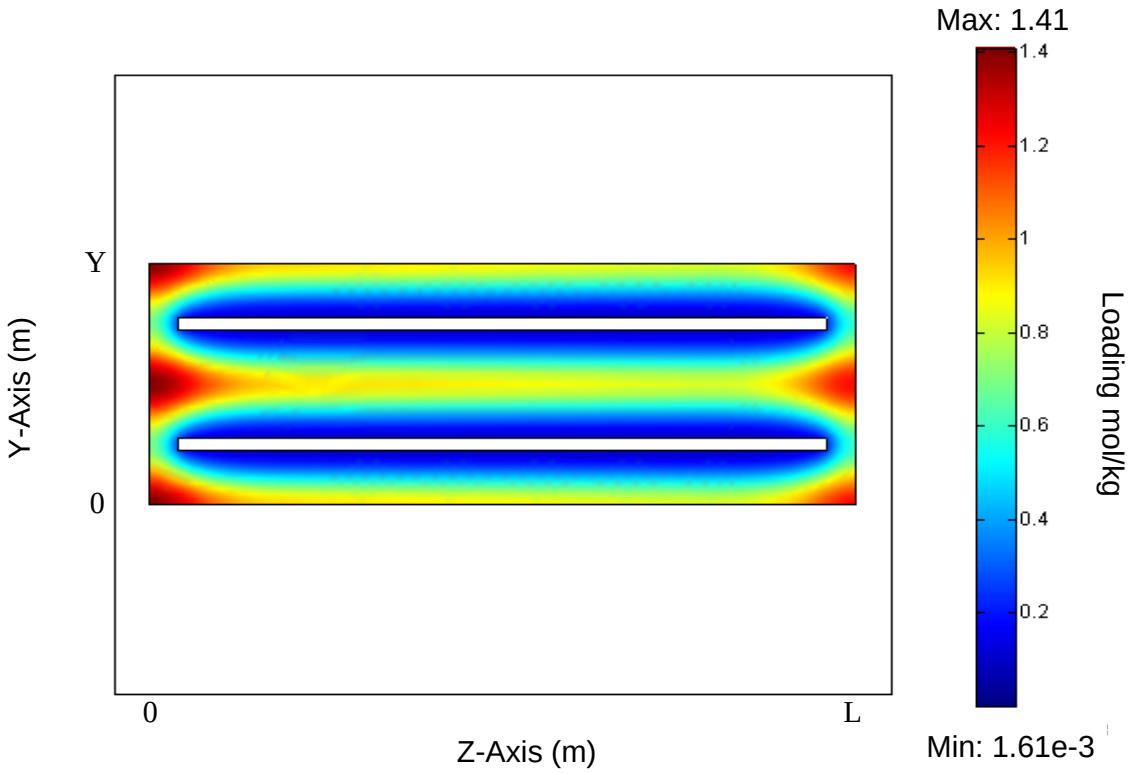

Figure 3.3: Loading profile for the uniform heating model considered at the end of the desorption half-cycle.

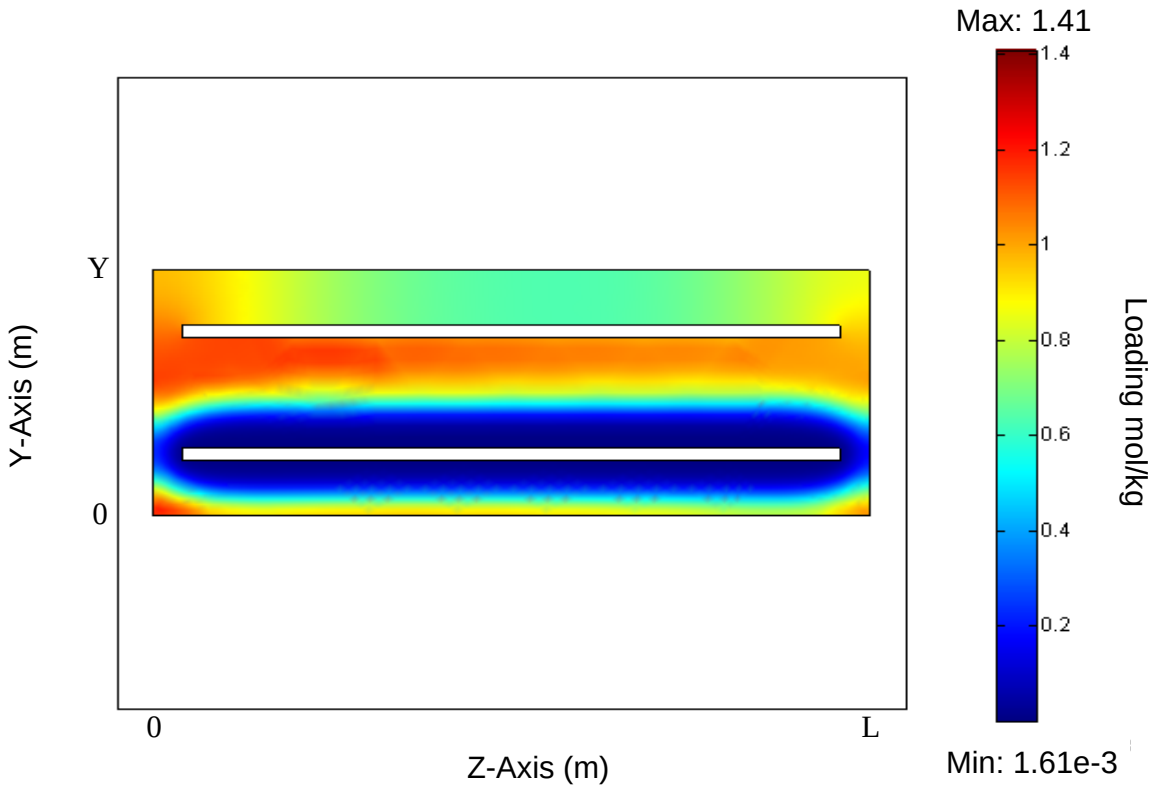

Figure 3.4: Loading profile for the nonuniform single heater model 30 minutes into the desorption half-cycle.

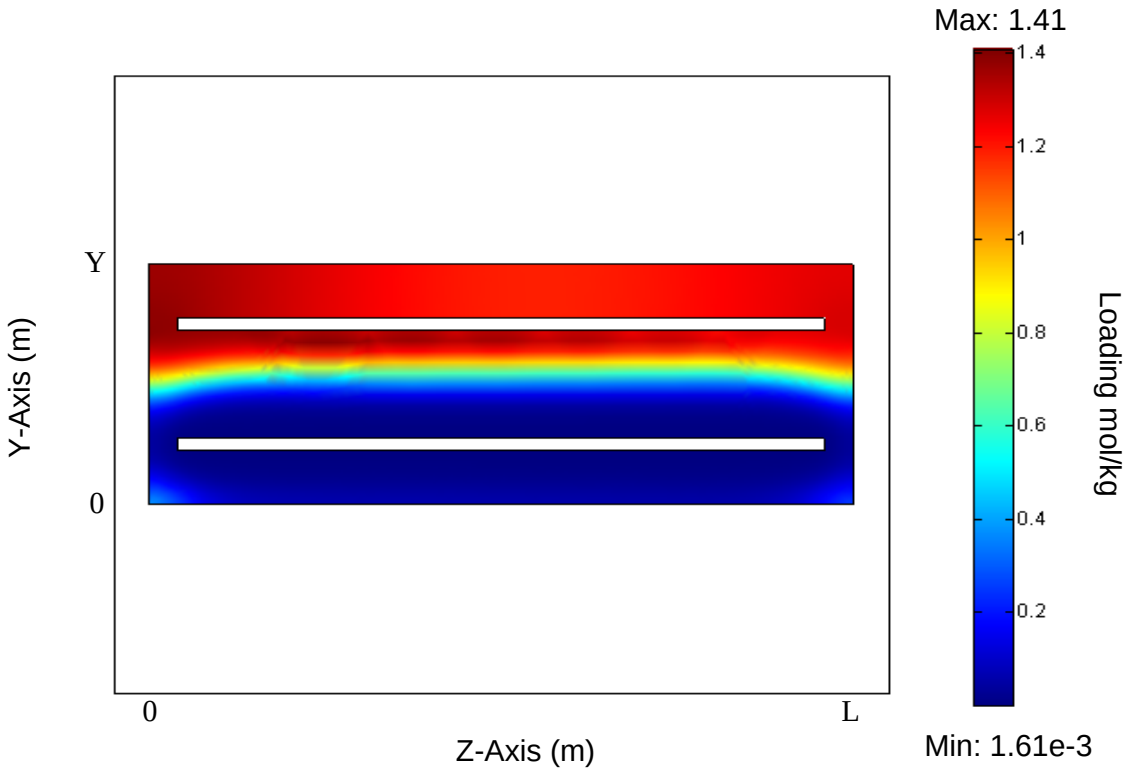

Figure 3.5: Loading profile for the nonuniform single heater model at the end of the desorption half-cycle.

the bed height was halved and the bed and heater lengths were doubled. Also, the energy flux at the heater boundaries was reduced in order to supply the same total energy as in the first set of simulations, since the surface areas of the heaters were doubled as well.

In the third set of simulations, the bed's geometry was kept constant but the value of the thermal conductivity of the adsorbent was doubled in order to compare with those of the second set. The energy flux for these simulations were kept the same as the first set maintaining a constant energy flux at the heater boundaries.

In the fourth and final set of simulations, the adsorbent's thermal conductivity was increased to a large value (100 W/(m K)) in order for the finite element solver to approximate the case of an infinite thermal conductivity, i.e., a system with 100% heating efficiency. These simulations were done in order to have an upper limit established for the regeneration efficiency. Further increases in the thermal conductivity have no observable effect.

A regeneration efficiency, η, was then determined for each set of simulations after they reached a periodic state by taking the ratio of the mass of CO_2 desorbed to the total energy supplied. These are compared in Figure 3.6. It is apparent that as the thermal aspect of the adsorbent bed becomes increasingly nonuniform during desorption, the regeneration efficiency decreases with the minimum occurring when only one heater supplies energy to the adsorbent bed. Also, the bed geometry has a significant impact on the regeneration efficiency and must be taken into account to approach an ideal value.

Figures 3.7 and 3.8 depict the amount of CO_2 in the adsorbed-phase per unit depth in the TSA bed at the periodic state after an adsorption and desorption half-cycle respectively for that of a realistic thermal conductivity compared with an essentially infinite thermal conductivity, a thermal conductivity that has been doubled, and when the bed height is halved and length doubled. The units on the y-axis

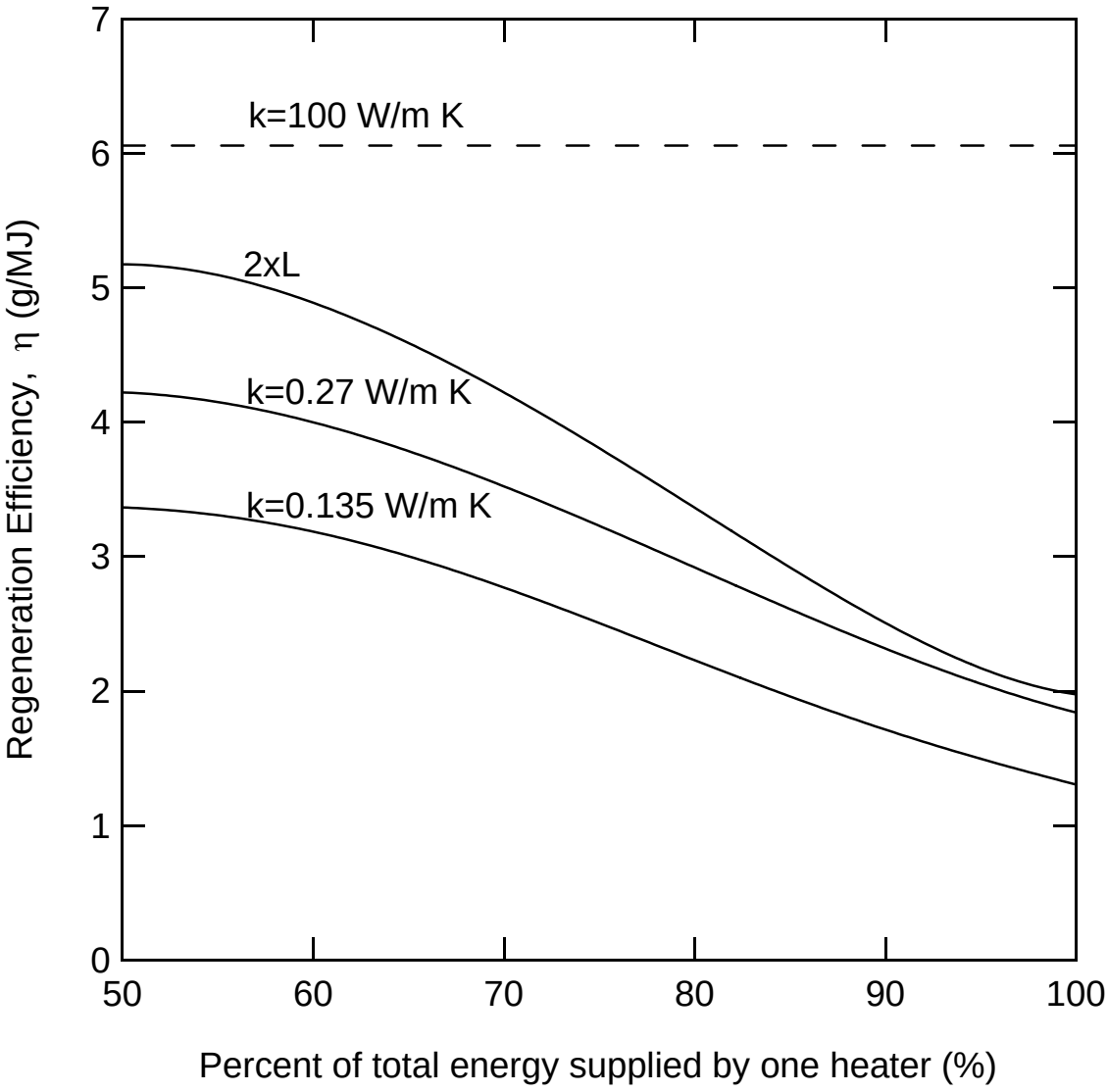

Figure 3.6: Mass of CO_2 desorbed per unit energy supplied as a function of the percent of the total energy supplied to one heater for a realistic, large, and doubled value of thermal conductivity. The curve labeled $2 \times L$ used $k = 0.135$ W/m K and has half the height and twice the length of the other geometry (i.e., Y has been halved and L has been doubled) with the heaters modified proportionately.

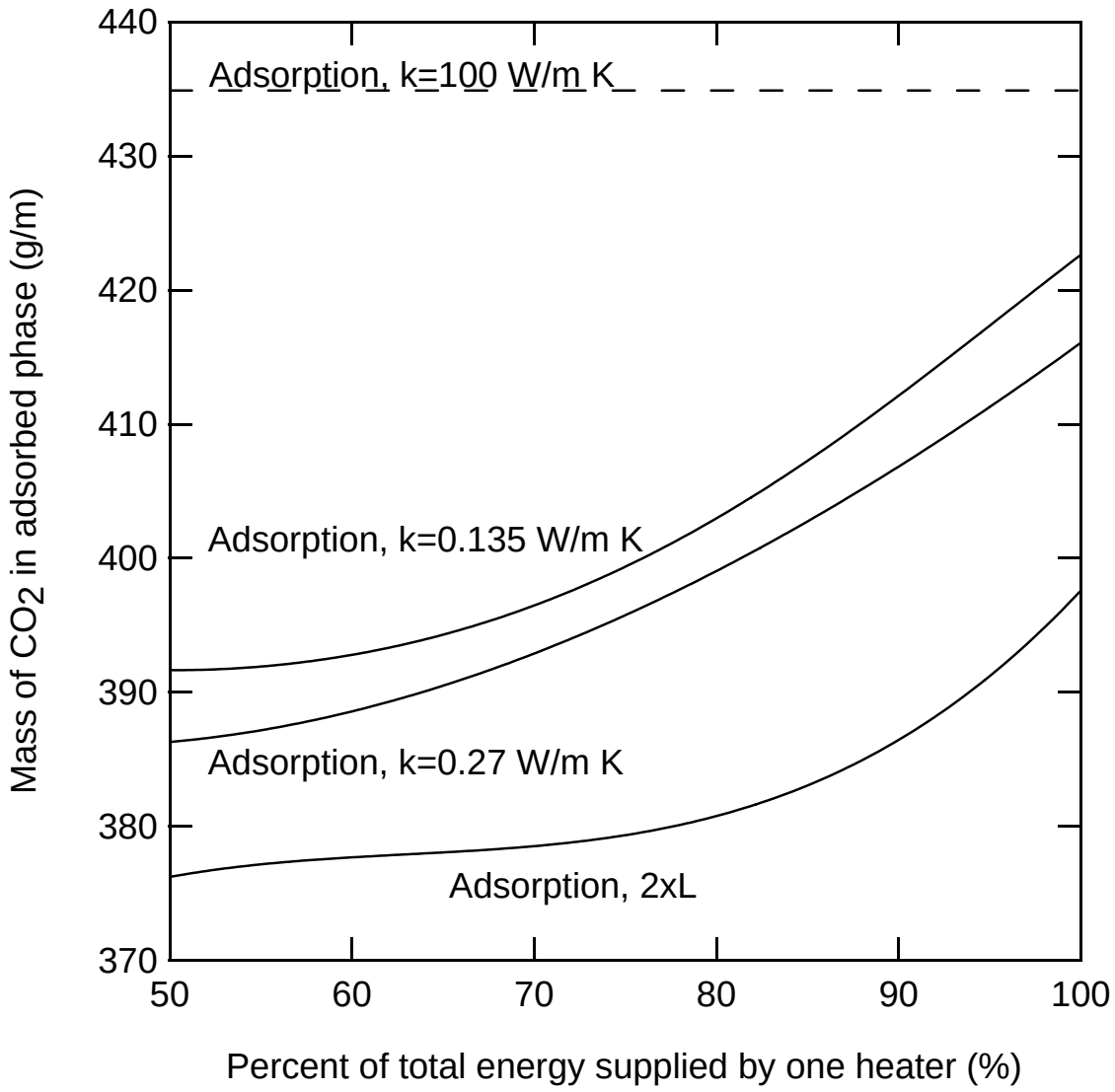

Figure 3.7: Mass of CO_2 in the adsorbed phase per unit depth of the adsorbent bed after an adsorption half-cycle for a realistic, large, and doubled value of thermal conductivity. The curve labeled $2 \times L$ used $k = 0.135$ W/m K and has half the height and twice the length of the other geometry (i.e., Y has been halved and L has been doubled) with the heaters modified proportionately..

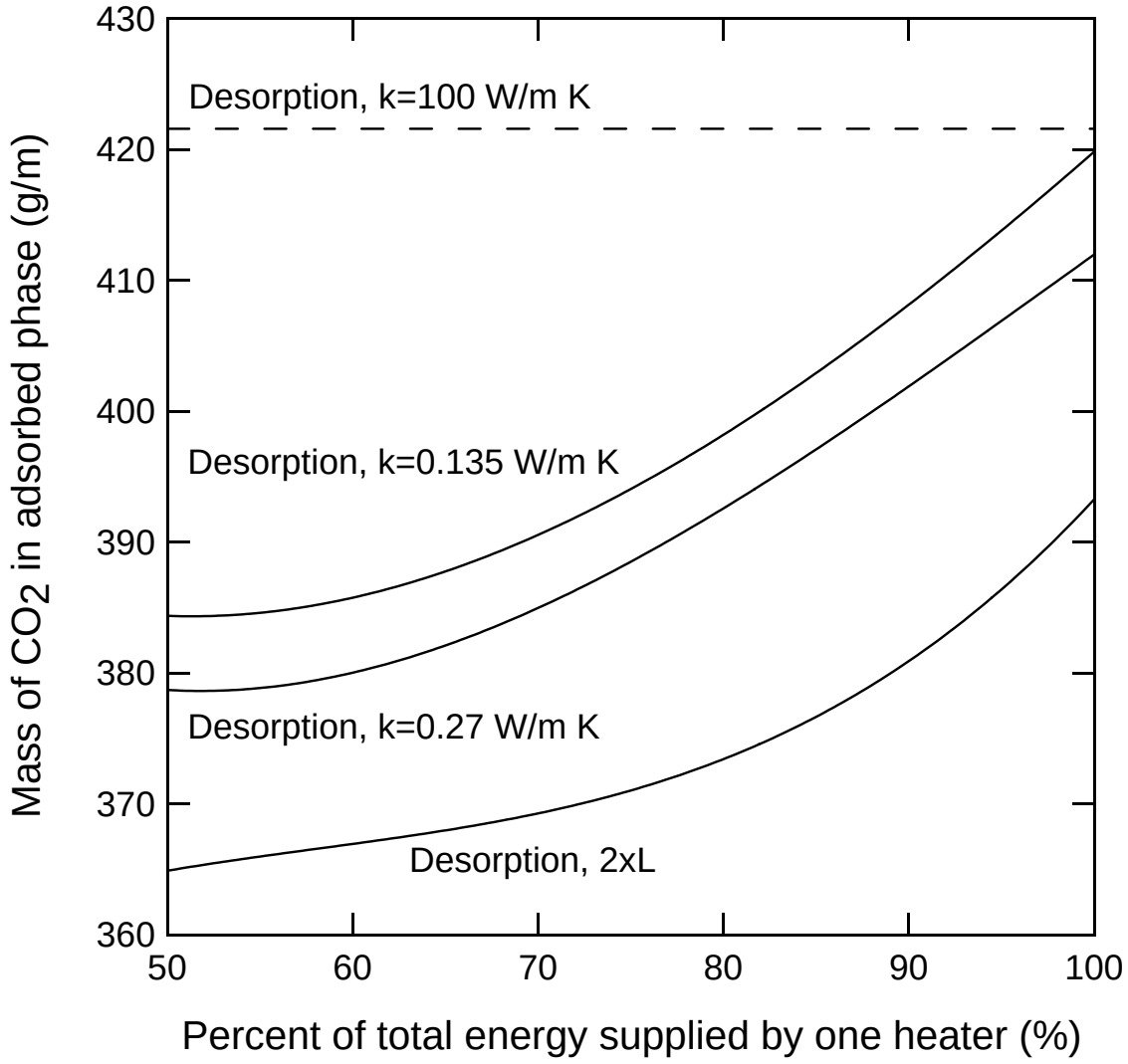

Figure 3.8: Mass of CO_2 in the adsorbed phase per unit depth of the adsorbent bed after a desorption half-cycle for a realistic, large, and doubled value of thermal conductivity. The curve labeled $2 \times L$ used $k = 0.135$ W/m K and has half the height and twice the length of the other geometry (i.e., Y has been halved and L has been doubled) with the heaters modified proportionately..

include a unit of length since the simulations performed were in 2-D and are independent of the x-axis. Therefore, the total mass would be determined by multiplying the g/m by the depth of the TSA bed, H. Alternatively, the cross sectional area of the packed bed is 0.0227 m^2 based on the dimensions shown in Figure 3.1, which when multiplied by the bulk density of packing, 700 kg/m^3 from Table 3.1, gives 15.9 kg of adsorbent per meter of bed depth. Thus, ordinate values from Figures 3.7 and 3.8 can be divided by this to give the weight fraction loading of the adsorbent.

At first glance it would appear that as the amount of energy supplied by the bottom heater reaches 100%, the mass of CO_2 removed from the feed stream is much greater than when both heaters each supply half of the total energy. However, when the difference between the mass of CO_2 adsorbed after the adsorption and desorption half-cycles is considered, as shown in Figure 3.9, it is clear that a smaller fraction of CO_2 is being removed from the process stream.

Also, the set of simulations in which the bed length is doubled retains less CO_2 in the bed after the desorption half-cycle than the previous set of simulations where the thermal conductivity is a realistic value and the case where the thermal conductivity is doubled. The mass of CO_2 adsorbed is the highest for the simulations in which the thermal conductivity approaches infinity since the bed is maintained at 298K and the heat of adsorption has no effect on adsorption equilibrium.

Examining Figures 3.6, 3.7, and 3.8 it should be apparent that in order to increase the CO_2 removal efficiency in TSA systems, rigorous heater control must be established to have the bed approach balanced conditions during heating, and the geometry of the adsorbent bed must be designed to optimize the effective thermal conductivity. Having too large a temperature gradient during the desorption half-cycle or having the heaters spaced farther apart than the optimum can greatly reduce the desorption of CO_2 from the adsorbed phase, which in turn also reduces the amount of CO_2 removed from the feed stream during adsorption.

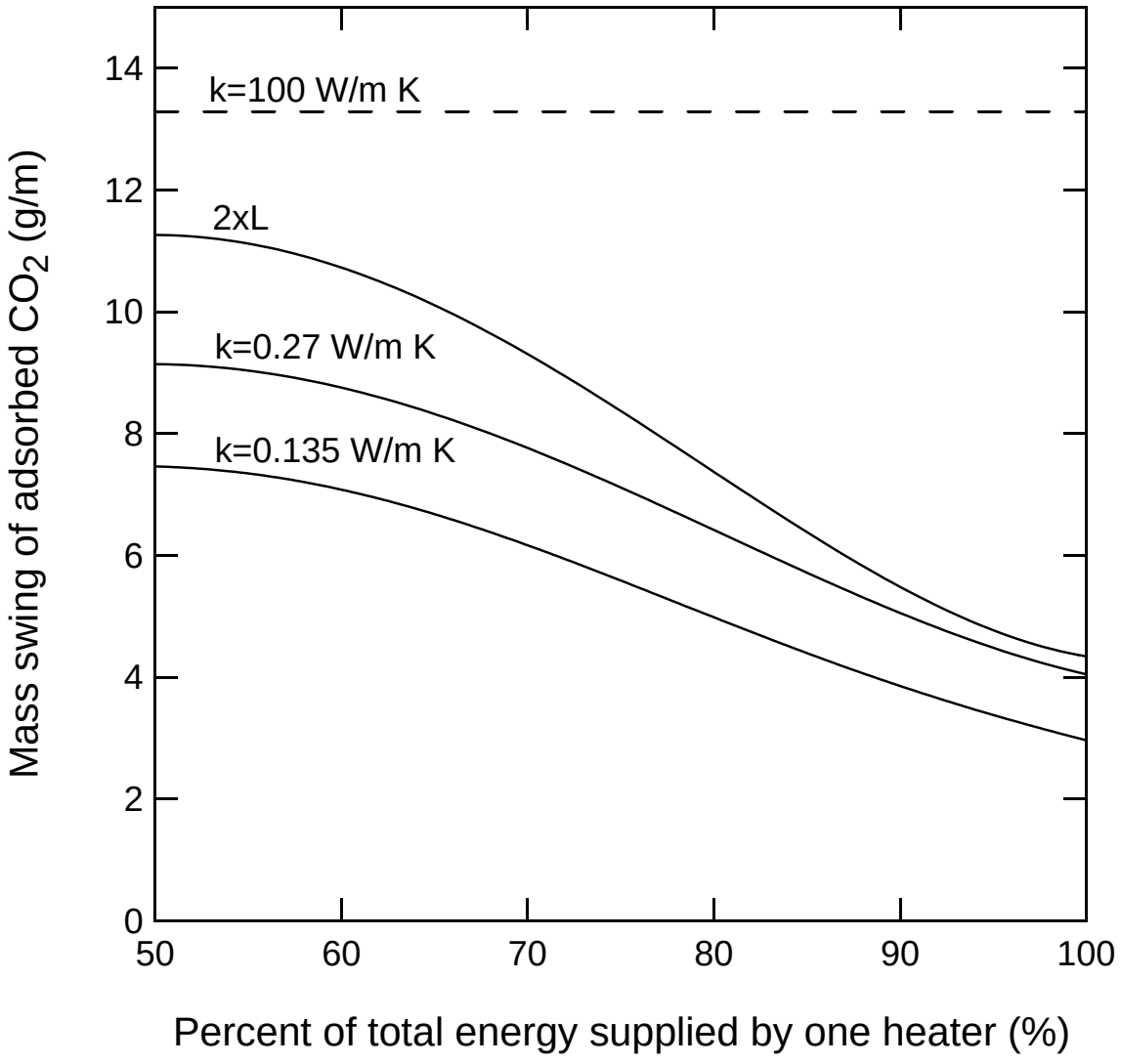

Figure 3.9: Difference in the mass of CO_2 in the adsorbed phase per unit depth of the adsorbent bed between adsorption and desorption half-cycles for a realistic, large, and doubled value of thermal conductivity. The curve labeled $2 \times L$ used $k = 0.135$ W/m K and has half the height and twice the length of the other geometry (i.e., Y has been halved and L has been doubled) with the heaters modified proportionately..

It should also be noted that the simulations performed were not optimized for the maximum removal of CO_2. In the simulations only one bed with two heaters was examined, however to increase the amount of CO_2 removed from the feed stream Mulloth et al.[5] show that a minimum of two TSA beds in series would be needed. In our simulations, the CO_2 desorbed was swept out of the bed within the first minute of the adsorption half-cycle. However, with a second bed the mass of CO_2 would ideally be captured and pressurized in the second TSA bed, thereby minimizing the amount of CO_2 that reenters the feed stream.

3.4 Conclusions

Mathematical models were formulated using material and energy balances previously developed by Sward et al.[7] and Walton and LeVan[10] and solved numerically in order to examine the influence that temperature gradients within the bed have on TSA compression efficiency. The models were solved for both a desorption and adsorption-half cycle of CO_2 on 5A zeolite. Several cases were examined in which the allocation of the energy supplied to the adsorbent bed was varied between two heaters ranging from an essentially uniform heating case to only one heater supplying the energy. Alternating adsorption and desorption half-cycles were simulated until a periodic state was reached at which point a comparison of the regeneration efficiencies was made for all of the simulations.

We determined that for the scale of the system and the materials considered, the value of the effective thermal conductivity of the bed has a significant impact on performance. By altering the geometry of the adsorbent bed, the effective thermal conductivity was doubled and the regeneration efficiency was increased by nearly 55%. Also, the case in which both of the heaters supply equal amounts of energy to the adsorbent bed has the highest regeneration efficiency, as would be expected.

With imbalanced heating loads, as would occur with a system malfunction,

the performance deteriorates significantly if the bed has expected values of thermal conductivity. This means that in order to maintain a high level of efficiency in a temperature swing adsorption compression process, it is necessary to have proper control of the energy supplied to a bed, ensuring that it is distributed evenly throughout. Alternatively, efforts could be made to increase the thermal conductivity of the bed or redesign its geometry to protect against such a degradation in performance. These are important factors in the operation of TSA processes that will help to insure that the bed removes the mass of CO_2 specified in the design.

Notation:

b, b_0, m	multi-temperature Toth parameters
c	fluid-phase concentration, mol/m^3
C_p	heat capacity, J/(kg K)
D	diffusion coefficient, m^2/s
h	enthalpy, J/mol
H	depth of TSA bed, m
J	molar flux, mol/(m s)
k	thermal conductivity, W/(m K)
k_d	Darcy's law coefficient, m^2/(Pa s)
L	length of TSA bed, m
$\overline{n}$	loading, mol/kg
n_{avg}	domain averaged loading, mol/kg
n_s	saturation capacity, mol/kg
n_{sat}	saturated bed loading, mol/kg
P	pressure, Pa
q	thermal flux, J/(m-s)
t	time, s
u	internal energy, J/mol: fluid phase. J/kg: stationary phase
$\overline{V}$	molar volume, m^3/mol
$\vec{v}$	velocity, m/s
x_i	fluid-phase mole fraction based on adsorbed-phase composition
y_i	fluid-phase mole fraction based on fluid-phase composition
Y	width of TSA bed, m
z	axial coordinate, m

Greek Letters

ϵ	void fraction of packing
$\epsilon^{'}$	total bed voidage, $\epsilon + (1 - \chi)\,\epsilon$
λ	isosteric heat of adsorption, J/mol
ρ_b	bulk density of packing kg/m^3
χ	particle porosity (intraparticle void fraction)
η	regeneration efficiency, g/MJ

Subscripts

s	solid phase
f	fluid phase
i	component property

References

[1] K.S. Walton, M.D. LeVan, A novel adsorption cycle for CO2 recovery: Experimental and theoretical investigations of a temperature swing compression process, Separation Science and Technology, 41 (3) (2006) 485-500.

[2] J.E. Finn, K.R. Sridhar, C.P. McKay, Utilization of martian atmosphere constituents by temperature-swing adsorption, Journal of the British Interplanetary Society, 49 (11) (1996) 423-430.

[3] L.M. Mulloth, J.E. Finn, A solid-state compressor for integration of CO_2 removal and reduction assemblies, SAE International 2000-01-2352.

[4] R.P. Hoover, P. C. Wankat, Gas compression using temperature swing adsorption, Separation Science and Technology 37 (14) (2002) 3187-3199.

[5] L. Mulloth, M. Varghese, B. Luna, J. Hogan, M.D. LeVan, J.R. Moate, Development of a low-power CO_2 removal and compression system for closed-loop air revitalization in future spacecraft, SAE International, Paper 2005-01-2944 (2005) 1-8.

[6] D.J. Miles, S.V. Shelton, Design and testing of a solid-sorption heat-pump system, Applied Thermal Engineering 16 (5) (1996) 389-394.

[7] B.K. Sward, M.D. LeVan, F. Meunier, Adsorption heat pump modeling: the thermal wave process with local equilibrium, Applied Thermal Engineering 20 (2000) 759-780.

[8] J. Mérel, M. Clausse, F. Meunier, Carbon dioxide capture by indirect thermal swing adsorption using 13X zeolite, Environmental Progress 25 (4) (2006) 327-333.

[9] R. Bounaceur, N. Lape, D. Roizard, C. Vallieres, E. Favre, Membrane processes for post-combustion carbon dioxide capture: A parametric study, Energy 31 (2005) 2556-2570.

[10] K.S. Walton, M.D. LeVan, Consistency of energy and material balances for bidisperse particles in fixed-bed adsorption and related applications, Industrial & Engineering Chemistry Research, 42 (26) (2003) 6938-6948.

[11] R.B. Bird, W.E. Stewart, E.N. Lightfoot, Transport Phenomena, 2nd ed.; John Wiley and Sons Inc: New York, 2002.

[12] S.M. Taqvi, W.S. Appel, M.D. LeVan, Coadsorption of organic compounds and water vapor on BPL activated carbon. 4. Methanol, ethanol, propanol, butanol, and modeling, Industrial & Engineering Chemistry Research, 38 (1) (1999) 240-250.

[13] M.S. Rosen, L.M. Mulloth, D.L. Affleck, Y. Wang, M.D. LeVan, Development and testing of a temperature-swing adsorption compressor for carbon dioxide in closed-loop air revitalization systems, SAE International, Paper 2005-01-2941 (2005) 1-6.

CHAPTER IV

FIXED-BED ADSORPTION WITH NONPLUG FLOW: PERTURBATION SOLUTION FOR CONSTANT PATTERN BEHAVIOR

4.1 Introduction

A fundamental understanding of the factors that affect breakthrough behavior is required to design and optimize an adsorption-based process. For many applications, such as those involving low breakthrough concentrations, a quantitative understanding of the phenomena that may alter the breadth of a breakthrough curve is necessary. These phenomena include, but are not limited to, external mass transfer resistances, intraparticle mass transfer resistances, the nonlinearity of adsorption isotherms, and dispersion in the axial and transverse directions.

A considerable amount of work has been performed to analyze phenomena that affect the breadth of the breakthrough curve for adsorption processes with plug-flow. For example, Costa and Rodrigues[5] demonstrate the significance of axial dispersion on the breadth of the breakthrough curve. As the Peclet number is increased the width of the breakthrough curve decreases, or tightens up. Coppola and LeVan[4] indicate the influence that fluid-solid-adsorption equilibria has on the breakthrough curve for deep beds. As an adsorption bed begins to saturate, the velocity of the adsorption wave for a very favorable adsorption isotherm approaches the fluid velocity near the bed outlet and subsequently the breakthrough is abrupt.

However, breakthrough behavior for beds of moderate to large cross-sectional area is rarely as sharp as predicted by theory based on plug flow. Only in small diameter columns and carefully packed laboratory-scale columns, including those for high-efficiency chromatography, are sharp breakthroughs found. Instead, breakthrough curves will spread based on a combined effect of deviations from plug flow including wall effects and the shape of the adsorption isotherm.

The scope of this paper involves investigating how adsorption processes described by constant pattern behavior are affected by small deviations from plug flow. Such deviations impact the breakthrough behavior at the bed outlet by saturating various radial positions of the adsorption bed at different times, in effect broadening the breakthrough curve. Deviations from plug flow exist in real adsorption beds due to nonuniform packings and channeling effects at the bed wall. Using laser-Doppler anemometry, Vortmeyer and Schuster[13] have shown experimentally that the local fluid-phase velocity varies significantly across the cross-section of the bed and is greater at the wall than at the centerline of the bed. Experiments and numerical analyses done by Miyabe and Guiochon[7] and Astrath et al.[2] also agree that the fluid-phase velocity is greater at the wall than the centerline in chromatography columns.

In comparison to the amount of work that has dealt with constant pattern behavior for plug flow, there is limited research concerning constant pattern behavior with deviations from plug flow. Tereck et al.[11] discuss the relationship among concentrations for a constant pattern profile under nonplug-flow conditions for a cylindrical channel with adsorption at the wall. They demonstrate that a constant pattern profile can be approached for adsorption with nonplug-flow-velocity profiles. Rudisill and LeVan[9] investigate adsorption of a dilute solute from fluid in nonplug-flow through a porous structure of arbitrary but constant cross section. Avilés and LeVan[3] create network models to describe nonuniform flow and nonlinear adsorption in packed beds. Although not solved for a system exhibiting constant pattern behavior, Vortmeyer and Michael[12] numerically solve the nonplug-flow gas-phase continuity equation with adsorption rates modeled by a linear driving force. They noticed that the numerical model predicted distinct differences between the breakthrough curves near the wall and the center of the bed.

In this paper, we solve the continuity equation for fixed-bed adsorption with

small deviations from plug flow, dispersion in the axial and transverse directions, and with adsorption equilibrium described by a slightly favorable isotherm. We begin by first assuming that the adsorbent bed is sufficiently long for a constant pattern adsorption wave to develop. Then, we decompose the continuity equation into a series of differential equations similar to Aris.[1] We use a perturbation analysis to obtain an approximate solution for the fluid-phase concentration. The results are general in the sense that the solution applies to perturbations of any axisymmetrical velocity profile and slightly favorable isotherm. We believe this to be the first analytical treatment of constant pattern behavior for a fixed-bed adsorber described by a nonplug-flow differential equation with axial and radial dispersion.

4.2 Theory

We examine mass transfer for axisymmetrical flow of fluid through a deep bed of packed adsorbent particles, so that the fluid-phase concentration c is a function of radius, time, and axial position only. The material balance for this system may be written

$$\rho_b \frac{\partial n}{\partial t} + \epsilon' \frac{\partial c}{\partial t} + \epsilon \vec{v} \frac{\partial c}{\partial z} = \epsilon D_r \frac{1}{r} \frac{\partial}{\partial r} \left(r \frac{\partial c}{\partial r} \right) + \epsilon D_z \frac{\partial^2 c}{\partial z^2} \tag{4.1}$$

with boundary conditions in the radial direction of

$$\left. \frac{\partial c}{\partial r} \right|_{r=0} = 0 \qquad \left. \frac{\partial c}{\partial r} \right|_{r=R_{bed}} = 0$$

where $\vec{v}$ is the local velocity which may vary across the cross section of the bed but not axially, R_{bed} is the radius of the bed, and the adsorbed-phase concentration n is described by a slightly favorable (i.e., concave downward) adsorption isotherm. D_r and D_z in equation 4.1 are molecular diffusion or dispersion coefficients in the radial

and axial directions. We let

$$\begin{array}{ccc} \xi = \dfrac{r}{R_{bed}} & z_a = \dfrac{z}{R_{bed}} & t_1 = \dfrac{\langle v \rangle t}{R_{bed}} \\ u\left(\xi\right) = \dfrac{\epsilon \vec{v}\left(\xi\right)}{\langle v \rangle} & c^* = \dfrac{c - c'}{c'' - c'} & n^* = \dfrac{n - n'}{n'' - n'} \\ Pe_r = \dfrac{2\langle v \rangle R_{bed}}{\epsilon D_r} & & Pe_a = \dfrac{2\langle v \rangle R_{bed}}{\epsilon D_z} \end{array} \tag{4.2}$$

where $\langle v \rangle$ is the mean superficial velocity, c' and n' are presaturated concentrations (zero for an initially clean bed), c'' is the feed concentration, and n'' is the corresponding adsorbed-phase concentration. Equation 4.1 becomes

$$\rho_b \frac{n'' - n'}{c'' - c'} \frac{\partial n^*}{\partial t_1} + \epsilon' \frac{\partial c^*}{\partial t_1} + u\left(\xi\right) \frac{\partial c^*}{\partial z_a} = \frac{2}{Pe_r} \frac{1}{\xi} \frac{\partial}{\partial \xi} \left(\xi \frac{\partial c^*}{\partial \xi} \right) + \frac{2}{Pe_a} \frac{\partial^2 c^*}{\partial z_a^2} \tag{4.3}$$

A new coordinate is defined to follow the stoichiometric front of the adsorption wave. We let

$$\zeta = z_a - \frac{t_1}{\Lambda + \epsilon'} \tag{4.4}$$

where Λ, the partition ratio, is given by

$$\Lambda = \rho_b \frac{n'' - n'}{c'' - c'} \tag{4.5}$$

Assuming the bed length L is large, a constant pattern profile will develop. Furthermore, for $\Lambda \gg 1$, Coppola and LeVan[4] show that the fluid-phase accumulation term in eq 4.3 is negligible, transforming it to

$$-\frac{\partial n^*}{\partial \zeta} + u\left(\xi\right) \frac{\partial c^*}{\partial \zeta} = \frac{2}{Pe_r} \frac{1}{\xi} \frac{\partial}{\partial \xi} \left(\xi \frac{\partial c^*}{\partial \xi} \right) + \frac{2}{Pe_a} \frac{\partial^2 c^*}{\partial \zeta^2} \tag{4.6}$$

with boundary conditions in the axial direction of

$$c^* \rightarrow 1 \ \text{ as } \ \zeta \rightarrow -\infty \qquad c^* \rightarrow 0 \ \text{ as } \ \zeta \rightarrow +\infty \tag{4.7}$$

We describe the local velocity by a small perturbation from plug flow using

$$u\left(\xi\right) = 1 + \gamma f\left(\xi\right) \tag{4.8}$$

where γ is the perturbation parameter for which $\gamma \ll 1$, and $f(\xi) = \mathrm{O}(1)$ is an axisymmetric term such that

$$\int_0^1 \xi f(\xi)\, d\xi = 0 \tag{4.9}$$

We solve equation 4.6 using a perturbation method with an assumed solution of the form

$$c^* = \sum_{k=0}^{\infty} \gamma^k c_k^* = c_0^* + \gamma c_1^* + \cdots \tag{4.10}$$

Substituting equation 4.10 into equation 4.6 gives the zero order differential equation

$$-\frac{\partial n_0^*}{\partial \zeta} + \frac{\partial c_0^*}{\partial \zeta} = \frac{2}{Pe_a}\frac{\partial^2 c_0^*}{\partial \zeta^2} \tag{4.11}$$

where $n_0^* = n^*(c_0^*)$.

We solve this equation following the method outlined by Coppola and LeVan[4] resulting in

$$d\zeta = \frac{2}{Pe_a}\frac{dc_0^*}{(c_0^* - n_0^*)} \tag{4.12}$$

which they integrated for Langmuir (constant separation factor) and Freundlich isotherms.

The first and second order differential equations are obtained by first writing the dimensionless adsorbed-phase concentration n^* in a Taylor series expansion of the form

$$n^* = n^*(c_0^{*\prime}) + \left.\frac{dn^*}{dc^*}\right|_{c_0^{*\prime}} \frac{(c^* - c_0^{*\prime})}{1!} + \left.\frac{d^2 n^*}{dc^{*2}}\right|_{c_0^{*\prime}} \frac{(c^* - c_0^{*\prime})^2}{2!} + \cdots \tag{4.13}$$

where $c_0^{*\prime}$ is the point at which the loading is centered. The subsequent example, centered about the plug-flow solution, shows that when taking the partial derivative of the Taylor series expansion with respect to ζ, the terms $\partial(d^k n^* / dc^{*k}\big|_{c_0^{*\prime}})/\partial\zeta$ for $k > 1$ can be neglected for slightly favorable isotherms. The first and second order terms are then described by

$$-\left.\frac{dn^*}{dc^*}\right|_{c_0^*} \frac{\partial c_1^*}{\partial \zeta} + f(\xi)\frac{\partial c_0^*}{\partial \zeta} + \frac{\partial c_1^*}{\partial \zeta} = \frac{2}{Pe_r}\frac{1}{\xi}\frac{\partial}{\partial \xi}\left(\xi \frac{\partial c_1^*}{\partial \xi}\right) + \frac{2}{Pe_a}\frac{\partial^2 c_1^*}{\partial \zeta^2} \tag{4.14}$$

and

$$-\left.\frac{dn^*}{dc^*}\right|_{c_0^*}\frac{\partial c_2^*}{\partial\zeta}+f\left(\xi\right)\frac{\partial c_1^*}{\partial\zeta}+\frac{\partial c_2^*}{\partial\zeta}+2c_1^*\left.\frac{d^2n^*}{dc^{*2}}\right|_{c_0^*}\frac{\partial c_1^*}{\partial\zeta}=\frac{2}{Pe_r}\frac{1}{\xi}\frac{\partial}{\partial\xi}\left(\xi\frac{\partial c_2^*}{\partial\xi}\right)+\frac{2}{Pe_a}\frac{\partial^2 c_2^*}{\partial\zeta^2} \tag{4.15}$$

Following Taylor,[10] we assume that the time necessary for appreciable effects to appear due to convective transport is long compared with that needed for the radial variations to be reduced to a fraction of their initial value due to molecular diffusion, i.e., axial derivatives are independent of radial position. After integrating the first order equation radially and applying both radial boundary conditions, we obtain

$$-\left.\frac{dn^*}{dc^*}\right|_{c_0^*}\frac{\partial c_1^*}{\partial\zeta}+\frac{\partial c_1^*}{\partial\zeta}=\frac{2}{Pe_a}\frac{\partial^2 c_1^*}{\partial\zeta^2} \tag{4.16}$$

A solution for c_1^* is assumed of the form

$$c_1^*=g\left(\zeta\right)+\frac{Pe_r}{2}\frac{dc_0^*}{d\zeta}\int_0^\xi\frac{\int_0^{\xi'}\xi''f\left(\xi''\right)d\xi''}{\xi'}d\xi' \tag{4.17}$$

Substituting equation 4.17 into equation 4.14 we obtain

$$-\left.\frac{dn^*}{dc^*}\right|_{c_0^*}\frac{\partial g}{\partial\zeta}+\frac{\partial g}{\partial\zeta}=\frac{2}{Pe_a}\frac{\partial^2 g}{\partial\zeta^2} \tag{4.18}$$

Integrating equation 4.18 by parts gives

$$\left(1-\left.\frac{dn^*}{dc^*}\right|_{c_0^*}\right)g=\frac{2}{Pe_a}\frac{dg}{d\zeta} \tag{4.19}$$

After substituting equation 4.12 into equation 4.19 and integrating, we obtain the solution for the axial contribution of the first order term, $g\left(\zeta\right)$, in the form

$$g\left(\zeta\right)=B_1\exp\left[\int\left(1-\left.\frac{dn^*}{dc^*}\right|_{c_0^*}\right)\frac{dc_0^*}{\left(c_0^*-n^*|_{c_0^*}\right)}\right] \tag{4.20}$$

which when substituted in equation 4.17 yields

$$c_1^*=B_1\exp\left[\int\left(1-\left.\frac{dn^*}{dc^*}\right|_{c_0^*}\right)\frac{dc_0^*}{\left(c_0^*-n^*|_{c_0^*}\right)}\right]+\frac{Pe_r}{2}\frac{dc_0^*}{d\zeta}\int_0^\xi\frac{\int_0^{\xi'}\xi''f\left(\xi''\right)d\xi''}{\xi'}d\xi' \tag{4.21}$$

The method for evaluating the second order term is the same as the one outlined above for the first order term. The example demonstrates that the radial terms

in the second order differential equation are also negligible, resulting in a solution of the form

$$c_2^* = -B_2 \exp\left[\int \left(1 - \left.\frac{dn^*}{dc^*}\right|_{c_0^*}\right) \frac{dc_0^*}{\left(c_0^* - n^*|_{c_0^*}\right)}\right] \tag{4.22}$$

B_1 and B_2 are constants of integration which are evaluated to center the adsorbed-phase transition at $\zeta = 0$ as seen in Figure 4.1. For the adsorbed-phase transition to be centered stoichiometrically at $\zeta = 0$ the area of the two shaded regions must be equal, as illustrated by Coppola and LeVan[4] and Rodrigues et al.[8] Thus, we have

$$\int_{-\infty}^{0} \left(1 - \overline{n^*}\right) d\zeta = \int_{0}^{+\infty} \overline{n^*} d\zeta \tag{4.23}$$

with

$$\overline{n^*} = \frac{\int_0^1 \xi n^* d\xi}{\int_0^1 \xi d\xi} \tag{4.24}$$

Example

The solution above pertains to any fixed-bed adsorber exhibiting constant pattern behavior with an axisymmetric piecewise continuous velocity profile and a slightly favorable isotherm. As an example of the application of the more general results, we evaluate the solution for a Langmuir isotherm, written in the dimensionless constant separation factor form

$$n^* = \frac{c^*}{R + (1 - R)\, c^*} \tag{4.25}$$

where R is the separation factor given by LeVan and Carta.[6]

$$R = r_{sep} + (1 - r_{sep}) \left(\frac{c'}{c''}\right) \tag{4.26}$$

with

$$r_{sep} = \frac{1}{1 + Kc''} \tag{4.27}$$

$R = 1$ gives a linear isotherm, and $R = 0$ corresponds to the rectangular (or irreversible) isotherm. Our solution applies to R slightly less than unity.

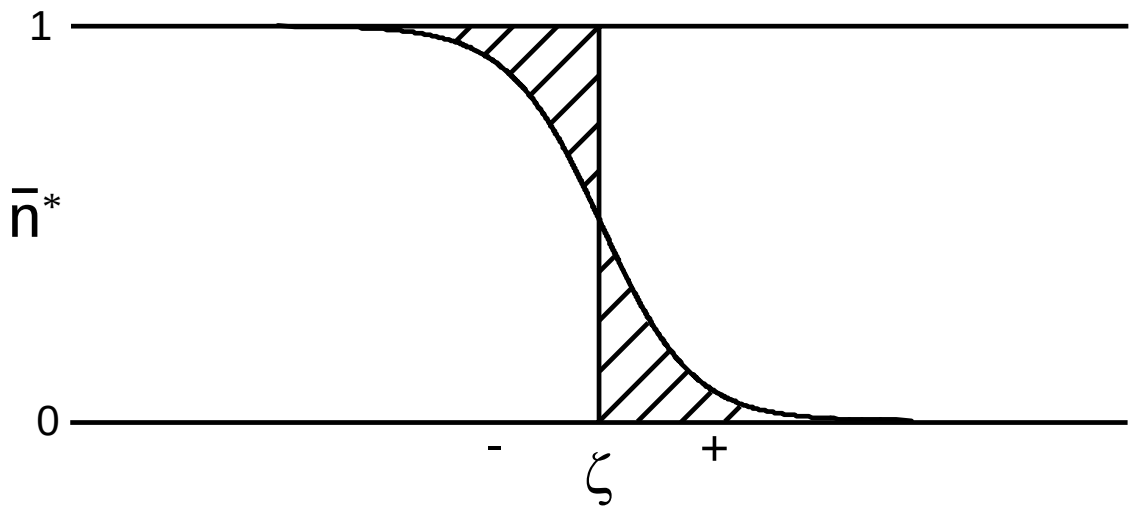

Figure 4.1: Material balance for centering profile at $\zeta = 0$.[6]

The Taylor series expansion of the Langmuir isotherm about the zeroth order solution, c_0^*, is given by

$$n^* = \frac{c_0^*}{R+(1-R)\,c_0^*} + \frac{R}{\left[R+(1-R)\,c_0^*\right]^2}\left(\gamma c_1^* + \gamma^2 c_2^*\right) + \frac{R\,(1-R)}{\left[R+(1-R)\,c_0^*\right]^3}\left(\gamma c_1^* + \gamma^2 c_2^*\right)^2 + \cdots \tag{4.28}$$

Taking the axial derivative of equation 4.28 gives

$$\begin{aligned}\frac{\partial n^*}{\partial \zeta} = {} & \frac{R}{\left[R+(1-R)\,c_0^*\right]^2}\frac{\partial c_0^*}{\partial \zeta} + \gamma\frac{R}{\left[R+(1-R)\,c_0^*\right]^2}\frac{\partial c_1^*}{\partial \zeta} \\ & -\gamma\frac{2R\,(1-R)}{\left[R+(1-R)\,c_0^*\right]^3}\frac{dc_0^*}{d\zeta}c_1^* + O\left(\gamma^2\right)\end{aligned} \tag{4.29}$$

After substituting equations 4.10 and 4.29 into equation 4.6 and rearranging, the zeroth, first, and second order differential equations are

$$\frac{\partial c_0^*}{\partial \zeta} = \frac{Pe_a}{2}\frac{c_0^*\,(1-R)\,(c_0^*-1)}{R+(1-R)\,c_0^*} \tag{4.30}$$

$$\begin{aligned}&\left[1-\frac{R}{\left[R+(1-R)\,c_0^*\right]^2}\right]\frac{\partial c_1^*}{\partial \zeta} + f\,(\xi)\,\frac{\partial c_0^*}{\partial \zeta} + \frac{2R\,(1-R)}{\left[R+(1-R)\,c_0^*\right]^3}\frac{dc_0^*}{d\zeta}c_1^* \\ &\qquad = \frac{2}{Pe_r}\frac{1}{\xi}\frac{\partial}{\partial \xi}\left(\xi\frac{\partial c_1^*}{\partial \xi}\right) + \frac{2}{Pe_a}\frac{\partial^2 c_1^*}{\partial \zeta^2}\end{aligned} \tag{4.31}$$

and

$$\begin{aligned}&\left[1-\frac{R}{\left[R+(1-R)\,c_0^*\right]^2}\right]\frac{\partial c_2^*}{\partial \zeta} + f\,(\xi)\,\frac{\partial c_1^*}{\partial \zeta} + \frac{2R\,(1-R)}{\left[R+(1-R)\,c_0^*\right]^3}\frac{dc_0^*}{d\zeta}c_2^* - \\ &\qquad \frac{2Rc_1^*\,(1-R)}{\left[R+(1-R)\,c_0^*\right]^3}\frac{dc_1^*}{d\zeta}c_2^* + \frac{3R\,(1-R)^2}{\left[R+(1-R)\,c_0^*\right]^4}\frac{dc_0^*}{d\zeta}c_1^{*2} \\ &\qquad = \frac{2}{Pe_r}\frac{1}{\xi}\frac{\partial}{\partial \xi}\left(\xi\frac{\partial c_2^*}{\partial \xi}\right) + \frac{2}{Pe_a}\frac{\partial^2 c_2^*}{\partial \zeta^2}\end{aligned} \tag{4.32}$$

respectively. The third term of equation 4.31 and the second, third, fourth, and fifth terms of equation 4.32 are $\mathrm{O}\left((1-R)^2\right)$ or greater and are therefore negligible since as R approaches unity they approach zero faster than the other terms. This assumption is only valid for the conditions in which the quantity $(1-R)^2 \leq 0.0025$, i.e., $0.95 \leq R \leq 1$.

The zeroth order term is solved by decomposing equation 4.30 by the method of partial fractions. These are then integrated to give

$$\zeta = \frac{2}{Pe_a}\left(\frac{1}{1-R}\right)\ln\frac{1-c_0^*}{c_0^{*R}} \tag{4.33}$$

where the constant of integration has been determined by Coppola and LeVan[4] to be zero from the relationship in equation 4.23.

The axial component of the first order term is determined from

$$g(\zeta) = B_1 \exp\left[\int \left(1 - \frac{R}{\left[R + (1-R)\, c_0^*\right]^2}\right) \frac{R + (1-R)\, c_0^*}{c_0^* (1-R)\left(c_0^* - 1\right)} dc_0^*\right] \tag{4.34}$$

Using the solution found in equation 4.33 and the method of partial fractions, equation 4.34 is solved to give

$$g(\zeta) = B_1 \frac{\partial c_0^*}{\partial \zeta} \tag{4.35}$$

The first and second order terms now have the forms

$$c_1^* = -\frac{\partial c_0^*}{\partial \zeta}\left\{B_1 - \frac{Pe_r}{2}\left[\int_0^\xi \left(\frac{\int_0^{\xi'} \xi'' f(\xi'')\, d\xi''}{\xi'}\right) d\xi'\right]\right\} \tag{4.36}$$

and

$$c_2^* = B_2 \frac{\partial c_0^*}{\partial \zeta} \tag{4.37}$$

Substituting equations 4.36 and 4.37 into equation 4.28 and using the relationships found in equations 4.23 and 4.24 the term c_1^* is then written

$$c_1^* = \frac{\partial c_0^*}{\partial \zeta}\frac{Pe_r}{2}\left\{\int_0^\xi \left(\frac{\int_0^{\xi'} \xi'' f(\xi'')\, d\xi''}{\xi'}\right) d\xi' - 2\int_0^1 \xi \left[\int_0^\xi \left(\frac{\int_0^{\xi'} \xi'' f(\xi'')\, d\xi''}{\xi'}\right) d\xi'\right] d\xi\right\} \tag{4.38}$$

with the axial Peclet number factored into the term $\frac{\partial c_0^*}{\partial \zeta}$ as seen in equation 4.30. Subsequently we then determine the solution for this example for two velocity profiles, the first a laminar deviation from plug flow and a plug-flow velocity profile with wall effects.

Parabolic Perturbation from Plug Flow

A laminar deviation is introduced to the velocity profile by replacing the $f(\xi)$ term found in equation 4.8 with

$$f(\xi) = 1 - 2\xi^2 \tag{4.39}$$

Substituting this into equation 4.38, the concentration profile is solved to give

$$c^* = c_0^* - \frac{\gamma}{4}\frac{Pe_r}{2}\frac{dc_0^*}{d\zeta}\left[\frac{1}{3} - \left(\xi^2 - \frac{\xi^4}{2}\right)\right] \tag{4.40}$$

We evaluate the first order correction term for the fluid-phase concentration for an isotherm with $R = 0.95$, axial and radial Peclet numbers of 100, and a velocity profile perturbation parameter γ of 0.1. Here we assume that the velocity is low enough that the effects of molecular diffusion dominate those of dispersion, i.e., the axial and radial Peclet numbers are equal. Figure 4.2 shows the first order correction term plotted against the dimensionless axial distance ζ. As ζ approaches $-\infty$ and $+\infty$, the first order correction term becomes negligible and the concentration wave approaches asymptotic values determined by the feed and presaturated concentrations. However, near the stoichiometric center of the adsorbed-phase transition, the first order correction term has a sizable impact on the fluid-phase concentration.

A comparison of concentration profiles evaluated from the plug-flow model and the plug-flow model with a laminar deviation is shown in Figure 4.3. The dimensionless concentrations c_0^* and c^* have been plotted versus the dimensionless axial distance ζ, where they have been centered stoichiometrically using the adsorbed-phase transition. As expected, when there is a slight deviation from plug flow, a radial gradient of concentration forms based on the shape of the velocity profile. For the case shown in Figure 4.3, the concentration at the centerline moves slightly ahead of the plug-flow solution while the concentration at the wall is slightly delayed.

In Figure 4.4 the lines of constant concentration are similar in shape to that of the quadratic plug-flow perturbation used. Because of this, breakthrough will occur at different times over the radial position in the bed, occurring earlier at the centerline and later at the wall.

It is interesting to note that taking the cross-sectional average of equation 4.40 collapses the solution for the fluid-phase concentration to that of the zeroth

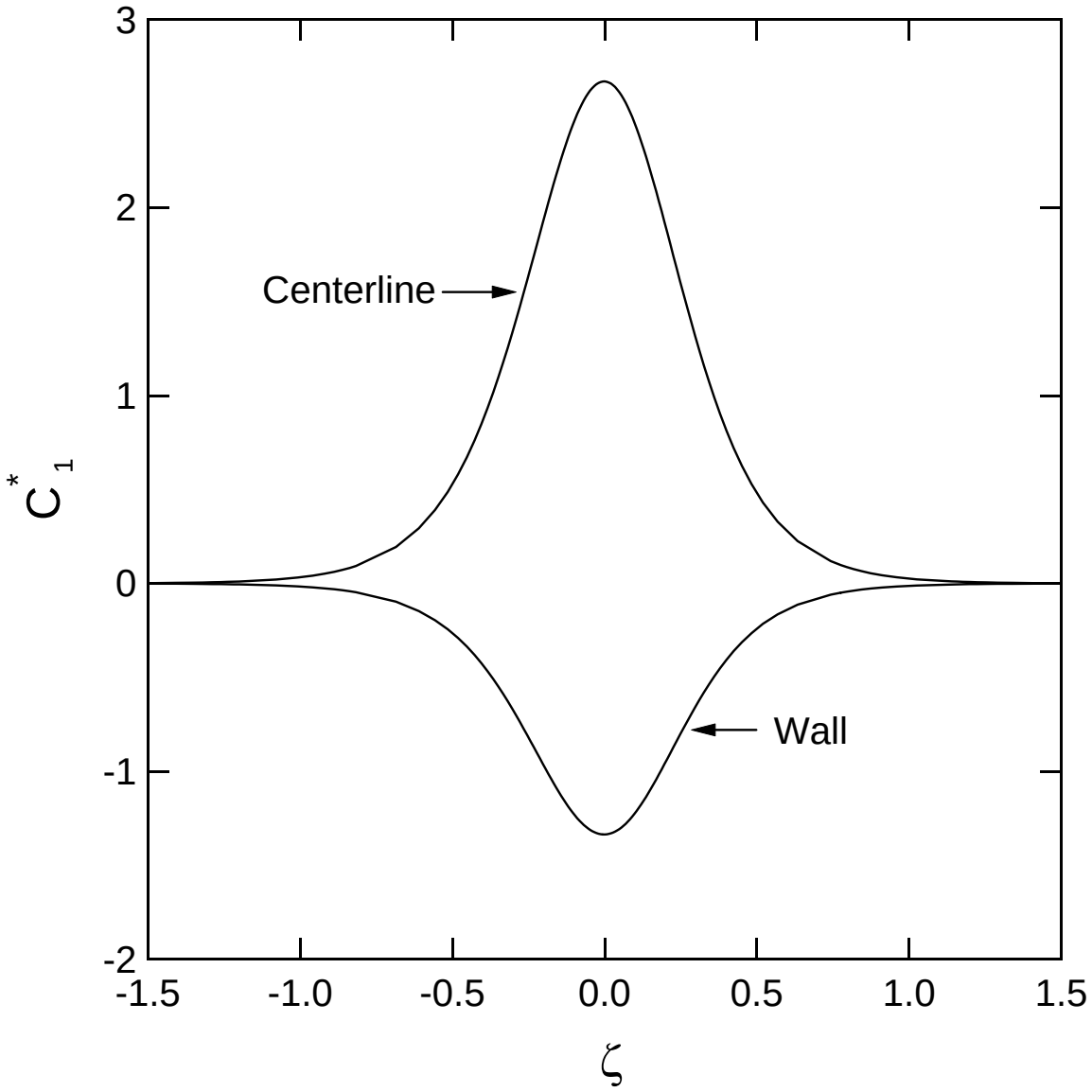

Figure 4.2: First-order correction term along the centerline of the bed and the wall as a function of axial position for the parabolic velocity example.

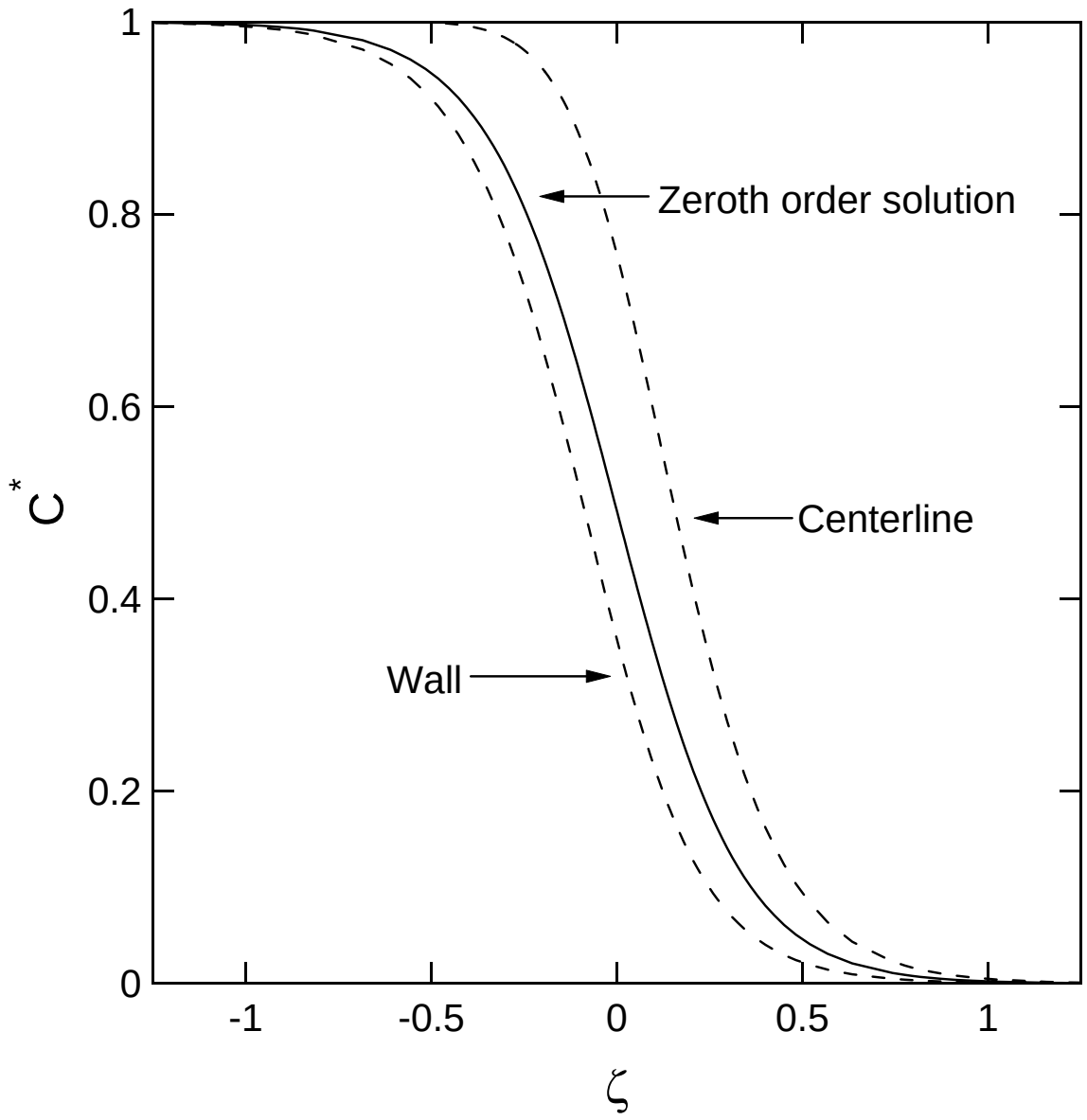

Figure 4.3: Example curves of fluid-phase concentrations with slightly favorable Langmuir isotherms for $\gamma = 0.1$, $R = 0.95$, $Pe_r = Pe_a = 100$, and $f(\xi) = 1 - 2\xi^2$.

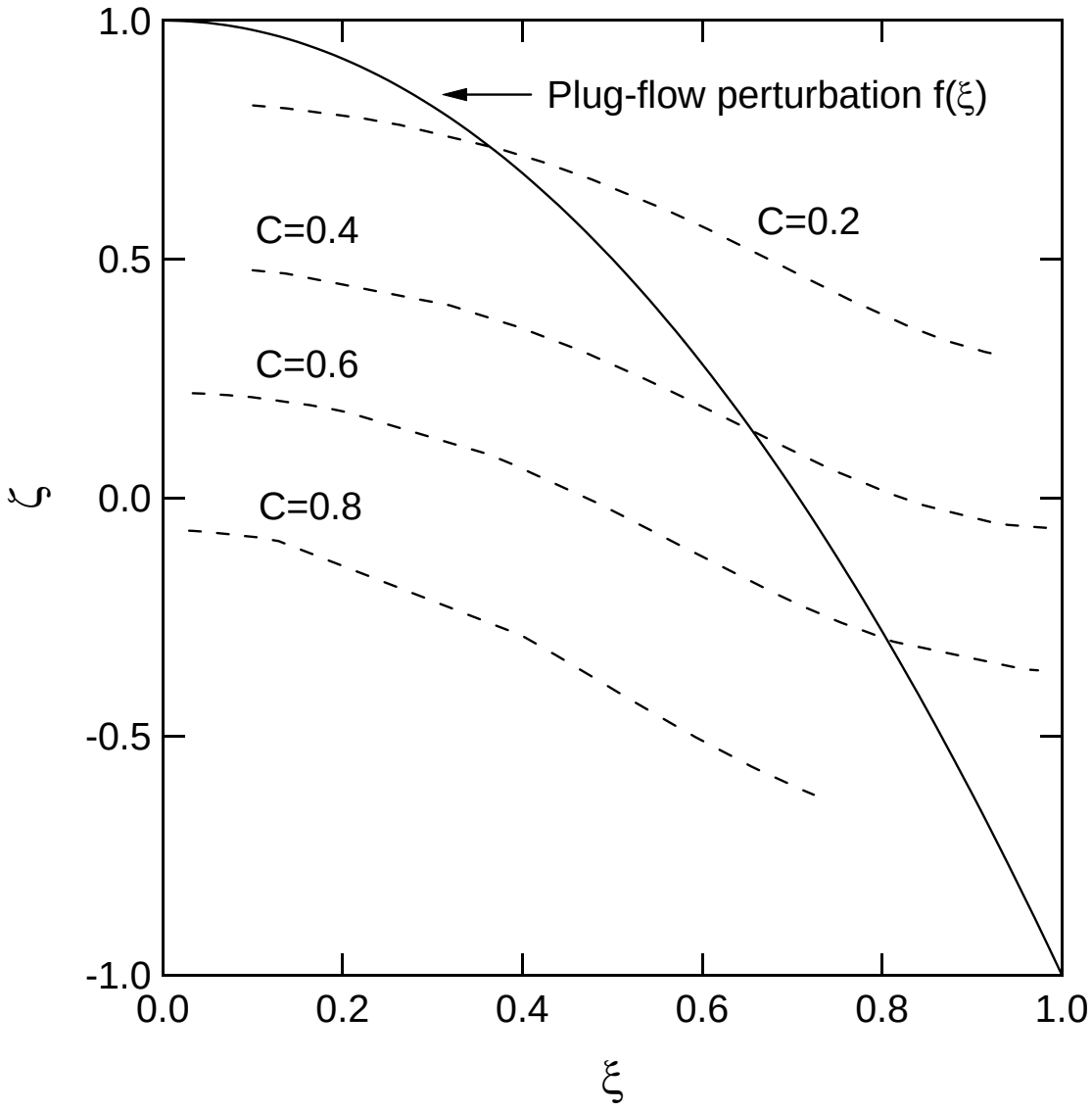

Figure 4.4: Lines of constant concentrations and plug-flow perturbation in a packed bed for slightly favorable Langmuir isotherm for $\gamma = 0.1$, $R = 0.95$, $Pe_r = Pe_a = 100$, and $f(\xi) = 1 - 2\xi^2$.

order solution. However, the mixing-cup concentration given by

$$\overline{c^*} = \frac{\int_A uc^*\, dA}{\langle u \rangle A} \tag{4.41}$$

differs from the plug-flow solution. As the fluid flow increasingly diverges from plug flow, the mixing-cup concentration continues to broaden, diverging from the plug-flow model prediction.

Wall Effect

To model a plug-flow velocity profile with wall effects, we exchange the quadratic function found in 4.39 for that of a piecewise-continuous function written as

$$f(\xi) = \begin{cases} \frac{\left(a^2-1\right)}{a^2}, & 0 \leq \xi < a \\ 1, & a \leq \xi \leq 1 \end{cases} \tag{4.42}$$

Solving for the concentration profile with this velocity profile gives

$$c^* = \begin{cases} c_0^* - \gamma \frac{dc_0^*}{d\zeta} \frac{Pe_r}{2} \left(h(a) - \frac{a^2-1}{a^2} \frac{\xi^2}{4} \right), & 0 \leq \xi < a \\ c_0^* - \gamma \frac{dc_0^*}{d\zeta} \frac{Pe_r}{2} \left(h(a) - \frac{\xi^2}{4} + \frac{1}{2} \ln \xi - \frac{1}{2} \ln a + \frac{1}{4} \right), & a \leq \xi \leq 1 \end{cases} \tag{4.43}$$

with

$$h(a) = \frac{1}{8} + \frac{1}{2} \ln a - \frac{1}{8} a^2 \tag{4.44}$$

As before we evaluate the first order correction term for the fluid-phase concentration for an isotherm with $R = 0.95$, axial and radial Peclet numbers of 100, and a velocity profile perturbation parameter γ of 0.1. Again, we assume that molecular diffusive forces dominate and can equate the axial and radial Peclet numbers. Figure 4.5 depicts the first order correction term plotted against the dimensionless axial distance ζ. Similarly to the previous velocity profile the first order correction term becomes negligible and the concentration wave approaches asymptotic values determined by the feed and presaturated conditions for values of ζ approaching $-\infty$ and $+\infty$, but has a significant impact on the fluid-phase concentration near the stoichiometric center of the adsorbed-phase transition wave. Though when Figures 4.2 and 4.5 are compared with each other it can be seen that the magnitude and the sign in

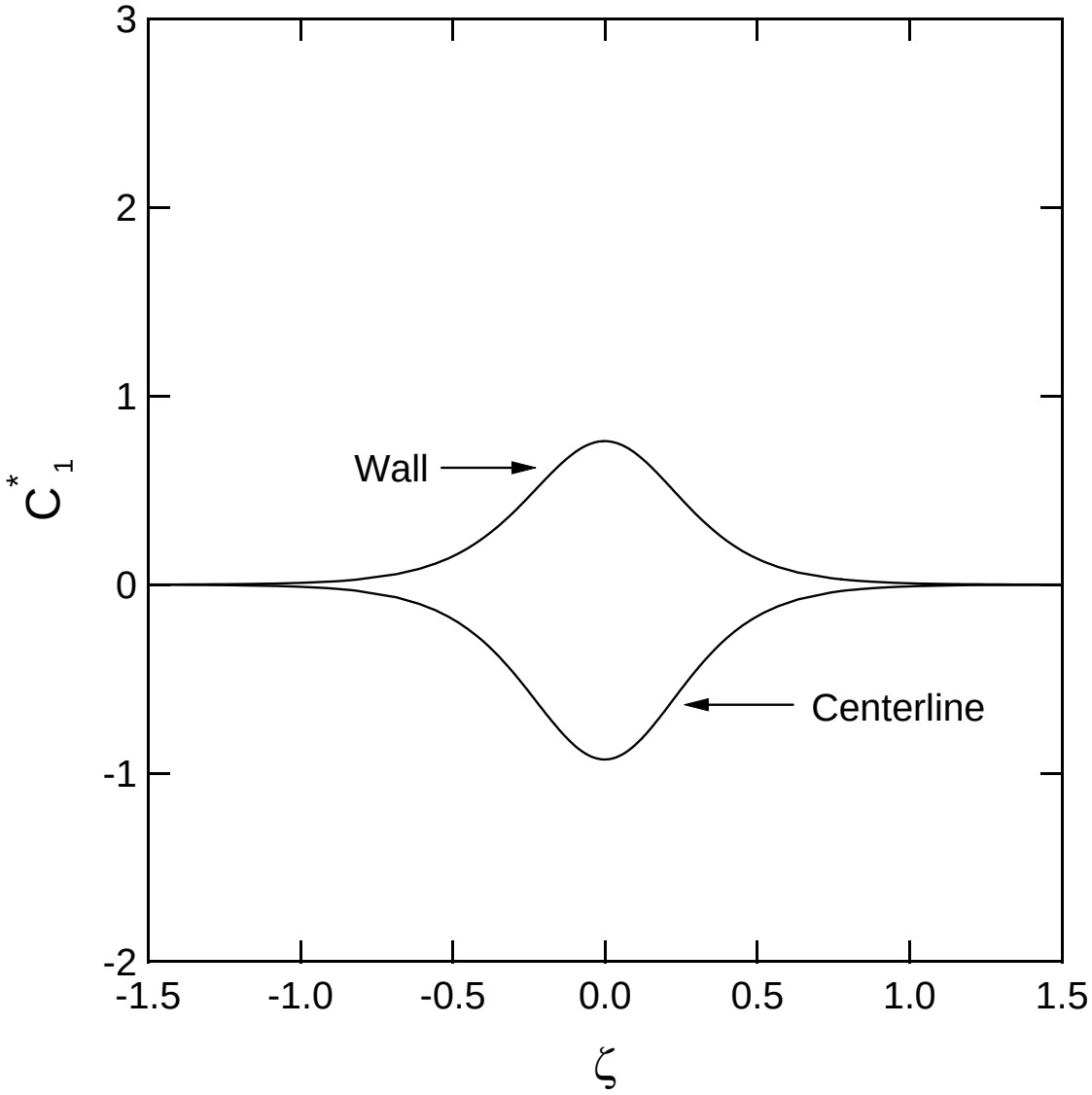

Figure 4.5: First-order correction term along the centerline of the bed and the wall as a function of axial position for the plug-flow velocity with wall effects example.

which the first correction term affects the fluid-phase concentration are different. The magnitude of the first order correction term is lower for the plug-flow velocity profile with wall effects since the area in which the fluid-phase velocity is at a maximum and minimum covers a larger percentage of the entire cross-sectional area, while the sign is opposite due to the maximum velocity occurring at the wall and not the centerline.

Figure 4.6 shows the concentration profiles evaluated from the plug-flow model and the plug-flow model with wall effects. Here the dimensionless concentrations stoichiometrically centered about the adsorbed-phase transition are plotted versus the dimensionless axial distance. As before with the plug-flow velocity profile with a laminar deviation, there is radial gradient based on the shape of the velocity profile. In this case the concentration at the wall moves slightly ahead of the plug-flow model while the concentration at the centerline is slowed.

In Figure 4.7 the lines of constant concentration are plotted in conjunction with the velocity profile used in the model. Here the open and closed circles describe the point of discontinuity at a. It can be inferred from Figures 4.4 and 4.7 that the shapes of the lines of constant concentration are highly dependent on the shape of the velocity profile used in the model. In the case in which wall effects are considered, breakthrough occurs more readily at the walls than the centerline due to the channeling effects considered in the velocity profile.

Unlike the case of the plug-flow velocity profile with a laminar deviation, the difference between the mixing cup concentration and the plug-flow velocity profile is negligible. This is due to the weaker magnitude of the first order correction term. As such the extent of the deviation of the mixing-cup concentration compared with that of the plug-flow model is dependent not only on the perturbation parameter but also the magnitude of the first order correction term.

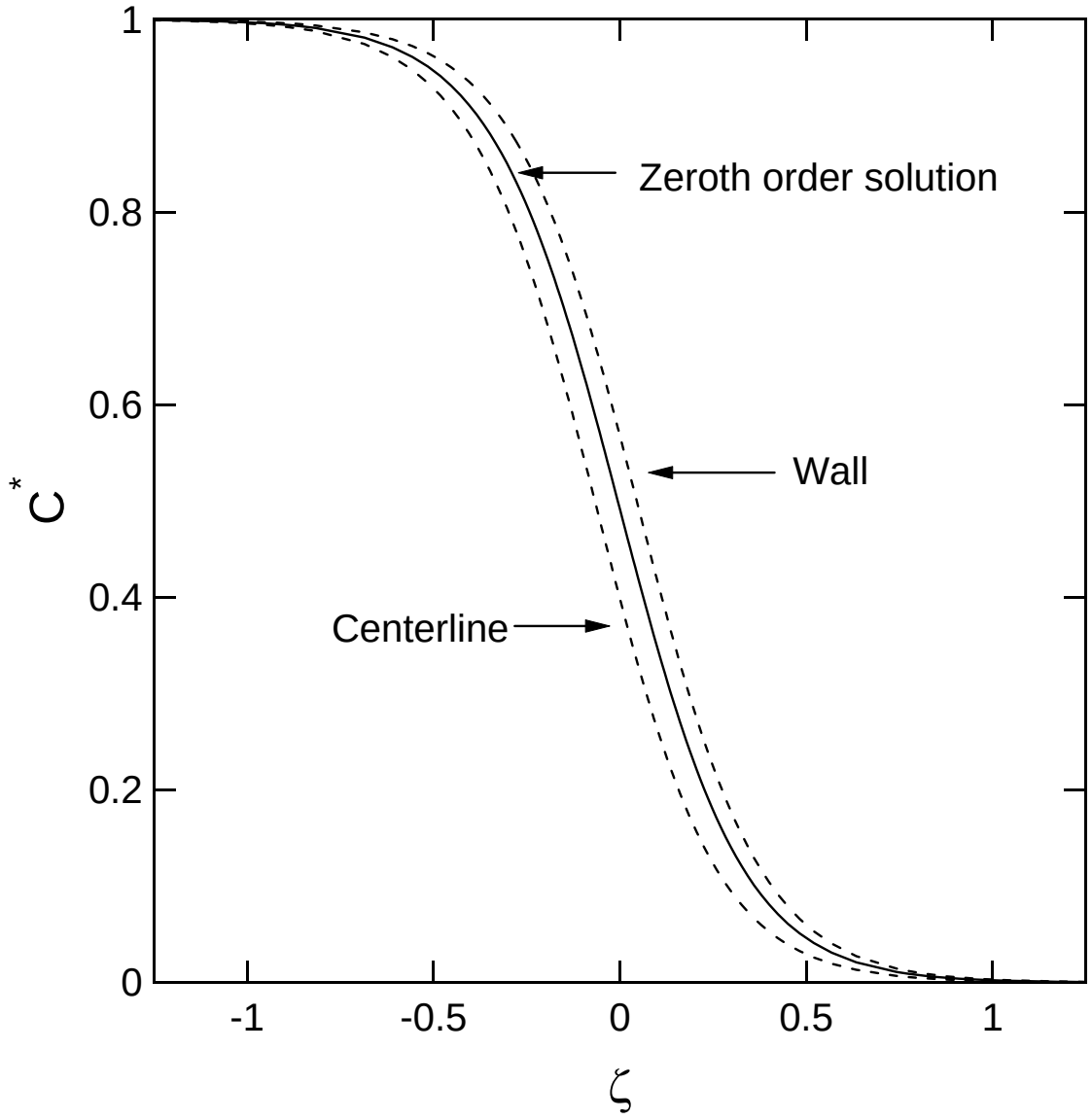

Figure 4.6: Example curves of fluid-phase concentrations with slightly favorable Langmuir isotherms for $\gamma = 0.1$, $R = 0.95$, $Pe_r = Pe_a = 100$, $a = 0.9$, and $f(\xi) = \begin{cases} \frac{(a^2-1)}{a^2}, & 0 \leq \xi < a \\ 1, & a \leq \xi \leq 1 \end{cases}$.

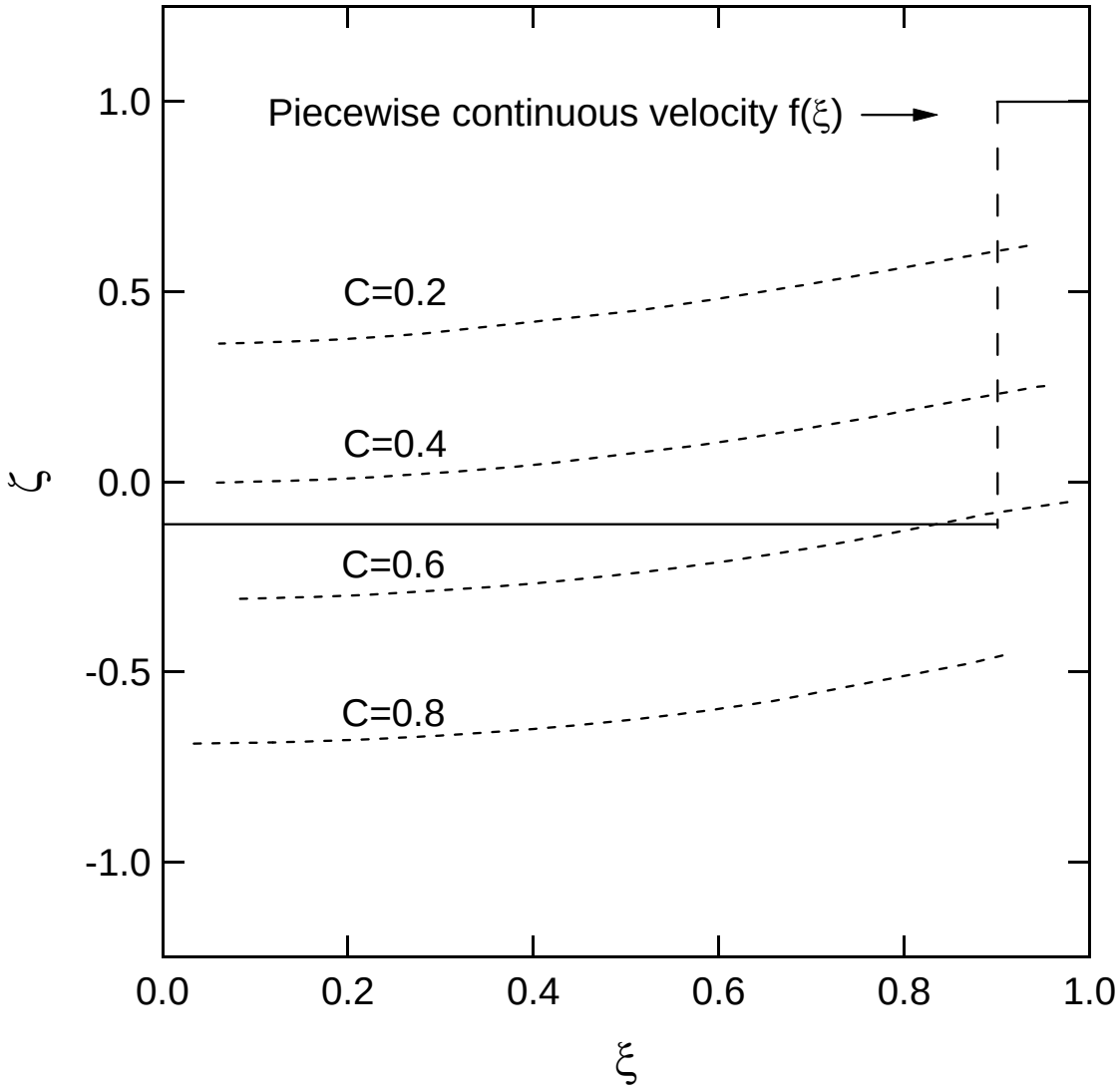

Figure 4.7: Lines of constant concentrations and plug-flow velocity with wall effects in a packed bed for slightly favorable Langmuir isotherm for $\gamma = 0.1$, $R = 0.95$, $Pe_r = Pe_a = 100$, $a = 0.9$, and $f(\xi) = \begin{cases} \frac{(a^2-1)}{a^2}, & 0 \le \xi < a \\ 1, & a \le \xi \le 1 \end{cases}$.

4.3 Conclusions

A generalized perturbation solution has been developed for a constant pattern profile of the nonplug-flow fixed-bed adsorption continuity equation. The velocity profile is described by an axisymmetric function, and the adsorbed-phase concentration is expressed by a slightly favorable isotherm. The evaluation performed in this paper extends to the first and second order terms considering both axial and transverse gradients in the fluid-phase concentration. As such, the fluid-phase concentration is described by a plug-flow model with a radial correction term.

For the condition considered, the radial variations of concentration are small compared to those in the axial direction, making the cross-sectionally averaged concentration indiscernible from the solution to the plug-flow model. However, the mixing-cup concentration moves ahead of and behind what the plug-flow model predicts based on the magnitude of the perturbation parameter in the velocity profile and of the first order correction term.

The solution for the constant pattern profile of the nonplug-flow fixed-bed adsorption continuity equation shows that a radial gradient of the fluid-phase concentration will form based on the shape of the velocity profile. This in turn influences the breakthrough behavior at the bed outlet, causing breakthrough to occur nonuniformly across the bed outlet, but with transverse dispersion attenuating the effect in comparison with the extent of the deviations from plug flow in the velocity profile. The magnitude of this outcome is important in designing adsorption-based systems where it is necessary to have low breakthrough concentrations and high utilization of the adsorbent. By being able to describe the impacts any deviations from plug flow will have on the fluid-phase concentration and thus the breakthrough behavior, it is possible to improve designs of fixed-bed adsorbers and chromatographic processes.

Notation:

a	radial position
A	cross-sectional area, m^2
B_1, B_2	constants of integration
c	fluid-phase concentration, mol/m^3
D	diffusion coefficient, m^2/s
D_z	diffusion coefficient in the z-direction, m^2/s
f	generalized velocity profile function, Eq. 4.8
g	function describing axial contribution in first order solution, Eq. 4.17
h	function dependent on a
K	isotherm parameter
n	adsorbed-phase concentration, mol/kg
$\overline{n}$	cross-sectionally averaged adsorbed-phase concentration, Eq. 4.24
Pe	Peclet number, Eq. 4.2
r	radial coordinate, m
r_{sep}, R	separation factor
R_{bed}	bed radius, m
t	time, s
t_1	dimensionless time, Eq. 4.2
u	dimensionless velocity, Eq. 4.2
$\vec{v}$	local velocity, m/s
$\langle v \rangle$	superficial velocity, m/s
z	axial coordinate, m
z_a	dimensionless axial coordinate, Eq. 4.2

Greek Letters

ϵ	void fraction of packing
ϵ'	total bed voidage
γ	perturbation parameter
Λ	partition ration, Eq. 4.5
ρ_b	bulk density, kg/m^3
ξ	dimensionless radial coordinate
ζ	dimensionless moving axial coordinate, Eq. 4.4

Superscripts

$'$	presaturated conditions
$''$	feed concentrations
$*$	nondimensionalized concentrations

Subscripts

r	radial
a	axial
0	zeroth order solution
1	first order solution

References

[1] R. Aris, On the dispersion of a solute in a fluid flowing through a tube. Proceedings of the Royal Society of London. Series A, Mathematical and Physical Sciences, 235, (1956) 67-77.

[2] Astrath D.U., Lottes F., Vu D.T., Arlt W., Stenby E.H., Experimental investigation of liquid chromatography cloumns by means of computed tomography. Adsorption, 13, (2007) 9-19.

[3] Aviles B.E., LeVan M.D., Network models for nonuniform Flow and adsorption in fixed beds. Chemical Engineering Science, 46, (1991) 1935-1944.

[4] Coppola A.P., LeVan M.D., Adsorption with axial diffusion in deep beds. Chemical Engineering Science, 36, (1981) 967-971.

[5] Costa C.,Rodrigues A., Design of cyclic fixed-bed adsorption processes part I: phenol adsorption on polymeric adsorbents. American Institute of Chemical Engineers Journal, 31, (1985) 1655-1665.

[6] LeVan M.D., Carta G., Section 16: Adsorption and ion exchange, in: Green D.W. & Maloney J.O. (Eds.), Perry's Chemical Engineers' Handbook, 8th ed.; Mcgraw-Hill: New York, (2008) p.16-15.

[7] Miyabe K., Guiochon G., Influence of column radial heterogeneity on peak fronting in linear chromatography. Journal of Chromatography A, 857, (1999) 69-87

[8] Rodrigues A.E., LeVan M.D., Tondeur D., Asymptotic fixed-bed behaviour: proportionate and constant patterns, in: Kluwer Academic Publishers (Eds.), Adsorption: Science and Technology, Dordrecht, (1989) p.149.

[9] Rudisill E., LeVan M.D., Constant pattern behavior for adsorption processes with nonplug flow. Industrial & Engineering Chemistry Research, 30, (1991) 1054-1060.

[10] Taylor G., Dispersion of soluble matter in solvent flowing slowly through a tube. Proceedings of the Royal Society of London. Series A, Mathematical and Physical Sciences, 219, (1953) 186-203.

[11] Tereck C.D., Kovach D.S., LeVan M.D., Constant-Pattern behavior for adsorption on the wall of a cylindrical channel. Industrial & Engineering Chemistry Research, 26, (1987) 1222-1227.

[12] Vortmeyer D., Michael K., The Effect of non-uniform flow distribution on concentration profiles and breakthrough curves of fixed bed adsorbers. Chemical Engineering Science, 40, (1985) 2135-2138.

[13] Vortmeyer D., Schuster J., Evaluation of steady flow profiles in rectangular and circular packed beds by a variational method. Chemical Engineering Science, 38, (1983) 1691-1699.

CHAPTER V

DEHYDRATION PERFORMANCE OF A NAFION® MEMBRANE MODULE WITH A SHELL SIDE VACUUM

5.1 Introduction

The regulation of water vapor has become increasingly important in recent years with much of the focus on the use of membrane sheets in polymer electrolyte fuel cells (PEFCs). However, as the number of applications requiring the same strict control as a PEFC increase, shell and tube membranes are being developed and investigated for use in the drying of process streams. Compared with other means of dehydration, such as the use of desiccant adsorbents, these shell and tube modules offer a potentially more energy efficient and compact method of dehydration.

Of the materials that have been established for use in dehydration applications, Nafion® has a high water selectivity and wide application in electrochemical processes. Nafion® is a copolymer of teflon and poly(perfluorosulfonic acid) in which water is transported from one interface to another through sulfonic acid channels. An important aspect of this is that the rate at which water binds as water-of-hydration and the rate at which water is transported within is closely tied to the degree of hydration of the membrane itself,[3,4,11,12] and thus the partial pressure of water vapor at each interface.

Several investigators have studied the dependency of water transport properties on the degree of hydration and have developed relationships for the diffusion coefficient and adsorption isotherm based on the partial pressure of water present within the membrane.[3,4,11,12] Springer et al.[6] measure water diffusion coefficients, water adsorption isotherms, and membrane conductivities in order to develop an isothermal, one-dimensional, steady-state model for a complete PEFC using a Nafion® membrane, and successfully verified some of their model's predictions experimentally.

These water adsorption isotherms were then used to develop a model for the diffusion coefficient based on the membrane's permeability by Ye and LeVan,[9] in which a three resistance model was considered.

Most of the research concerning Nafion® membranes has been focused on their use as thin sheets in PEFCs. However, the investigation of water transport properties done by Ye and LeVan[9] used the material in a concentric tube arrangement operating in a counter-current fashion consisting of a single tube. They were able to develop concentration profiles along the length of the membrane for flow rates ranging from 2 to 10 slpm. In a second paper, Ye and LeVan[10] characterized a shell and tube membrane module containing 50 tubes, in which they determined that not only does membrane thickness have a significant impact in determining the mass transfer resistances, but skin resistances do as well.

Recently, Nafion® membranes have interested NASA for use in dehydrating gas streams as a pretreatment for air revitalization. Since the majority of energy used in revitalizing the cabin air is involved in removing the water, utilizing a membrane could greatly reduce the energy requirements of air revitalization as predicted by Ye and LeVan.[9] For manned-space flight, it is typically desired to recuperate the water removed from the feed stream in the purge. However, in certain circumstances it is more important to reduce the mass and power consumption of the process than it is to recycle the water, such as in air revitalization systems proposed for NASA's crew exploration vehicle (CEV). In this case, replacing the purge gas on the shell side of the membrane with a vacuum could conserve the drying performance of the membrane module.

The scope of this work is to investigate the drying performance of a multi-tube Nafion® membrane module housed in a shell and operated with a vacuum on the purge side. We are interested in the integrity of the membrane and transport rates of water through the membrane with flow through the tubes and a vacuum applied

Table 5.1: Table of membrane dimensions.

N_t	100
L	1.1 m
Tube ID	0.64 mm
Tube OD	0.84 mm
l_m	0.1 mm
Shell ID	12.7 mm

on the shell side. We propose a model modified from the work of Ye and LeVan[9] for the dehydration of an air stream at various flow rates and feed relative humidities.

5.2 Experiments

The experimental apparatus used to characterize the drying performance of a Nafion® shell and tube membrane module with a vacuum purge is shown in Figure 5.1. We used a membrane purchased from PermaPure, Inc. (PD-100T-48MSS) with 100 tubes housed in a stainless steel shell. The dimensions of the membrane are shown in Table 5.1.

To deliver a feed stream of known humidity to the tube inlet of the membrane, compressed laboratory air flowed through a pressure swing adsorption (PSA) dehydration system and then passed through a manifold with 4 water filled bubblers immersed in a temperature bath consisting of a 50% ethylene glycol and water mixture. The gas then flowed through a copper tube approximately 4 m long to reach room temperature before being fed to the membrane module. The required relative humidities were achieved by regulating the temperature of the bath. A mass flow controller (MKS) and 4 channel readout were used to regulate the flow of the feed stream. Two relative humidity sensors (Vaisala) were used near the tube inlet and outlet to measure the temperature and relative humidity of the process stream. Three 1000 torr and one 100 torr pressure transducers (MKS) were used to measure the pressure on the tube and shell sides. A turbo pump with a diaphragm priming pump was used

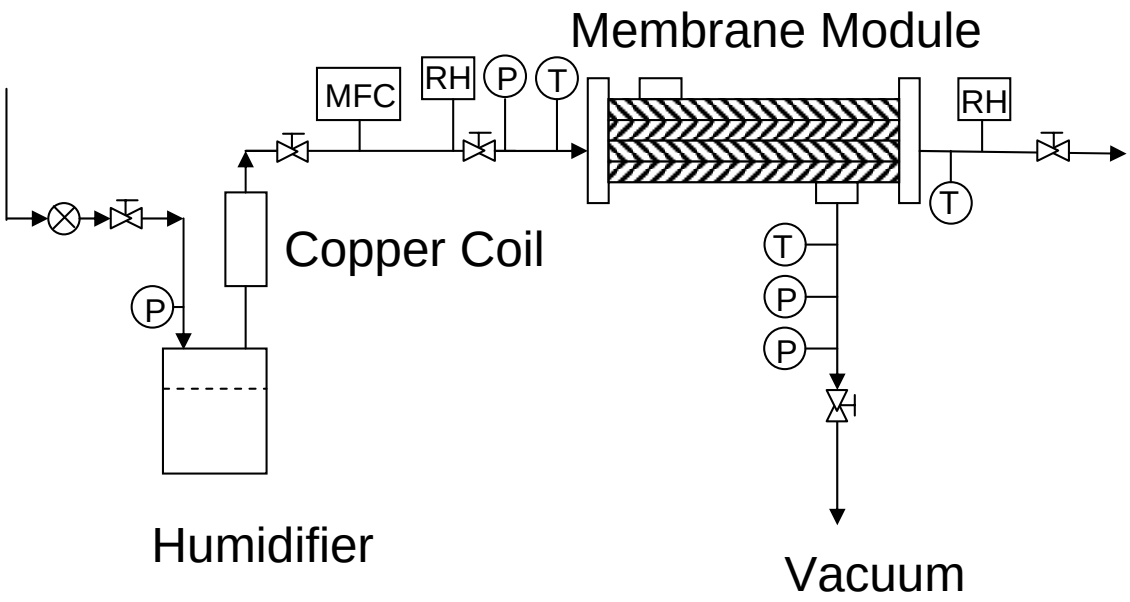

Figure 5.1: Diagram of the experimental apparatus for removing water vapor using a Nafion® with a vacuum on the shell side which uses two relative humidity sensors (RH), three thermocouples (T), a mass flow controller (MFC), and four pressure transducers (P), three of which have a maximum operating range of 1000 torr and one 100 torr.

to provide the vacuum (in a microtorr range) on the shell side.

Initially, the membrane was dried by exposure to a microtorr vacuum overnight to ensure that the level of hydration correctly corresponded to the experimental relative humidity. A gas stream was then fed to the tube side of the vacuum at 5 slpm for a particular relative humidity until no measurable change in pressure on the shell side occurred within 10 minutes, at which time measurements were made of the relative humidity and temperature of the tube-side fluid stream at the tube inlet and outlet and the pressure at the tube inlet along with the temperature and pressure of the fluid exiting the shell during an hour-long interval. At the end of the interval, the feed stream flow rate was increased and the experiment was repeated for tube-side flow rates of 8 and 10 slpm. When relative humidity, temperature, and pressure data had been collected for all three flow rates, the membrane was exposed to a microtorr vacuum overnight and the procedure was repeated the next day for a different relative humidity. All experiments were performed at room temperature ($\sim$24°C).

5.3 Theory

We examine the transport of water from inside a shell and tube membrane module with a vacuum on the shell side as an alternative to a purge gas. A representative schematic of the membrane is shown in Figure 5.2. A sample gas intended for dehydration is fed to the tube side at a specified total mass flow rate, ω_t, and mass fraction of water, x. As the sample gas flows down the length of the membrane, water permeates from the tube side through the membrane to the shell side. In our model, we assume that the permeation rates of nitrogen and oxygen are insignificant compared with that of water based on the values measured by Gode et al.[3] We also measured permeation rates of oxygen and nitrogen under dry conditions through the membrane used in the experiments and found them to be very low 1.04×10^{-10} and 2.2×10^{-11} mol/ m s kPa, respectively, for a pressure gradient of 140 kPa. We also as-

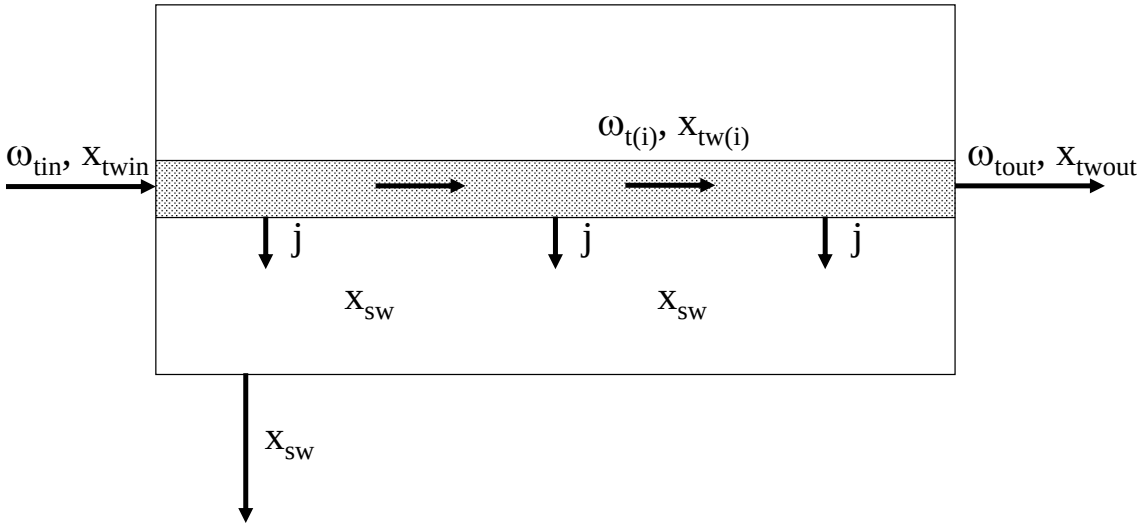

Figure 5.2: Representative diagram of shell and tube membrane with a vacuum applied to the shell side.

sume that axial diffusion is negligible compared to the bulk flow, gases may be treated as ideal, the membrane apparatus is isothermal, and end effects may be neglected.

We write a tube side material balance in which the rate of water lost inside the tubes is set equal to the surface integral of the rate at which water is transported to the membrane interface given by

$$\omega_{tin}x_{twin} - \omega_{tout}x_{twout} = -\int_A j_1 dA_1 \tag{5.1}$$

where j_1 is the mass flux of water to the membrane interface.

We convert equation 5.1 from a mass to a molar perspective to yield

$$F_t^{air}\left(\left.\frac{y_{tw}}{1-y_{tw}}\right|_{z=L} - \left.\frac{y_{tw}}{1-y_{tw}}\right|_{z=0}\right) = -\int_A J_1 dA_1 \tag{5.2}$$

where F_t^{air} is the total molar flow rate of dry air which is related to the total molar flow rate by

$$F_t^{air} = \left(1 - y_{tw(i)}\right) F_{t(i)}^{tot} \tag{5.3}$$

which we assume to remain constant through the length of the membrane.

We then introduce a two resistance model to account for the transport of water from the tube-side fluid to the tube-side membrane interface and for the transport of water through the membrane itself. These are given by

$$J_1 = -k_t\left(c_{tmt}y_{mtw} - c_{tt}y_{tw}\right) \tag{5.4}$$

$$J_2 = -\frac{1}{l_m}\int_{P_{mtw}}^{P_{sw}} D\frac{dc_w}{dP_w}dP_w \tag{5.5}$$

where J_1 and J_2 are the local mass transfer rates , y_{sw} and y_{tw} are the mole fractions of water in the shell and tube, and P_{mtw} and P_{sw} are the partial pressures of water at the tube-side membrane interface and in the shell, respectively. The convective mass transfer coefficient of water for the tube side interfacial resistance, k_t, is determined from correlations Shah and London[5] developed for laminar flow in tubes.

Ye and LeVan[9] provide a relationship for the diffusion coefficient of a single tube module in the form

$$D_{YL} = \frac{Pe_m}{V_{std}\,(dc_w/dP_w)} \tag{5.6}$$

where V_{std} is the molar volume of gas at a standard state, and Pe_m is the permeability of water through the membrane for a single tube as a function of the partial pressure of water given by

$$Pe_m = \frac{2.8 \times 10^{-6} P_w^{3/2}}{P_{atm}} \tag{5.7}$$

The diffusion coefficient in equation 5.6, D_{YL}, is inversely proportional to the slope of the water adsorption curve, dc_w/dP_w, determined from the partial derivative of the ratio of the moles of water to the sulfonic acid sites, λ, with respect to the partial pressure of water

$$\frac{M_{Naf}}{\rho_{Naf}} \frac{dc_w}{dP_w} = \frac{d\lambda}{dP_w} \tag{5.8}$$

and yields

$$\frac{dc_w}{dP_w} = \frac{\rho_{Naf}}{M_{Naf}} \left(\frac{17.81}{P_{sat}} - \frac{79.2}{P_{sat}^2} P_w + \frac{108}{P_{sat}^3} P_w^2 \right) \tag{5.9}$$

where ρ_{Naf} and M_{Naf} are the density and molecular weight of Nafion®, respectively, and P_{sat} is the saturated vapor pressure for water.

In their second paper, Ye and LeVan[10] discuss the impact that the membrane thickness has on the permeability of the membrane concluding that a simple proportionality relationship does not adequately consider interfacial skin effects. Instead, they develop a permeability for a multi-tube membrane module determined empirically as

$$Pe_m = \frac{1.1 \times 10^{-6} P_w^{3/2}}{P_{atm}} \tag{5.10}$$

Substituting equation 5.10 into equation 5.6 yields

$$D_{YL} = \frac{1.1 \times 10^{-6} P_w^{3/2}}{P_{atm} V_{std}\,(\partial c_w/\partial P_w)} \tag{5.11}$$

D_{YL} in equation 5.11 is evaluated for partial pressures ranging from 0 to 3 kPa and shown in Figure 5.3.

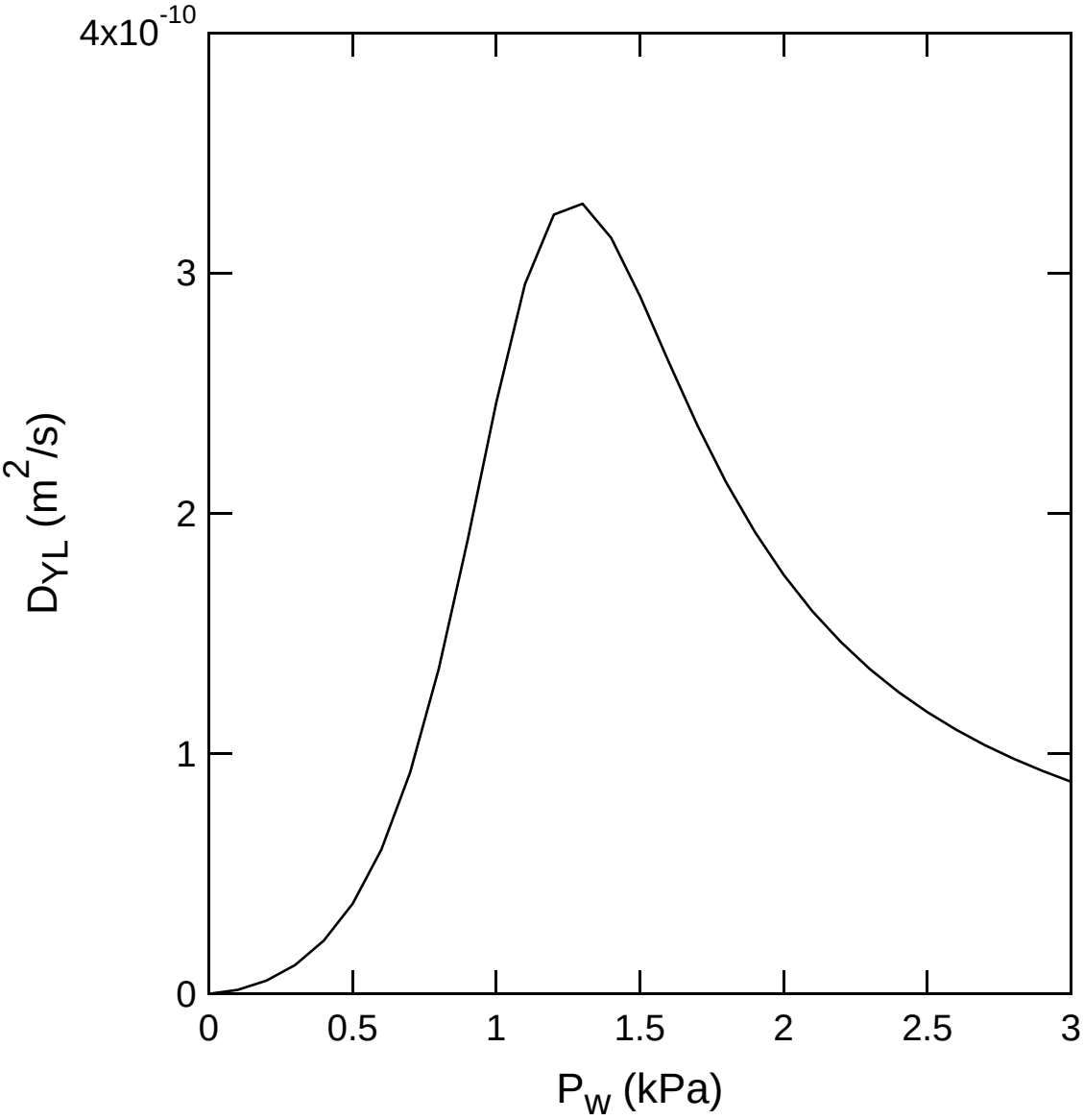

Figure 5.3: Diffusion coefficient for water in Nafion® calculated at various partial pressures at a temperature of 298K.

Once steady state is reached, the rates at which mass is transfered to the membrane interface and is transported through the membrane satisfy

$$J_1 dA_1 = J_2 dA_2 \tag{5.12}$$

where dA_1 is the differential area based on the outside diameter of the tube and dA_2 is the logarithmic mean of the cross-sectional areas of the tube and shell.

We recognize that the relationship used in our model to calculate the diffusion coefficient of water in the membrane was determined for a shell and tube membrane module operating with a purge gas on the shell side. Also, data used by Ye and LeVan[9] in establishing the diffusion coefficient shown in equation 5.11 considered relative humidity values in the tube and shell ranging from 6.5% to 94%. To account for any differences in water transport through the membrane between normal operation employing a purge stream and vacuum operation we introduce a membrane diffusion efficiency, η, of the form

$$\eta D_{YL} = D \tag{5.13}$$

where D_{YL} is the diffusion coefficient determined from the relationship Ye and LeVan[9] developed which we modify for use in our system as described by equation 5.11. Substituting equation 5.13 into 5.5 and integrating yields

$$J_2 = -\eta \frac{1.1 \times 10^{-6}}{P_{atm} V_{std} \times 10^4 \, l_m} \frac{2}{5} \left(P_{sw}^{5/2} - P_{mtw}^{5/2} \right) \tag{5.14}$$

5.4 Results

We examine the dehydration performance of a multi-tube Nafion® membrane module via a numerical solution of the coupled tube-side material balance and rate equations. We model the membrane in Figure 5.2 as a set of differential segments in series and solve the material balances for each segment simultaneously using a nonlinear equation solver that implements a modified Powell method.[2]

The estimated errors associated with measuring the water concentration for the tube and shell side outlets were determined by taking the average of the difference

between the measured data point and the time averaged value for the entire length of the experiment. The errors associated with the uncertainties in measurements were less than 2% and 3% for pressure and relative humidity, respectively. The propagation of uncertainties in measurements in calculated quantities was then determined using[7]

$$\delta q = \sqrt{\left(\frac{\partial q}{\partial x}\delta x\right)^2 + \cdots + \left(\frac{\partial q}{\partial z}\delta z\right)^2} \tag{5.15}$$

where q is a calculated value, δq is the error in a calculated value, and δx and δz are the errors associated with the measured values. Using this method, all cumulative errors associated with the calculation of water concentrations in the tube and shell sides were determined to be $\pm 5\%$.

Concentration profiles along the length of the membrane for a feed relative humidity of 20% are shown in Figures 5.4 through 5.6 for varying tube-side flow rates of 5, 8, and 10 slpm, respectively. The tube and shell side concentrations are represented by solid curves and the tube-side interfacial concentrations are described by dashed curves. Here it can be seen that the tube side concentration decreases in quantity as the gas stream flows down the length of the membrane, while the shell-side concentration remains constant since we assume that the partial pressure of water on the shell side is uniform and equal to the outlet pressure. Also, the tube-side interfacial resistance does not appear to have a significant impact on the transport of water as much as the resistance through the membrane itself, shown in Figure 5.7, indicating that the diffusion of water through the membrane is the rate limiting factor. It is also important to note that the slope of the concentration profile on the tube side, i.e., dc_{tw}/dz is the steepest near the inlet for a tube-side flow rate of 5 slpm.

The concentration profiles along the length of the membrane for feed relative humidities of 50% and 70% are shown in Figures 5.8 through 5.10 and Figures 5.11 through 5.13, respectively. As seen in the previous figures, water transport is affected primarily by diffusional resistances of water through the membrane for all feed relative

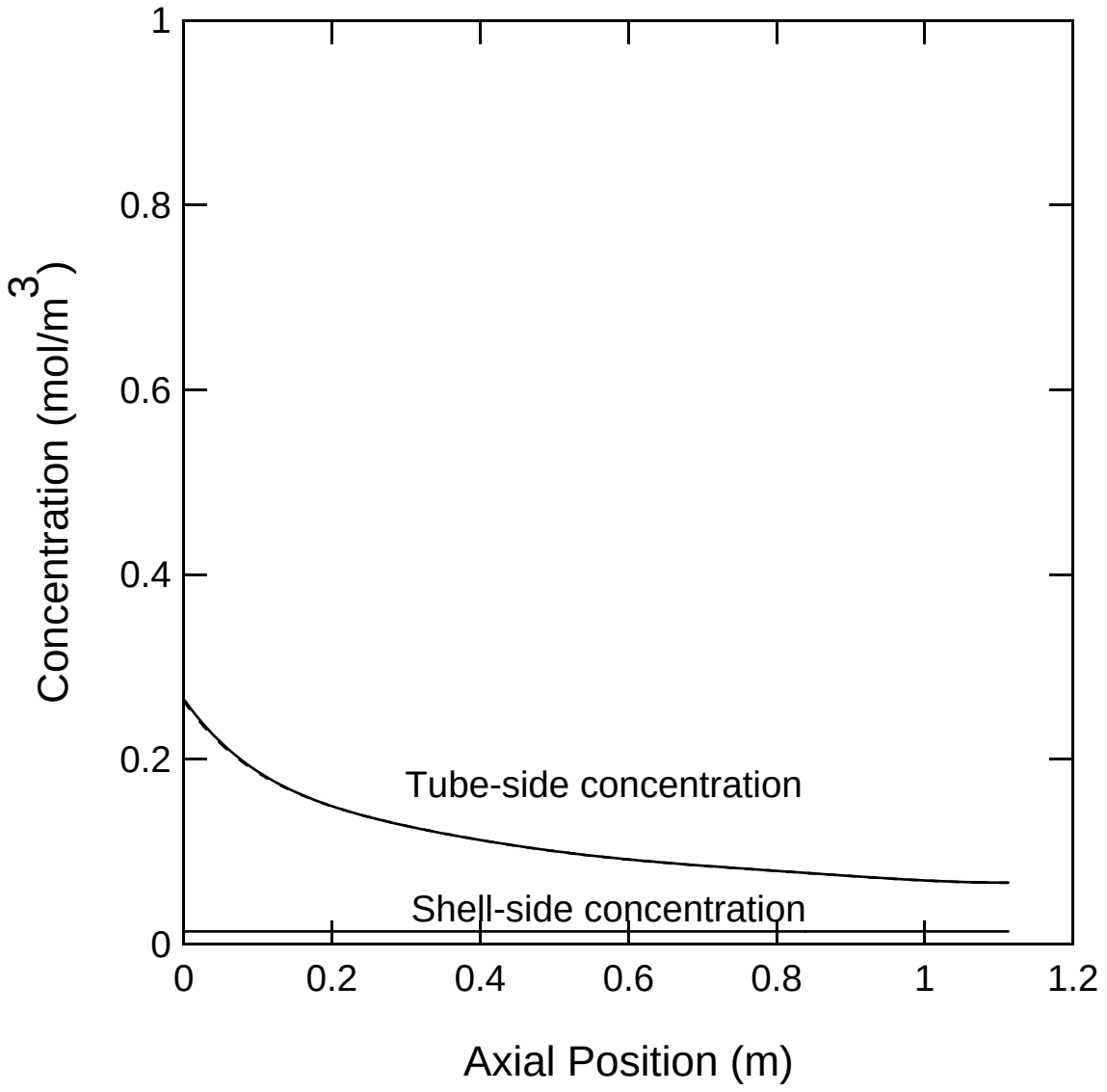

Figure 5.4: Concentration profile for the membrane with a feed relative humidity of 20% and tube-side flow rate of 5 slpm.

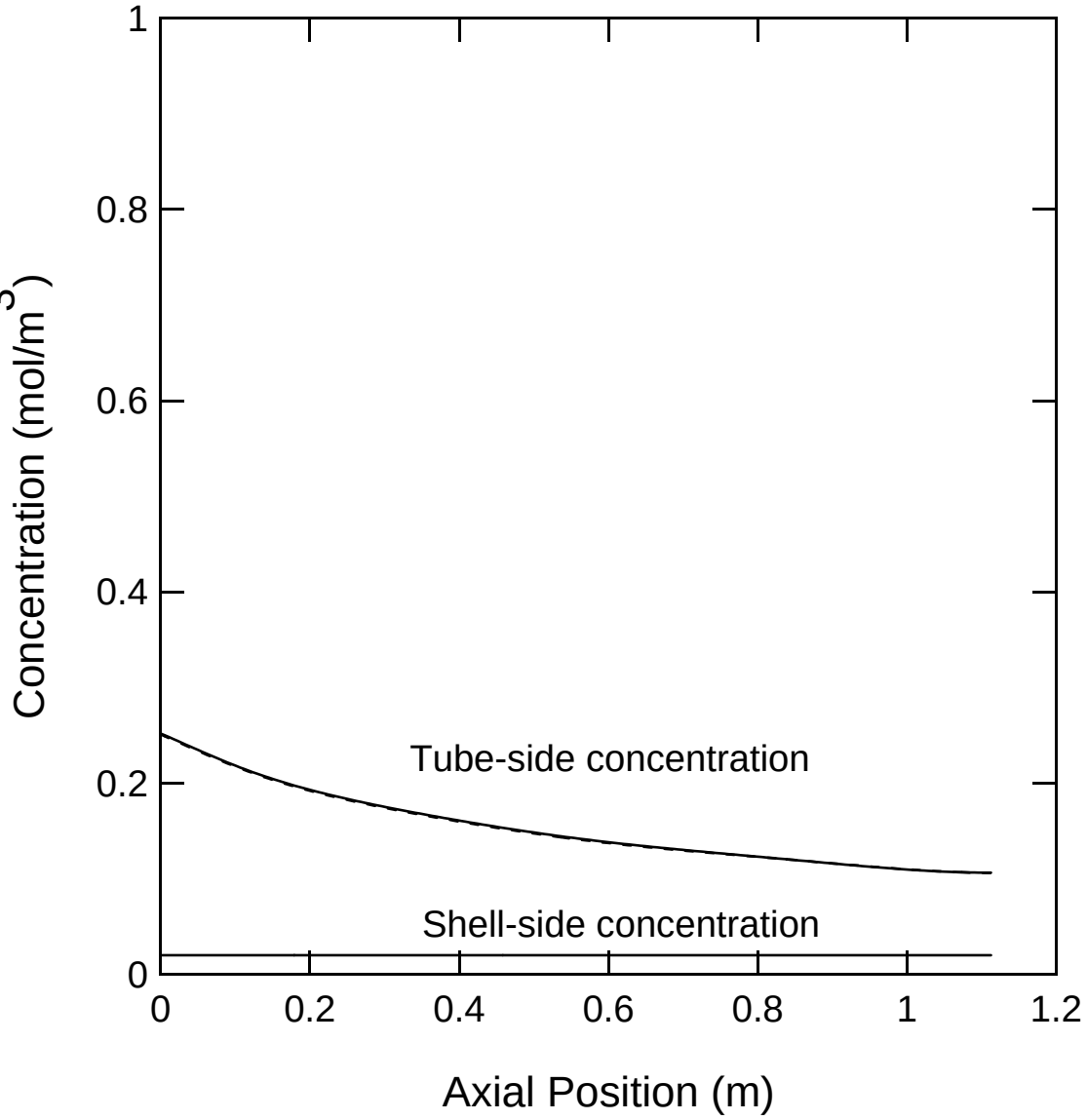

Figure 5.5: Concentration profile for the membrane with a feed relative humidity of 20% and tube-side flow rate of 8 slpm.

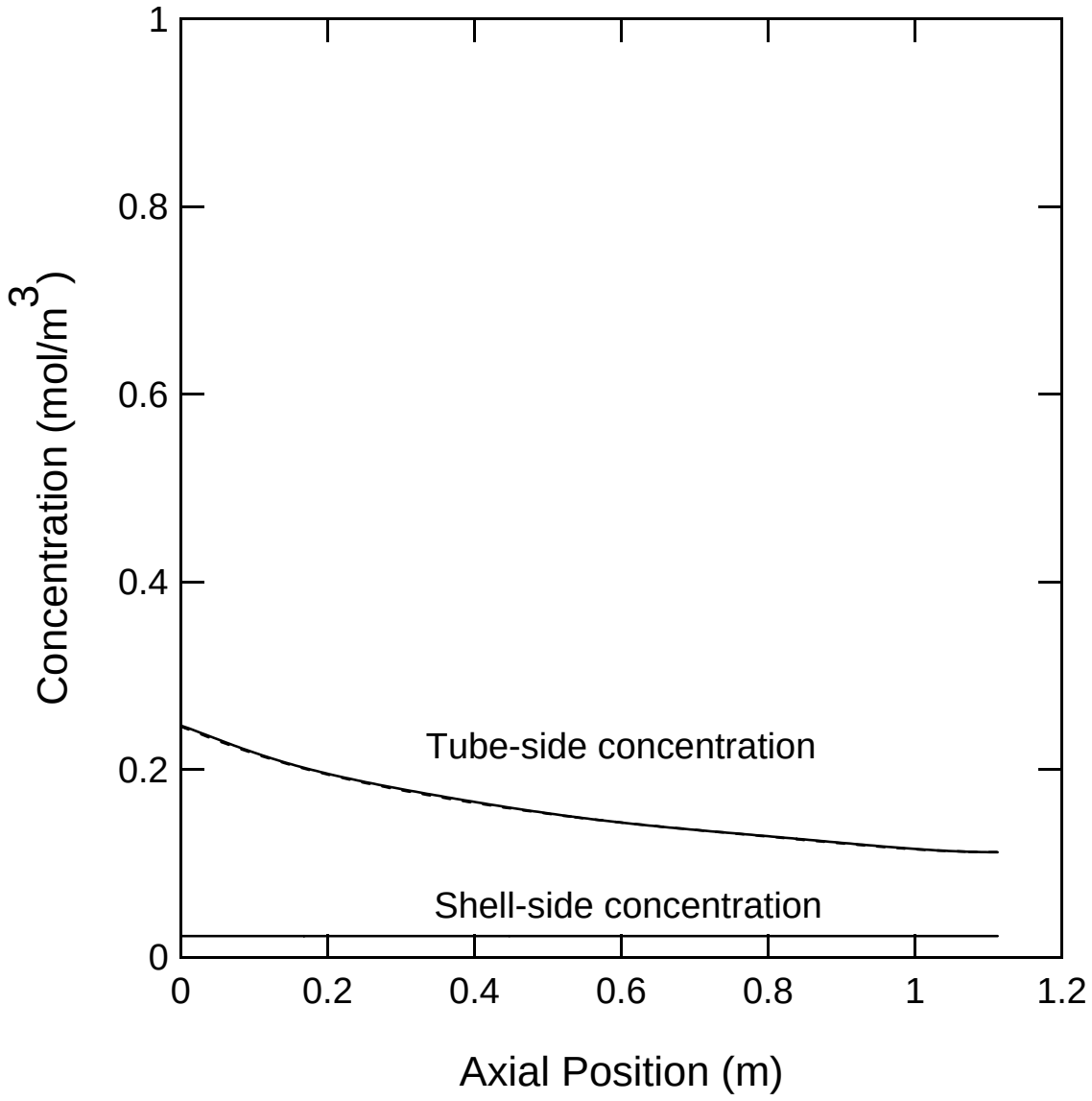

Figure 5.6: Concentration profile for the membrane with a feed relative humidity of 20% and tube-side flow rate of 10 slpm.

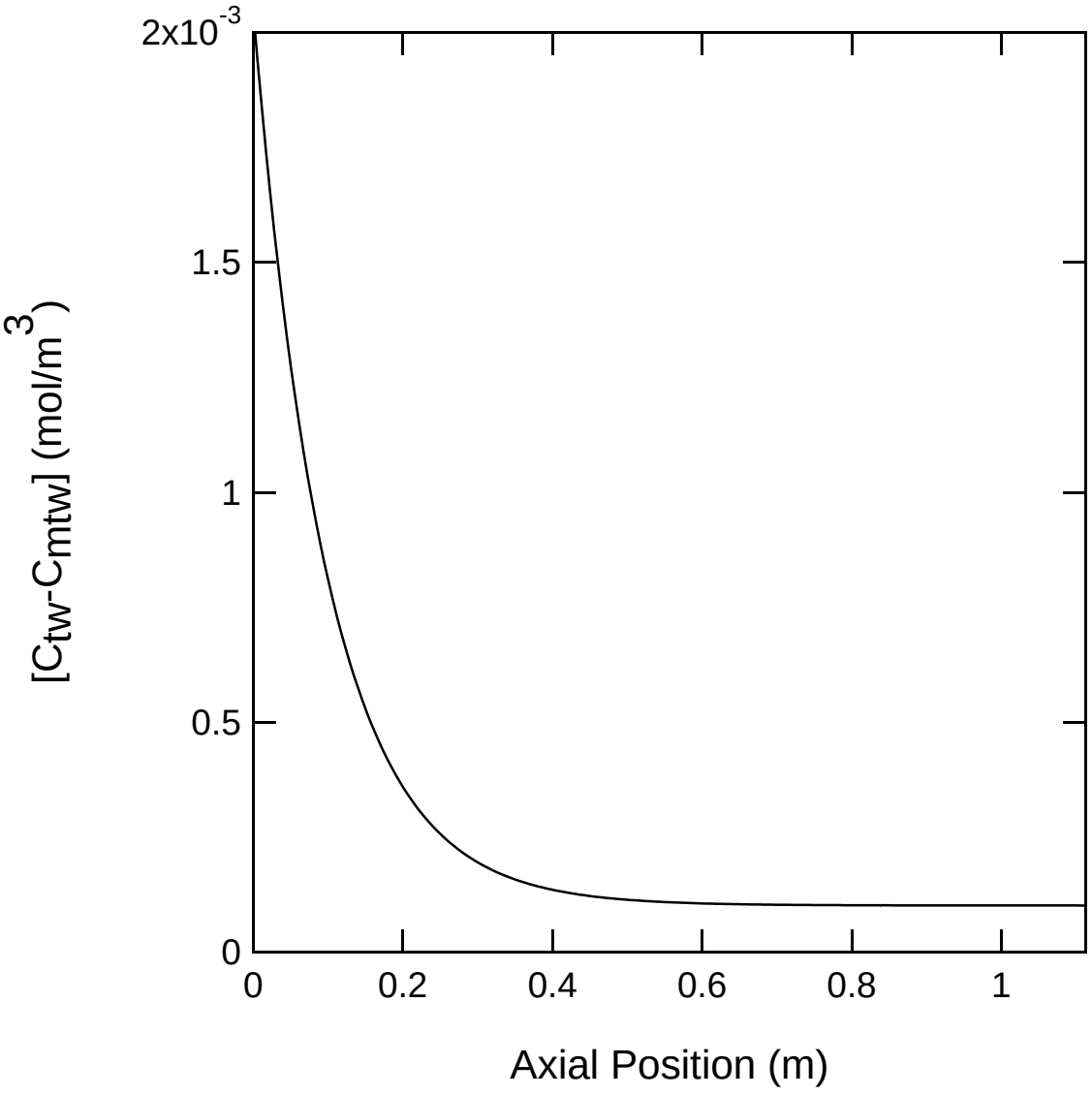

Figure 5.7: Difference between the calculated tube side concentration and the tube side interfacial concentration for a tube-side flow rate of 5 slpm, and feed relative humidity of 20%.

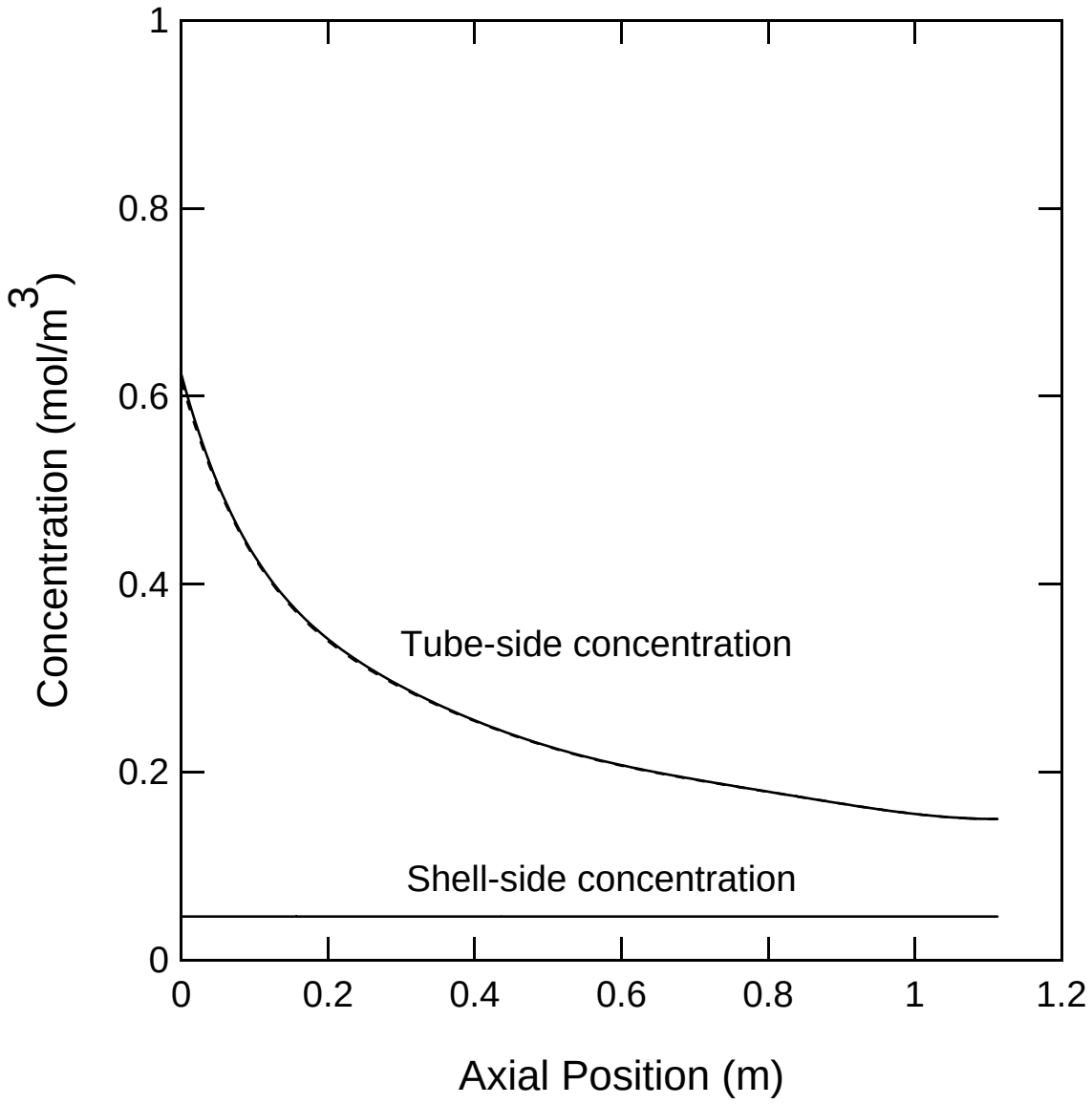

Figure 5.8: Concentration profile for the membrane with a feed relative humidity of 50% and tube-side flow rate of 5 slpm.

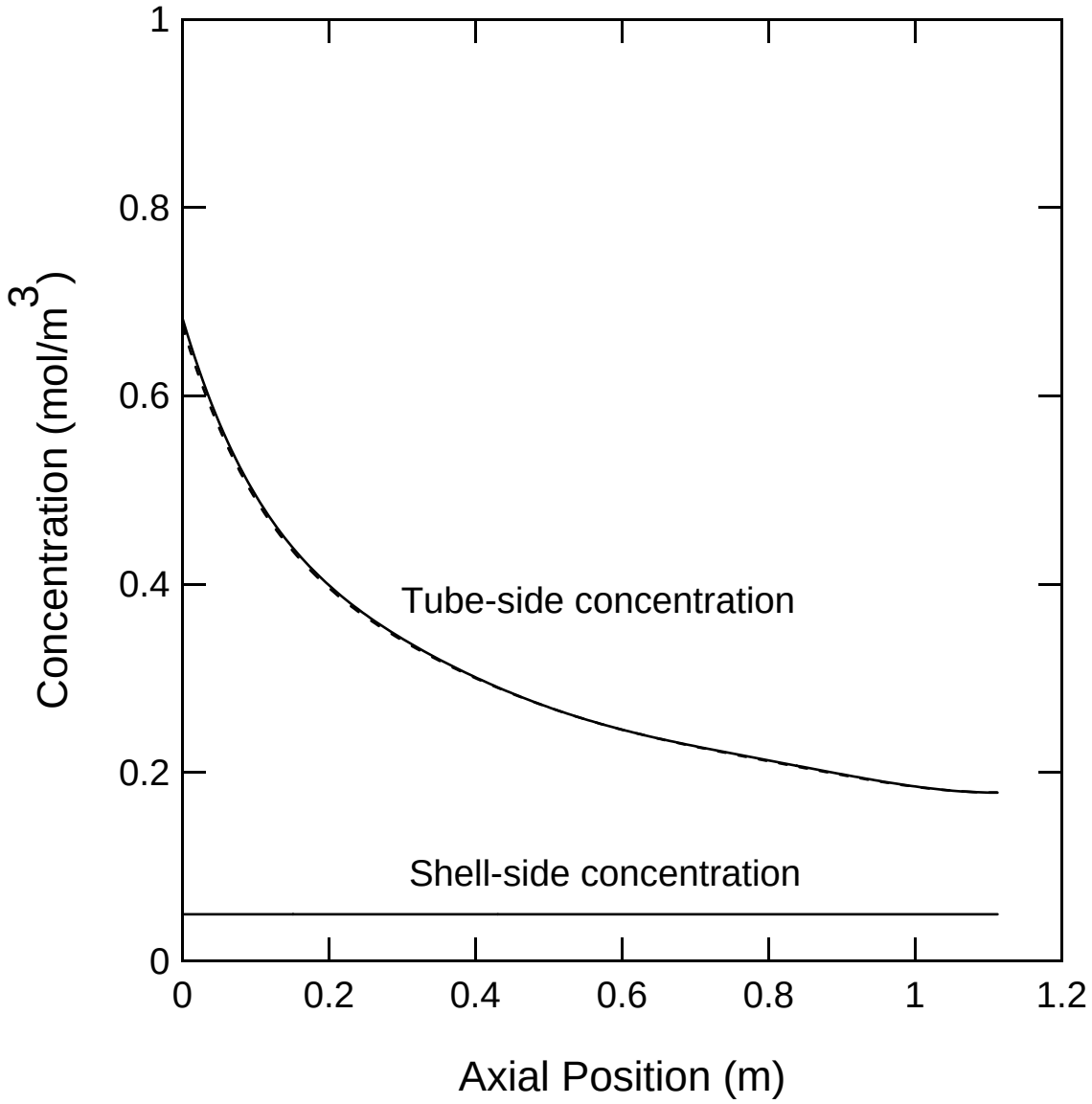

Figure 5.9: Concentration profile for the membrane with a feed relative humidity of 50% and tube-side flow rate of 8 slpm.

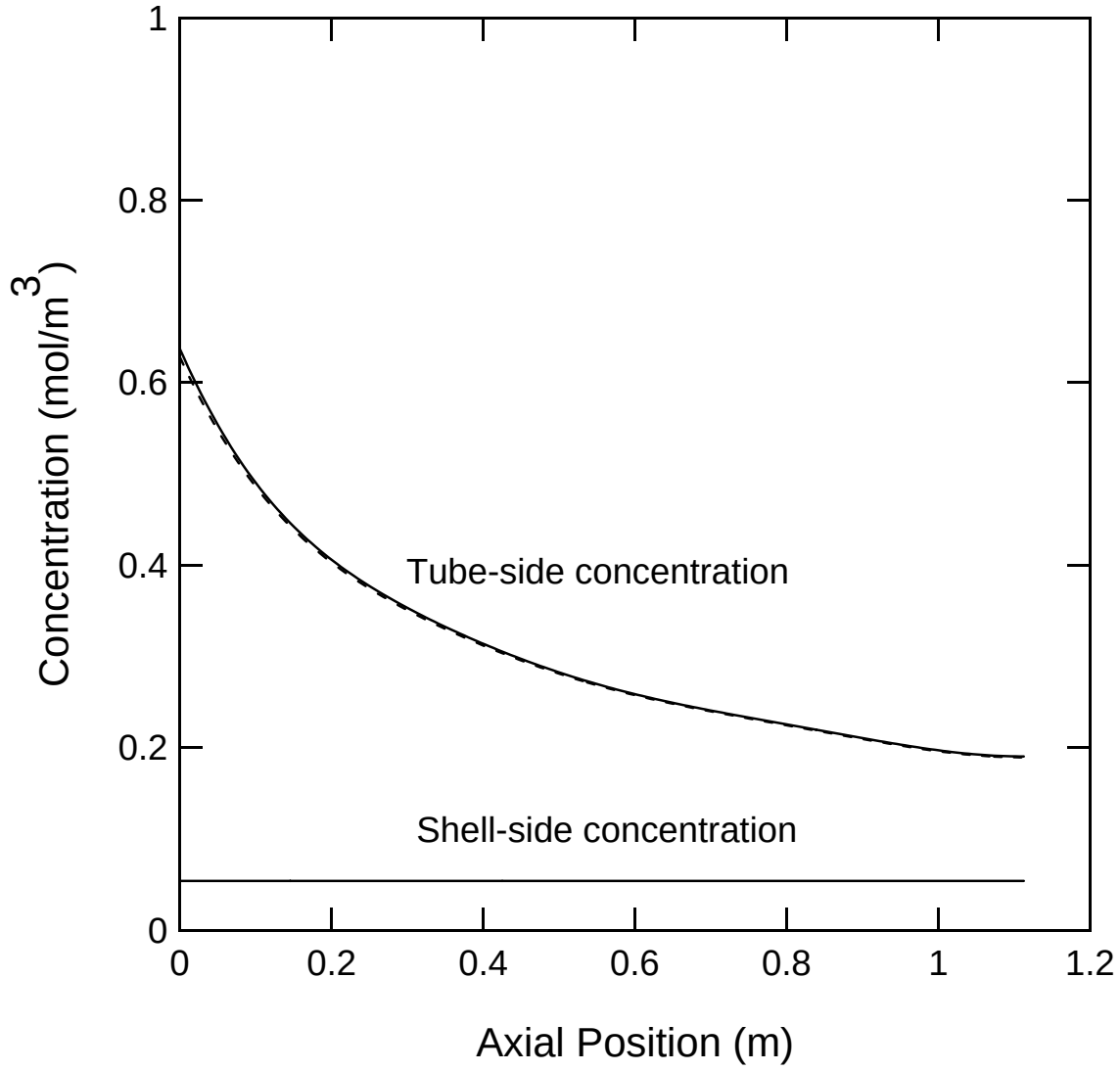

Figure 5.10: Concentration profile for the membrane with a feed relative humidity of 50% and tube-side flow rate of 10 slpm.

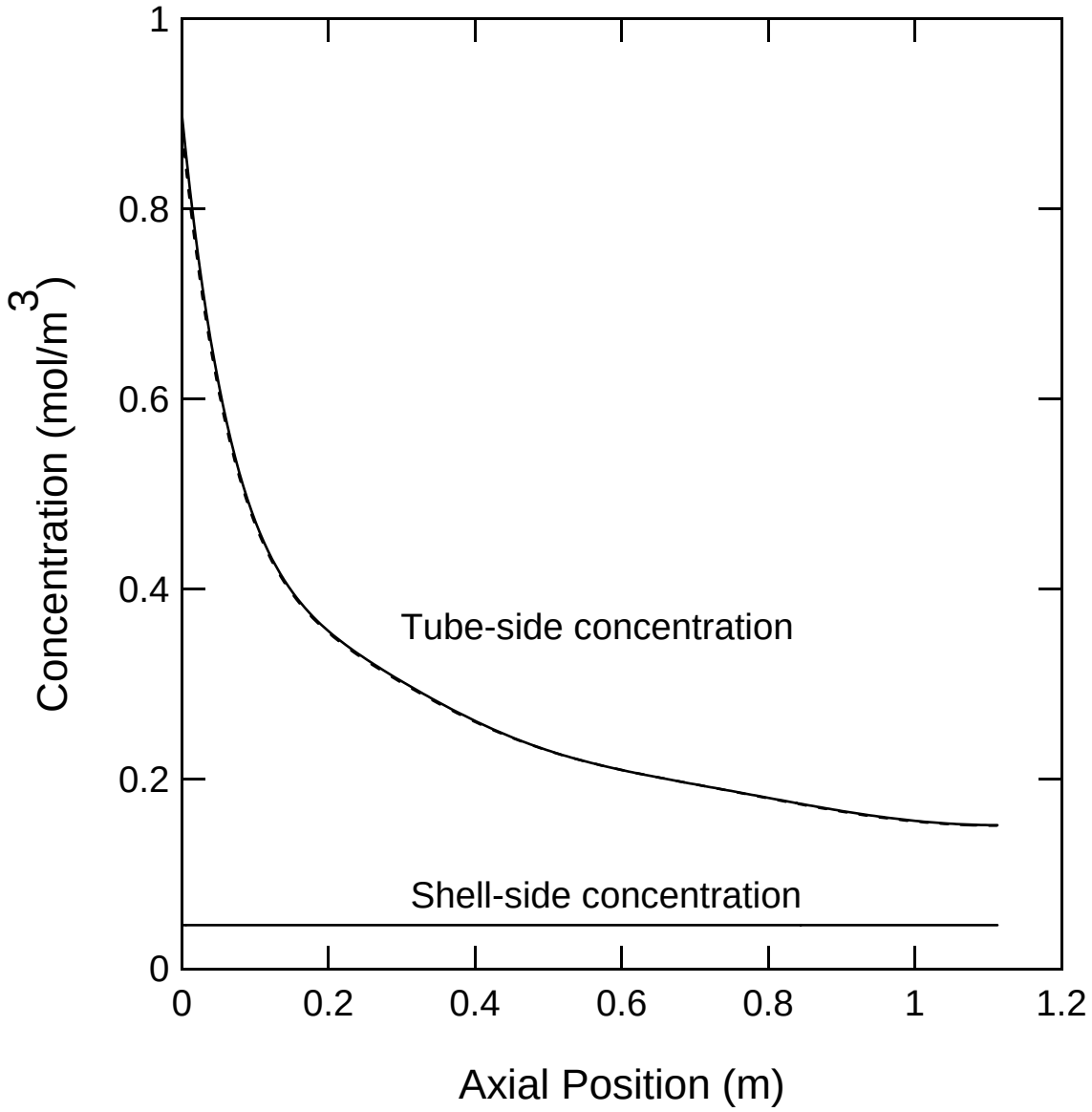

Figure 5.11: Concentration profile for the membrane with a feed relative humidity of 70% and tube-side flow rate of 5 slpm.

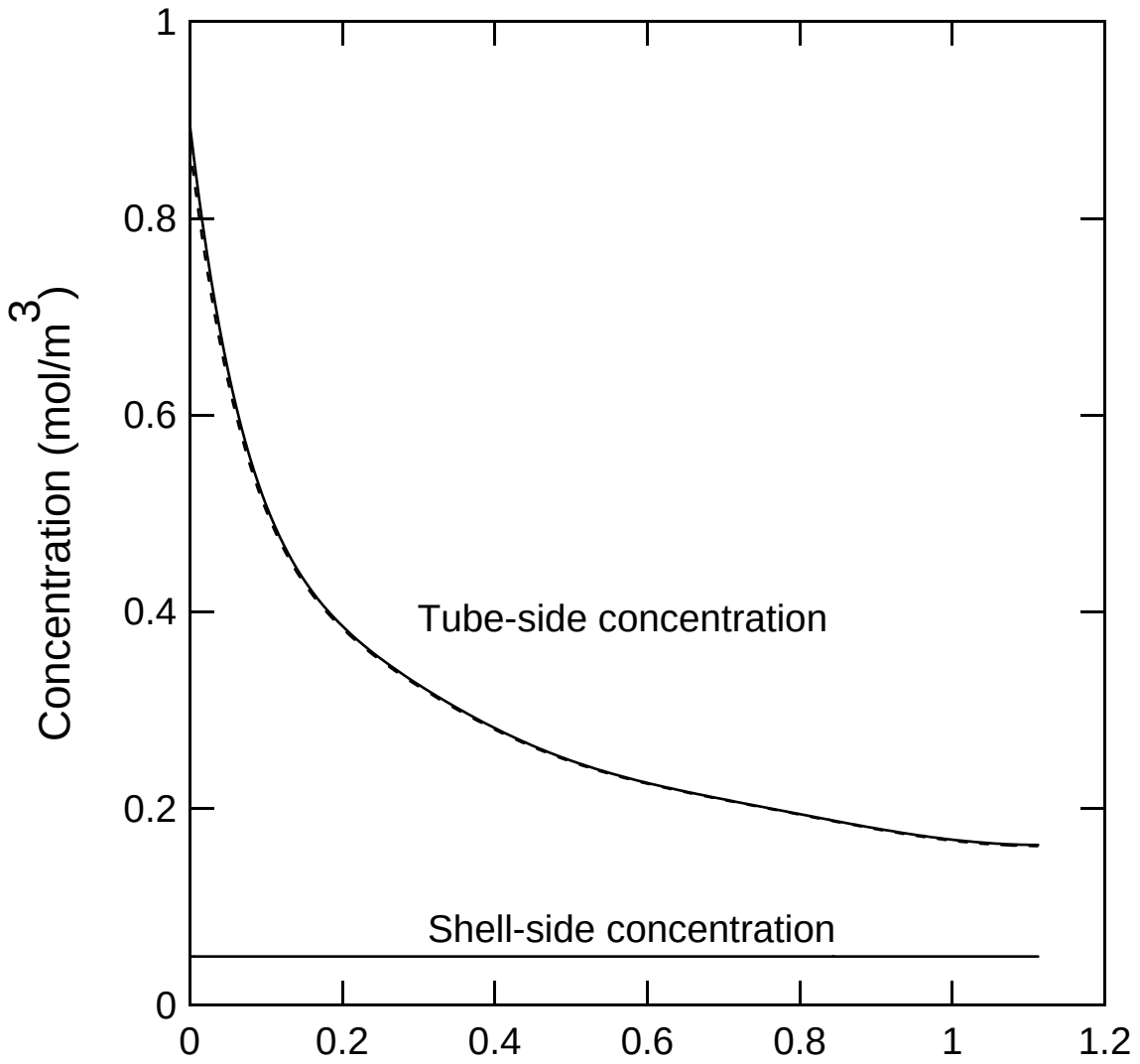

Figure 5.12: Concentration profile for the membrane with a feed relative humidity of 70% and tube-side flow rate of 8 slpm.

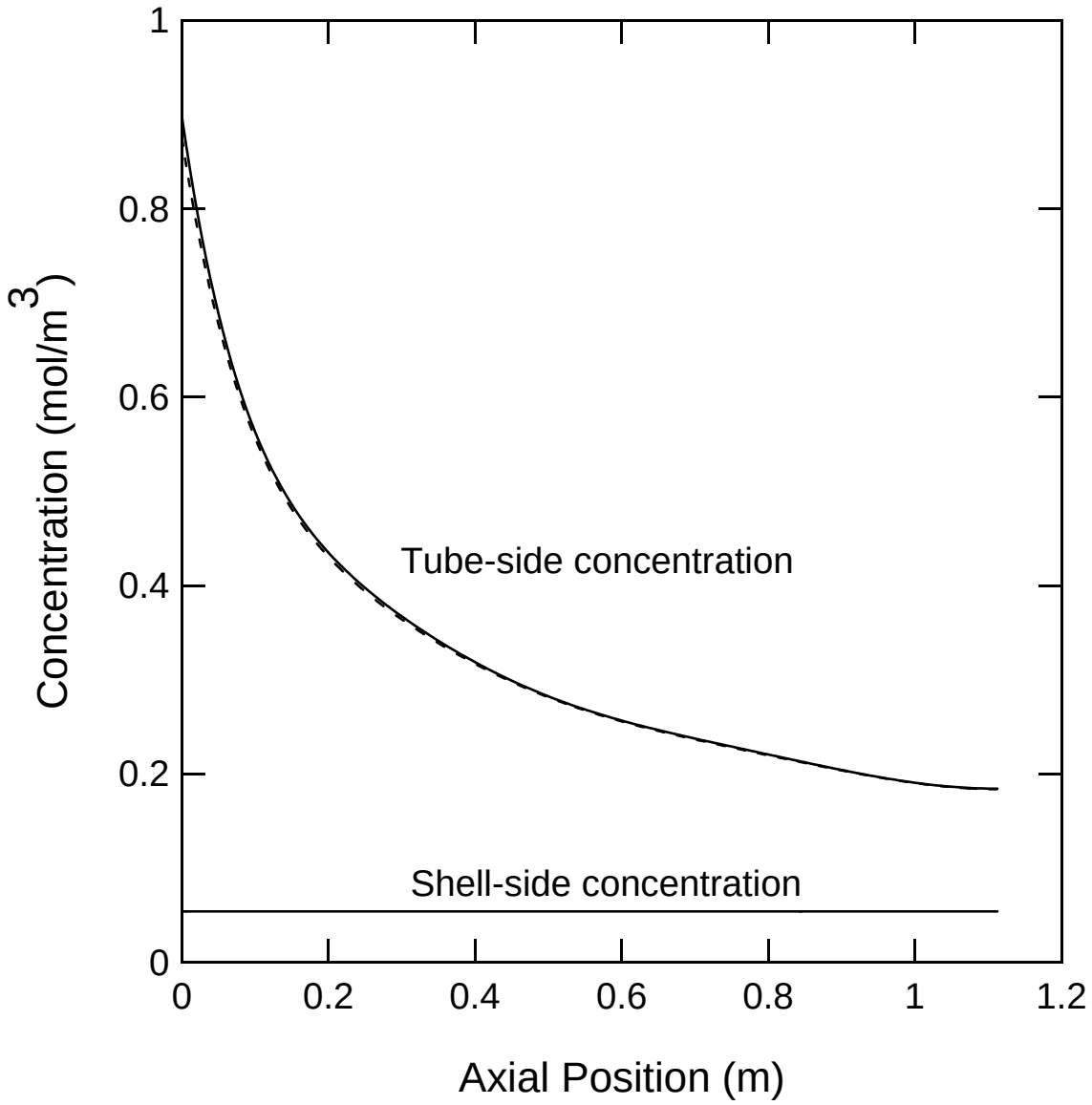

Figure 5.13: Concentration profile for the membrane with a feed relative humidity of 70% and tube-side flow rate of 10 slpm.

Table 5.2: Diffusional efficiencies, η, determined for varying tube-side flow rates and relative humidities.

%RH	5 slpm	8 slpm	10 slpm
20%	58.9%	38.3%	42.0%
50%	17.6%	21.3%	23.4%
70%	18.1%	26.1%	26.7%

humidities considered, and the slope of the concentration profile on the tube side is sharpest at the inlet for a tube-side flow rate of 5 slpm.

The relationship to determine a tube side diffusion coefficient developed by Ye and LeVan[9] incorporates the adsorption isotherm developed by Springer et al.[6] and therefore requires λ to be 4 or greater in order to be valid. However, the relative humidity on the shell-side ranges from 1-5% which corresponds to a value for λ less than 4. To account for this discrepancy, our model includes a diffusional efficiency as described in equation 5.14, which we evaluated for the range of flow rates and relative humidities studied and are shown in Table 5.2. A minima occurs for the diffusional efficiency for a relative humidity of 50% since the relationship for the diffusion coefficient developed by Ye and LeVan[9] has a sharp peak for a partial pressure of water around 1.5 kPa as shown in Figure 5.3, corresponding to a relative humidity of 50%.

The values for the flux of water through the membrane as predicted using the diffusion coefficient in equation 5.11 and the actual value corresponding to our experiments are evaluated for all flow rates and feed relative humidities considered and plotted against the axial position in Figures 5.14 through 5.16. It is evident that as the relative humidity in the feed is increased, the difference between the diffusion coefficients increases significantly further indicating that the relationship between the diffusion coefficient and the partial pressure of water developed by Ye and LeVan[9] for a single-tube membrane module and modified for a multi-tube module, as by Ye and LeVan,[10] does not accurately describe the phenomena occurring within the

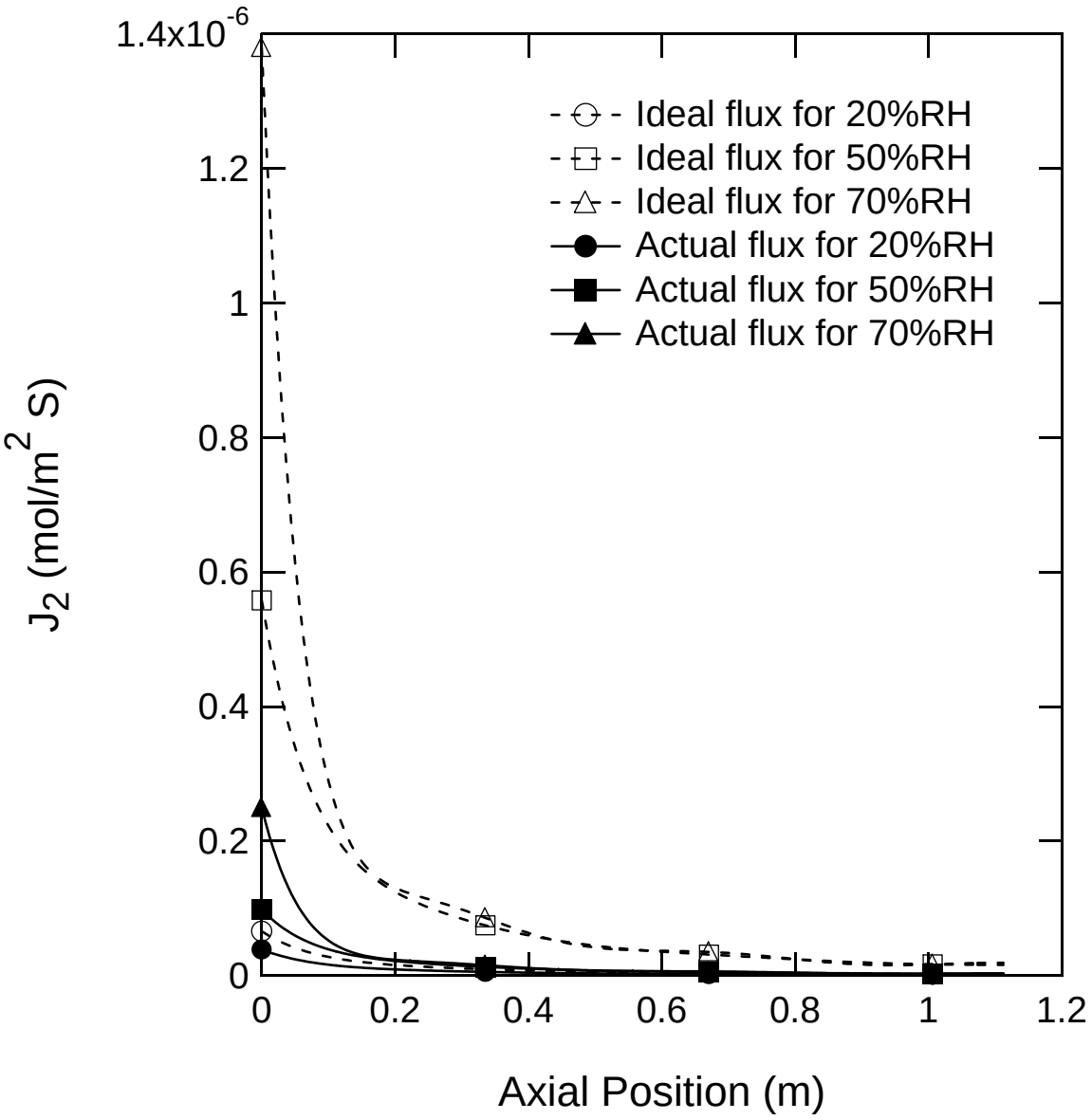

Figure 5.14: Flux of water through the membrane for a tube-side flow rate of 5 slpm. Symbols are used to delineate curves and do not represent measured data.

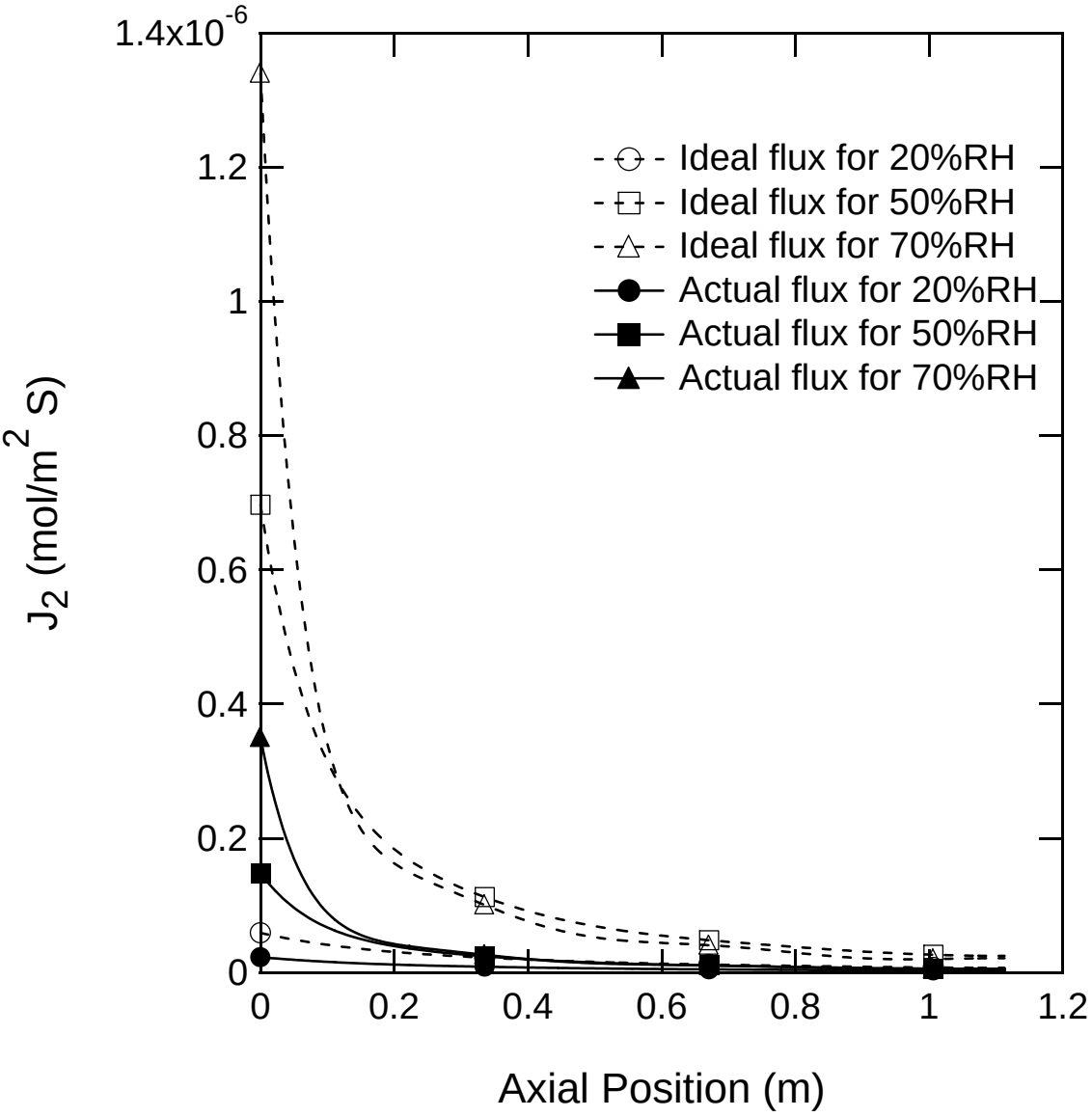

Figure 5.15: Flux of water through the membrane for a tube-side flow rate of 8 slpm. Symbols are used to delineate curves and do not represent measured data.

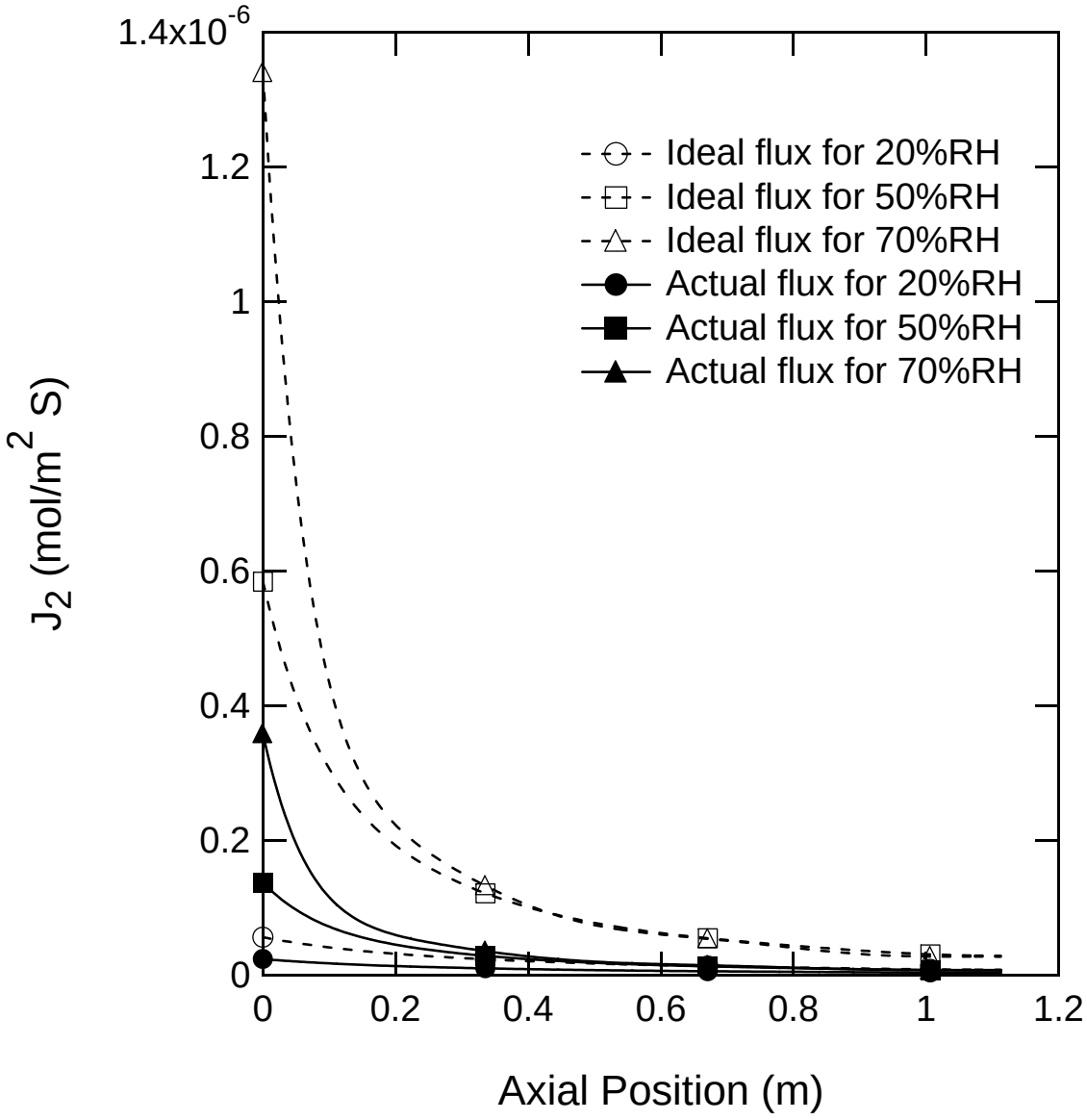

Figure 5.16: Flux of water through the membrane for a tube-side flow rate of 10 slpm. Symbols are used to delineate curves and do not represent measured data.

membrane. This discrepancy is probably due to the ratio of the water molecules to the sulfonic acid sites, λ, being significantly reduced through the thickness of the membrane by the vacuum on the shell-side effectively drying it out and shutting down water transport. Relative humidities in the shell for the experiments reported here range from 1.1% to 5.4%. These are below the values of 6.5% to 94% mentioned earlier that were used by Ye and LeVan[9] to establish their diffusion coefficient.

5.5 Conclusions

An experimental and modeling study has been performed to examine the viability of using a multi-tube Nafion® shell and tube membrane module with vacuum applied on the shell side in lieu of a purge gas to dehydrate a gas stream flowing on the tube side. In experiments, the membrane remained intact and showed no degradation in integrity over the course of the study. A mathematical model was developed and solved that accounted for an interfacial resistance and a diffusional resistance through the membrane. Several cases were investigated in which the feed flow rate and relative humidity varied from 5 to 10 slpm and 20% to 70%, respectively.

We conclude that a Nafion® membrane module with a shell-side vacuum can be used for removal of water from a feed stream. We also determined that although water was being transported from the tube to the shell side, the flux of water through the membrane was lower than predicted by the relationship previously developed by Ye and LeVan[9] due to decreased hydration levels inside the membrane. We also determined that mass transfer resistances inside the fluid phase have no significant impact on the rate of water transport.

Notation:

A	measured surface area, m^2
c_t	total concentration, mol/m^3
D	diffusion coefficient through the membrane, m^2/s
D_{YL}	diffusion coefficient developed by Ye and LeVan,[9] cm^2/s
dA_1, dA_2, dA_3	differential resistance areas, m^2
F^{tot}	total molar flow rate, mol/s
F^{air}	molar flow rate of dry air, mol/s
j_1, j_2, j_3	local mass fluxes, kg/m^2 s
J_1, J_2, J_3	local molar fluxes, mol/m^2 s
k	convective mass transfer coefficient, mol/m^2 s
l_m	thickness of the membrane, m
M	molecular weight, kg/mol
N_t	number of tubes in the membrane
P_{atm}	atmospheric pressure, kPa
P_{sat}	saturated vapor pressure of water, kPa
P_w	partial pressure of water, kPa
Pe_m	Permeability of the membrane, m^3_{std}/m kPa s
V_{std}	molar volume of an ideal gas at stp, m^3/mol
x	mass fraction
y	mole fraction
z	axial dimension

Greek Letters

η	membrane diffusion efficiency
ω	mass flow rate, Kg/s
ρ	density, Kg/m^3

Subscripts

mt	tube-side interface
Naf	property of Nafion®
ref	reference state
s	shell side
t	tube side
w	water

References

[1] R.B. Bird, W.E. Stewart, E.N. Lightfoot, Transport Phenomena, 2nd ed.; John Wiley and Sons Inc: New York, 2002.

[2] B.S. Garbow, K.E. Hillstrom, J. Jorge, Minpack Project, Argonne National Laboratory, March 1980.

[3] P. Gode, G. Lindbergh, G. Sundholm, In-Situ measurements of gas permeability in fuel cell membranes using a cylindrical microelectrode, Journal of Electroanalytical Chemistry, 518 (2002) 115-122.

[4] D.R. Morris, X.D. Sun, Water-sorption and transport properties of Nafion 117 H, Journal of Applied Polymer Science, 50 (1993) 1445.

[5] R.K. Shah, A.L. London, Supplement 1 to advances in heat transfer; Academic Press: New York, 1978.

[6] T.E. Springer, T.A. Zawodzinski, S. Gottesfeld, Polymer electrolyte fuel cell model, Journal of the Electrochemical Society, 138 (1991) 2334-2342.

[7] John R. Taylor, An Introduction to Error Analysis, 2nd ed.; Universal Science Books: Sausaltom, Ca, 1982.

[8] A.Z. Weber, J. Newman, Transport in polymer-electrolyte membranes I. Physical model, Journal of the Electrochemical Society, 150 (7) (2003) A1008-A1015.

[9] X. Ye, M.D. LeVan, Water transport properties of Nafion membranes Part I. Single-tube membrane modulre for air drying, Journal of Membrane Science, 221 (2003) 147-161.

[10] X. Ye, M.D. LeVan, Water transport properties of Nafion membranes Part II. Multi-tube membrane module for air drying, Journal of Membrane Science, 221 (2003) 163-173.

[11] S.C. Yeo, A. Eisenberg, Physical properties and supermolecular structure of perfluorinated ion-containing (Nafion) polymers, Journal of Applied Polymer Science, 21 (1977) 875.

[12] T.A. Zawodzinski, L.O. Sillerud, S. Gottesfeld, Determination of water diffusion coefficients in perfluorosulfonate ionometric membranes, Journal of Physical Chemistry, 95 (1991) 6040.

CHAPTER VI

WATER TRANSPORT PROPERTIES OF NAFION® MEMBRANE MODULES EFFECTS OF SCALE

6.1 Introduction

Recently, Nafion® membranes have gained the interest of NASA for use as a pretreatment for air revitalization.[4] Currently NASA employs desiccant dryers to remove the water vapor associated with the cabin air, and these are highly energy intensive. By utilizing a shell and tube membrane, the size of the desiccant dryers required could be reduced significantly.[4] However, the flow rates required for the carbon dioxide removal assembly (CDRA) are much higher than previously characterized membranes are capable of handling.

In this paper we determine the effects of scale on the performance of a concentric tube Nafion® membrane module consisting of 7000 tubes in a shell in countercurrent operation. We solve a system of nonlinear equations numerically for mass and energy transport in order to develop concentration and temperature profiles as well as determine the membrane's efficiency based on the surface area utilized. We believe this is the first study performed which attempts to determine the effects of scale on the dehydration performance of such a membrane module.

6.2 Experiments

The experimental apparatus used to determine scaling effects of a Nafion® membrane module in a shell and tube configuration is shown in Figure 6.1. We used a membrane module purchased from PermaPure, Inc. (PR-178-02-01) consisting of 7000 tubes housed within a polypropylene shell. The tubes are gathered together in a set of 30 bundles centered end to end with common headers. The full membrane dimensions are shown in Table 6.1.

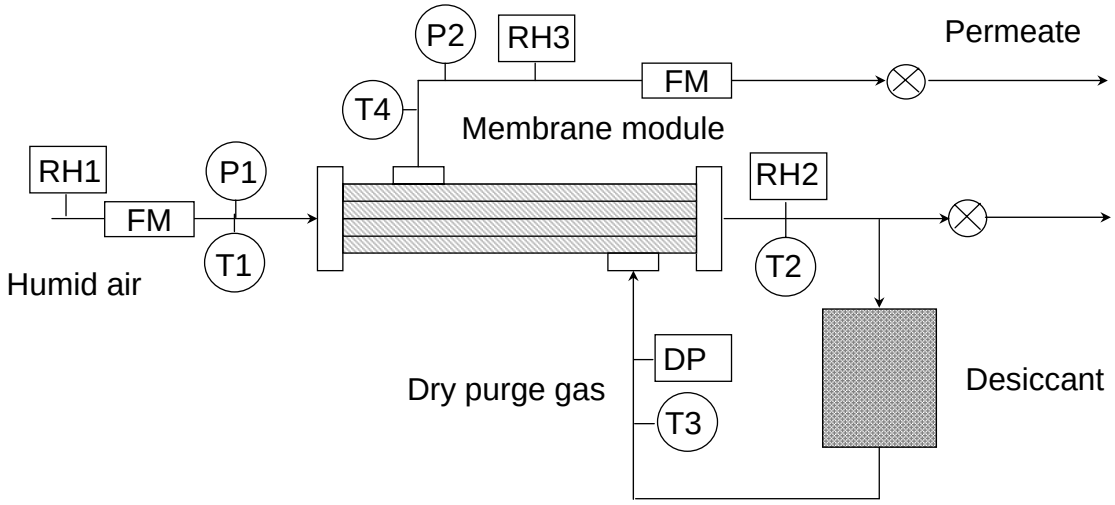

Figure 6.1: Diagram of the apparatus for the removal of water vapor using a shell and tube Nafion® multi-tube membrane module under counter-current operation which uses three relative humidity sensors (RH), four thermocouples (T), two mass flow meters (FM), two pressure transducers (P), and a dew point sensor (DP).

Table 6.1: Table of membrane dimensions and values for parameters used in our model.

Membrane dimensions	
N_t	7000
L	0.726 m
Tube ID	0.97 mm
Tube OD	1.1 mm
l_m	0.13 mm
Shell ID	152 mm
Model parameters	
C_{pa}	1010 J/Kg K
C_{pw}	4180 J/Kg K
k_m	0.15 W/m s
μ_a	1.86 Kg/m s
ρ_a	1.185 Kg/m^3
T_{ref}	298 K
D_{wa}	2.64x10^{-4} m^2/s

To generate a feed stream, compressed laboratory air was fed to a packed drip column in which the water temperature was controlled through the use of a heat exchanger. Next the stream passed through a filter to remove any condensate ensuring that only water vapor exists before being heated to room temperature via an electrical resistance heater. The relative humidities of each experiment were produced by varying the temperature of the water in the drip column. Before entering the tube side of the membrane module, the flow rate, temperature, relative humidity, and pressure were measured using a venturi meter, thermocouple, Vaisala RH meter, and a digital pressure gauge. As the stream exited the tubes of the membrane, the relative humidity and temperature were measured once again by using a Vaisala RH meter. Feed streams were generated at varying relative humidities.

Before the gas stream could enter the shell side, it passed through a desiccant bed of 5A zeolite to remove as much water as possible. The desiccant was regenerated before each experiment by being heated in an oven under vacuum overnight. To determine the relative humidity and temperature of the purge gas, a Panametrics

dew point sensor in conjunction with a thermocouple was used upstream of the shell-side inlet. Finally, as the purge gas exited, the flow rate, temperature and pressure were measured once again. Two valves are connected to the membrane apparatus in order to change the flow rate of the purge gas and to maintain a constant back pressure.

6.3 Mathematical Model

We examine mass and energy transfer in a water selective shell and tube membrane under counter-current operation. A representative schematic of the membrane modeled is shown in Figure 6.2. A humid air stream that is to be dehydrated is fed to the tube side of the membrane at room temperature, while a dry purge gas stream enters the shell side at the opposite end. As the air stream flows through the length of the membrane, water selectively permeates from the tubes to the shell and is swept out by the purge gas. We assume that only water vapor permeates as experiments have shown that permeation rates through Nafion of oxygen and nitrogen were several orders of magnitude lower than that of water. We also assume that axial diffusion is negligible compared with the bulk flow, the process and purge gases may be treated as ideal, the system is adiabatic, and the end effects of the membrane are negligible.

Mass transfer

We write an overall material balance for the membrane in the form

$$N_t F_t^{tot} \left(y_{tw}|_{z=L} - y_{tw}|_{z=0} \right) = F_s^{tot} \left(y_{sw}|_{z=0} - y_{sw}|_{z=L} \right) \tag{6.1}$$

where N_t is the number of tubes in the membrane, F_t^{tot} is the total molar flow rate per tube, F_s^{tot} is the total molar flow rate in the shell, and y_{tw} and y_{sw} are the position dependent mole fractions of water inside the tube and shell respectively. We let

$$F_t^{tot} = \frac{F_t^{air}}{(1 - y_{tw})} \qquad F_s^{tot} = \frac{F_s^{air}}{(1 - y_{sw})} \tag{6.2}$$

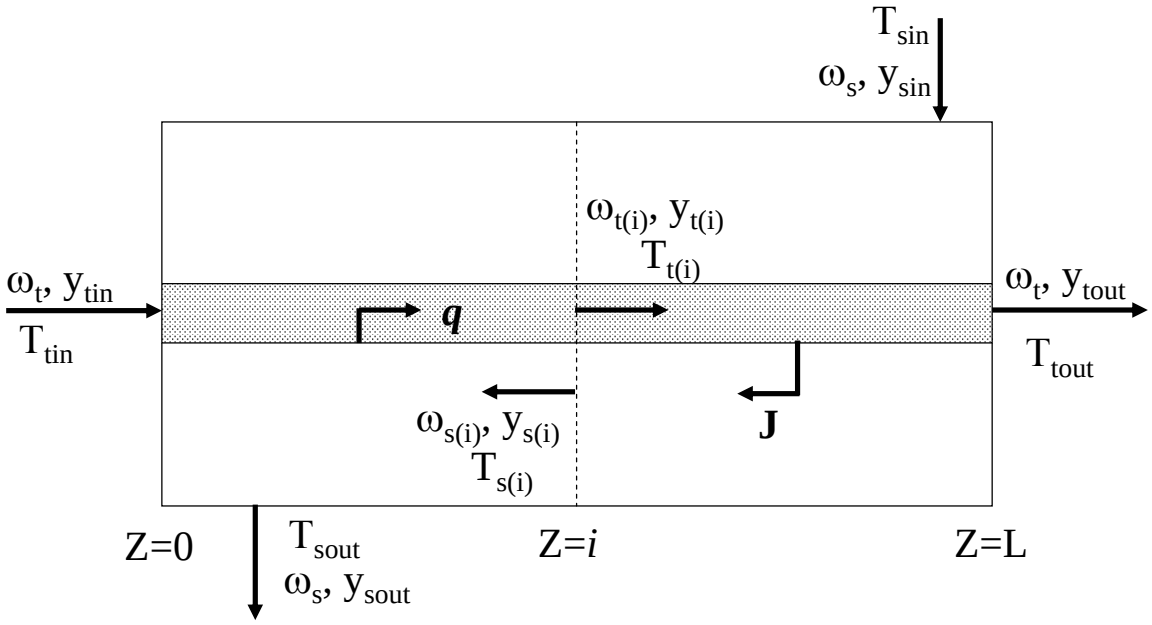

Figure 6.2: Representative diagram of shell and tube membrane under counter-current operation.

where F_t^{air} and F_s^{air} are the molar flow rates of dry air in the tube and shell, respectively, which we assume to remain constant along the length of the membrane.

We adopt a three resistance model to describe the water flux from the tube-side bulk fluid to the corresponding membrane interface, through the membrane, and from the opposite membrane interface to the corresponding shell fluid for each axial position as given by

$$J_1 = -k_t \left(c_{tmt} y_{mtw} - c_{tt} y_{tw}\right) \tag{6.3}$$

$$J_2 = -\frac{1}{l_m} \int_{P_{mtw}}^{P_{msw}} D \frac{\partial c_w}{\partial P_w} dP_w \tag{6.4}$$

$$J_3 = -k_s \left(c_{tms} y_{msw} - c_{ts} y_{sw}\right) \tag{6.5}$$

where y_{mtw} and y_{msw} are the mole fractions of water in the tube and shell-side films respectively, and c_{tt}, c_{tmt}, c_{tms}, and c_{ts} are the total molar concentrations in the bulk fluid of the tube, the tube-side film, the shell-side film, and the bulk fluid in the shell, respectively. The limits of integration of the flux through the membrane, J_2, are the partial pressures of water in the shell and tube-sides, i.e., P_{msw} and P_{mtw}. The values for the shell and tube convective mass transfer coefficients, k_t and k_s, were obtained using the correlations Shah and London[6] developed for laminar fluid flow across tube bundles and inside the tubes, or those developed by Gnielinski[2] for transitional fluid flow given by

$$Sh = (\zeta/8)\left(Re - 1000\right) \frac{Sc}{\left(1 + 12.7\left(\zeta/8\right)\right)^{1/2}} \left(Sc^{2/3} - 1\right) \tag{6.6}$$

with

$$\zeta = \frac{0.316}{Re^{1/4}} \tag{6.7}$$

where Sh is the Sherwood number, Sc is the Schmidt number, and Re is the Reynolds number. Ye and LeVan[8] provide a relationship for the diffusion coefficient of a single tube module written

$$D = \frac{Pe_m}{V_{std} \times 10^4 \left(\partial c_w / \partial P_w\right)} \tag{6.8}$$

where V_{std} is the molar volume of gas at a standard state, and Pe_m is the permeability of water through the membrane for a single tube as a function of the partial pressure of water given by

$$Pe_m = \frac{2.8 \times 10^{-6} P_w^{3/2}}{P_{atm}} \tag{6.9}$$

The diffusion coefficient in equation 6.8, D, is inversely proportional to the slope of the water adsorption curve, $\partial c_w / \partial P_w$, determined from the partial derivative of the ratio of the moles of water to the sulfonic acid sites, λ, with respect to the partial pressure of water

$$\frac{M_{Naf}}{\rho_{Naf}} \frac{\partial c_w}{\partial P_w} = \frac{\partial_\lambda}{\partial P_w} \tag{6.10}$$

and yields

$$\frac{\partial c_w}{\partial P_w} = \frac{\rho_{Naf}}{M_{Naf}} \left(\frac{17.81}{P_{sat}} - \frac{79.2}{P_{sat}^2} P_w + \frac{108}{P_{sat}^3} P_w^2 \right) \tag{6.11}$$

where ρ_{Naf} and M_{Naf} are the density and molecular weight of Nafion®, respectively, and P_{sat} is the saturated vapor pressure for water.

In their second paper, Ye and LeVan[9] discuss the impact that the membrane thickness has on the permeability of the membrane concluding that a simple proportionality relationship does not adequately consider interfacial skin effects. Instead, they develop a permeability for a multi-tube membrane module determined empirically as

$$Pe_m = \frac{1.1 \times 10^{-6} P_w^{3/2}}{P_{atm}} \tag{6.12}$$

Substituting equation 6.12 into equation 6.8 yields

$$D = \frac{1.1 \times 10^{-6} P_w^{3/2}}{P_{atm} V_{std} \left(\partial c_w / \partial P_w \right)} \tag{6.13}$$

We then introduce a temperature dependence for the diffusion coefficient in equation 6.13 given by

$$D = \frac{1.1 \times 10^{-6} P_w^{3/2}}{P_{atm} V_{std} \left(\partial c_w / \partial P_w \right)} \exp\left[-2416 \left(1/T - 1/298 \right) \right] \tag{6.14}$$

At steady state the molar rate of transfer of water for each film and through the membrane are equal at any axial position, i.e.,

$$J_1 dA_1 = J_2 dA_2 = J_3 dA_3 \tag{6.15}$$

where dA_1 and dA_3 are the differential cross-sectional areas inside and outside a tube, respectively and dA_2 is the logarithmic mean of the two.

We relate the rate at which the tube-side mass changes to the mass flux to the membrane interface by equating a tube-side mass balance with an area integral of the tube-side interfacial resistance given by

$$F_t^{air}\left(\frac{y_{tw(i+1)}}{\left(1-y_{tw(i+1)}\right)}-\frac{y_{tw(i)}}{\left(1-y_{tw(i)}\right)}\right)=-\int_{A_{id}} J_1\, dA_{id} \tag{6.16}$$

where A_{id} is the surface area required for a membrane under ideal operating conditions.

Heat Transfer

The overall energy balance for the system is written

$$\begin{aligned}&\omega_t|_{z=L}\, C_{pt}|_{z=L}\,(T_t|_{z=L}-T_{ref})-\omega_t|_{z=0}\, C_{pt}|_{z=0}\,(T_t|_{z=0}-T_{ref}) \;=\\ &\quad \omega_s|_{z=0}\, C_{ps}|_{z=0}\,(T_s|_{z=0}-T_{ref})-\omega_s|_{z=L}\, C_{ps}|_{z=L}\,(T_s|_{z=L}-T_{ref})\end{aligned} \tag{6.17}$$

where C_{pt} and C_{ps} are the mean specific heats of the tube and shell-side fluids, T_t and T_s are the temperatures of the tube and shell-side fluids, and ω_t and ω_s are the mass flow rates of the process and purge gas streams, respectively. We assume that temperature changes throughout the membrane module are small enough that the corresponding variations in specific heats are negligible. We then write the specific heat in terms of the molar fraction of water

$$C_{pt} = C_{pw} M_w y_{tw(i)} + C_p M_a \left(1 - y_{tw(i)}\right) \tag{6.18}$$

$$C_{ps} = C_{pw} M_w y_{sw(i)} + C_{pa} M_a \left(1 - y_{sw(i)}\right) \tag{6.19}$$

where the subscript i denotes axial position, M_w and M_a are the molecular weights of water and dry air, and C_{pw} and C_{pa} are the specific heats of water and dry air respectively. The conversion of mass flow rates to molar flow rates and substitution of equations 6.18 and 6.19 in equation 6.17 yields

$$\begin{aligned} N_t F_t^{air} \left(C_{pw} M_w \frac{y_{tw(i+1)}}{\left(1 - y_{tw(i+1)}\right)} + C_{pa} M_a \right) \left(T_{t(i+1)} - T_{ref} \right) \\ -N_t F_t^{air} \left(C_{pw} M_w \frac{y_{tw(i)}}{\left(1 - y_{tw(i)}\right)} + C_{pa} M_a \right) \left(T_{t(i)} - T_{ref} \right) \quad = \\ F_s^{air} \left(C_{pw} M_w \frac{y_{sw(i)}}{\left(1 - y_{sw(i)}\right)} + C_{pa} M_a \right) \left(T_{s(i)} - T_{ref} \right) \\ -F_s^{air} \left(C_{pw} M_w \frac{y_{sw(i+1)}}{\left(1 - y_{sw(i+1)}\right)} + C_{pa} M_a \right) \left(T_{s(i+1)} - T_{ref} \right) \end{aligned} \tag{6.20}$$

where T_{ref} is a reference temperature set equal to 298 K.

We use an analogous 3 resistance model to describe the energy flux from the bulk phases to the membrane interfaces and through the membrane itself. Rate equations are

$$q_1 = -h_t \left(T_t - T_{mt} \right) \tag{6.21}$$

$$q_2 = -\frac{k_m}{l_m} \left(T_{mt} - T_{ms} \right) \tag{6.22}$$

$$q_3 = -h_s \left(T_s - T_{ms} \right) \tag{6.23}$$

where T_{mt} and T_{ms} are the interfacial membrane temperatures. We use analogous correlations that parallel those for mass transfer to calculate the convective heat transfer coefficients in the shell and tube, h_s and h_t, respectively. We assumed a constant value for the membrane thermal conductivity, k_m, ascertained by Khandelwal and Mench.[3]

Similarly to mass transfer, the steady state rates of enthalpy transfer are set equal, i.e.,

$$q_1 dA_1 = q_2 dA_2 = q_3 dA_3 \tag{6.24}$$

and we relate the enthalpy change in the tubes to the interfacial energy flux using

$$\begin{aligned} F_t^{air}\left(C_{pw}M_w\frac{y_{tw(i+1)}}{\left(1-y_{tw(i+1)}\right)}+C_{pa}M_a\right)\left(T_{t(i+1)}-T_{ref}\right) \\ -F_t^{air}\left(C_{pw}M_w\frac{y_{tw(i)}}{\left(1-y_{tw(i)}\right)}+C_{pa}M_a\right)\left(T_{t(i)}-T_{ref}\right) \\ =-\int_{A_{id}} q_1\, dA_{id} \end{aligned} \tag{6.25}$$

We introduce overall efficiency terms into our models for mass and energy transport to account for any flow maldistributions by

$$A\,\eta_M = A_{id} \tag{6.26}$$

and

$$A\,\eta_T = A_{id} \tag{6.27}$$

where A is the actual surface area utilized accounting for poor flow distribution. Equations 6.26 and 6.27 are substituted into the corresponding tube-side mass and energy balance, equations 6.16 and 6.25, to give

$$F_t^{air}\left(\frac{y_{tw(i+1)}}{\left(1-y_{tw(i+1)}\right)}-\frac{y_{tw(i)}}{\left(1-y_{tw(i)}\right)}\right)=-\eta_M\int_A J_1\, dA \tag{6.28}$$

and

$$\begin{aligned} F_t^{air}\left(C_{pw}M_w\frac{y_{tw(i+1)}}{\left(1-y_{tw(i+1)}\right)}+C_{pa}M_a\right)\left(T_{t(i+1)}-T_{ref}\right) \\ -F_t^{air}\left(C_{pw}M_w\frac{y_{tw(i)}}{\left(1-y_{tw(i)}\right)}+C_{pa}M_a\right)\left(T_{t(i)}-T_{ref}\right) \\ =-\eta_T\int_A q_1\, dA \end{aligned} \tag{6.29}$$

6.4 Results and Discussion

In order to characterize the performance of the Nafion^{TM}shell and tube membrane module from our experiments, we solve the coupled mass and energy equations numerically with the aid of a generalized nonlinear equation solver that applies a modified Powell method.[1] We model the membrane module in Figure 6.2 as a set of

differential elements in series by partitioning the membrane into j subdivisions with axial positions ranging from $i = 1$ at $z = 0$ to $i = j + 1$ at $z = L$.

The results of our model for the concentration profiles are shown in Figures 6.3 through 6.5 for a ratio of the purge gas flow rates to the feed flow rates at approximately 1.1. The tube and shell-side water concentrations are depicted with solid lines and the interfacial water concentrations are the dashed lines. Figure 6.6 shows that the interfacial resistances on the tube and shell-side do not restrict the rate of mass transport to the same extent as that of the resistance in the membrane itself, meaning the diffusion of water through the membrane is the rate limiting factor in the flux of water from the tube to shell side.

At first glance it appears that the concentration gradient is independent of axial position for all feed relative humidities investigated, but upon closer inspection it is evident that the gradient at an axial position of $z = 0$ is larger than that at $z = L$. This is verified by the profile of the water flux through the membrane depicted in Figure 6.7. There it can be seen that the water flux decreases along the length of the membrane, and as the relative humidity of the process gas decreases.

The corresponding temperature profiles of the membrane are displayed in Figures 6.8 through 6.10 with the tube and shell-side values shown with solid curves while the interfacial values are the dashed curves. Unlike water transport, the membrane resistance does not play a significant role in the transfer of energy as opposed to the interfacial resistances, meaning that the temperature profiles are fairly linear. Also, since the purge gas is slightly elevated in temperature due to heat of adsorption effects from the desiccant compared to that in the tubes, the direction of the driving force in terms of shell-side and tube-side values is reversed compared to the water transport.

During the experiments we noticed that there was a distinct radial temperature gradient in the membrane apparatus, meaning that the top was warmer than the

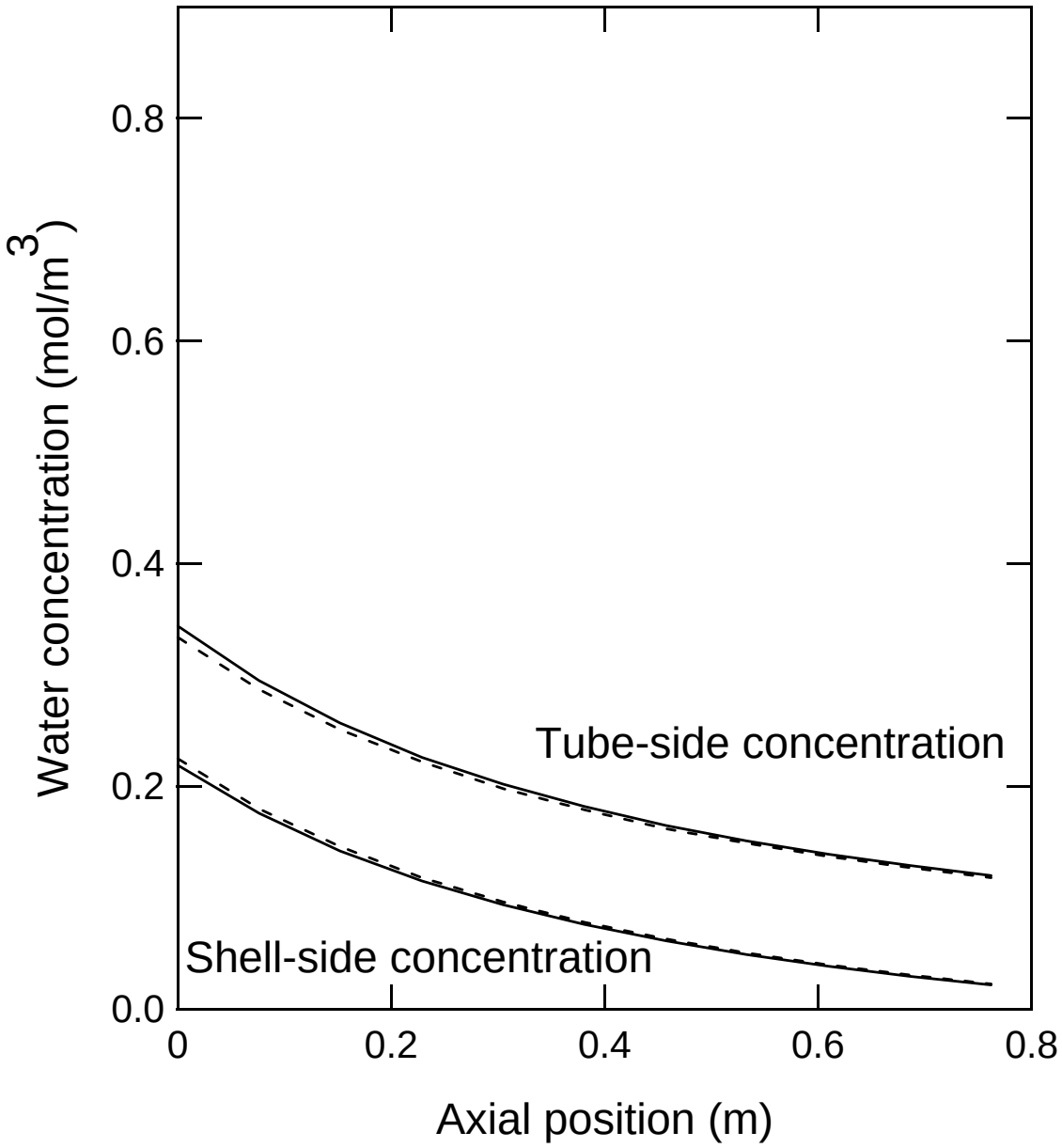

Figure 6.3: Water concentration profile along the length of the membrane for a tube side relative humidity of 33% and a V_s/V_t ratio of 1.1. Solid lines describe water concentration in the bulk fluid while dashed lines describe the water concentration in the tube and shell side films.

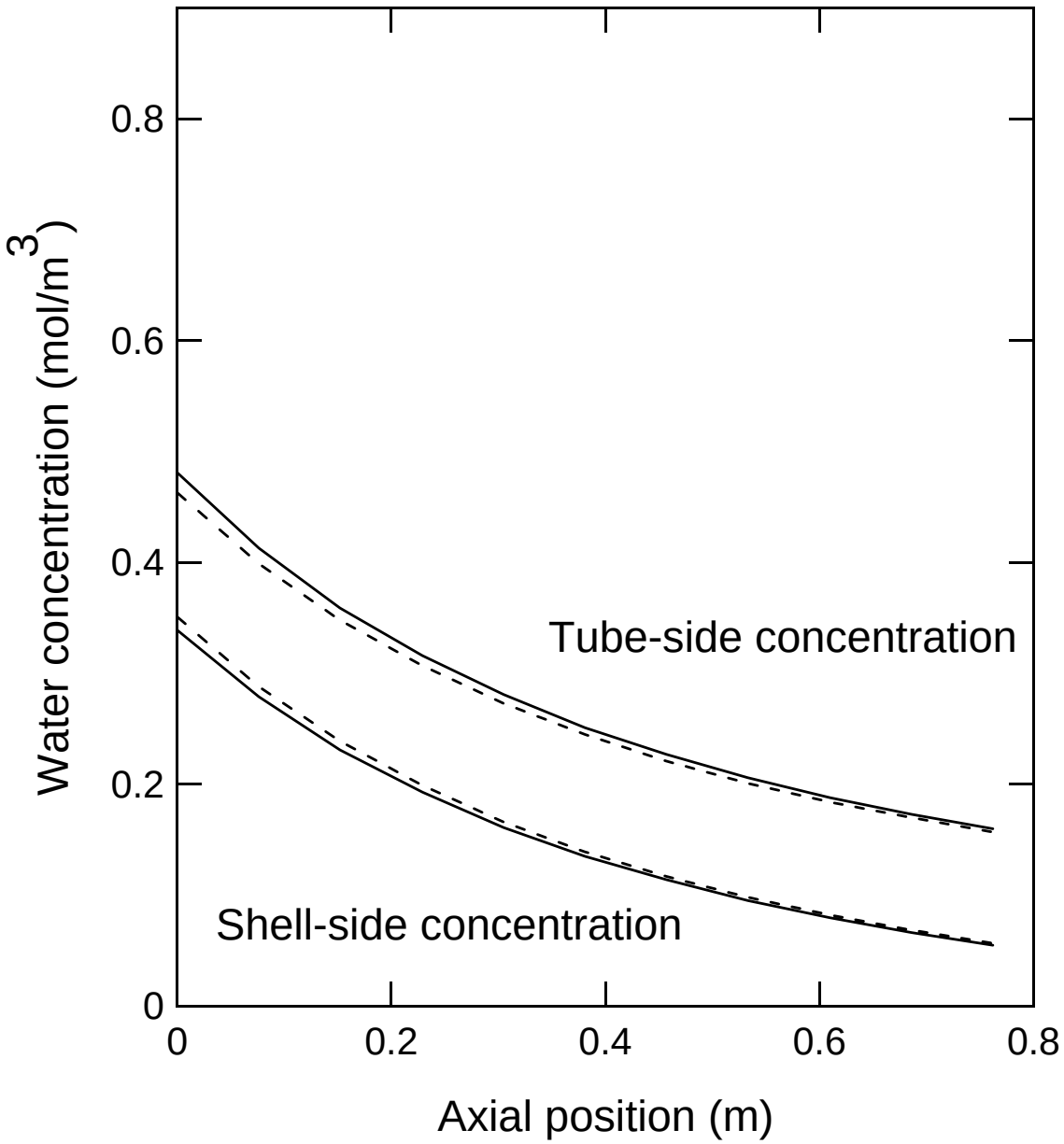

Figure 6.4: Water concentration profile along the length of the membrane for a tube side relative humidity of 45% and a V_s/V_t ratio of 1.1. Solid lines describe water concentration in the bulk fluid while dashed lines describe the water concentration in the tube and shell side films.

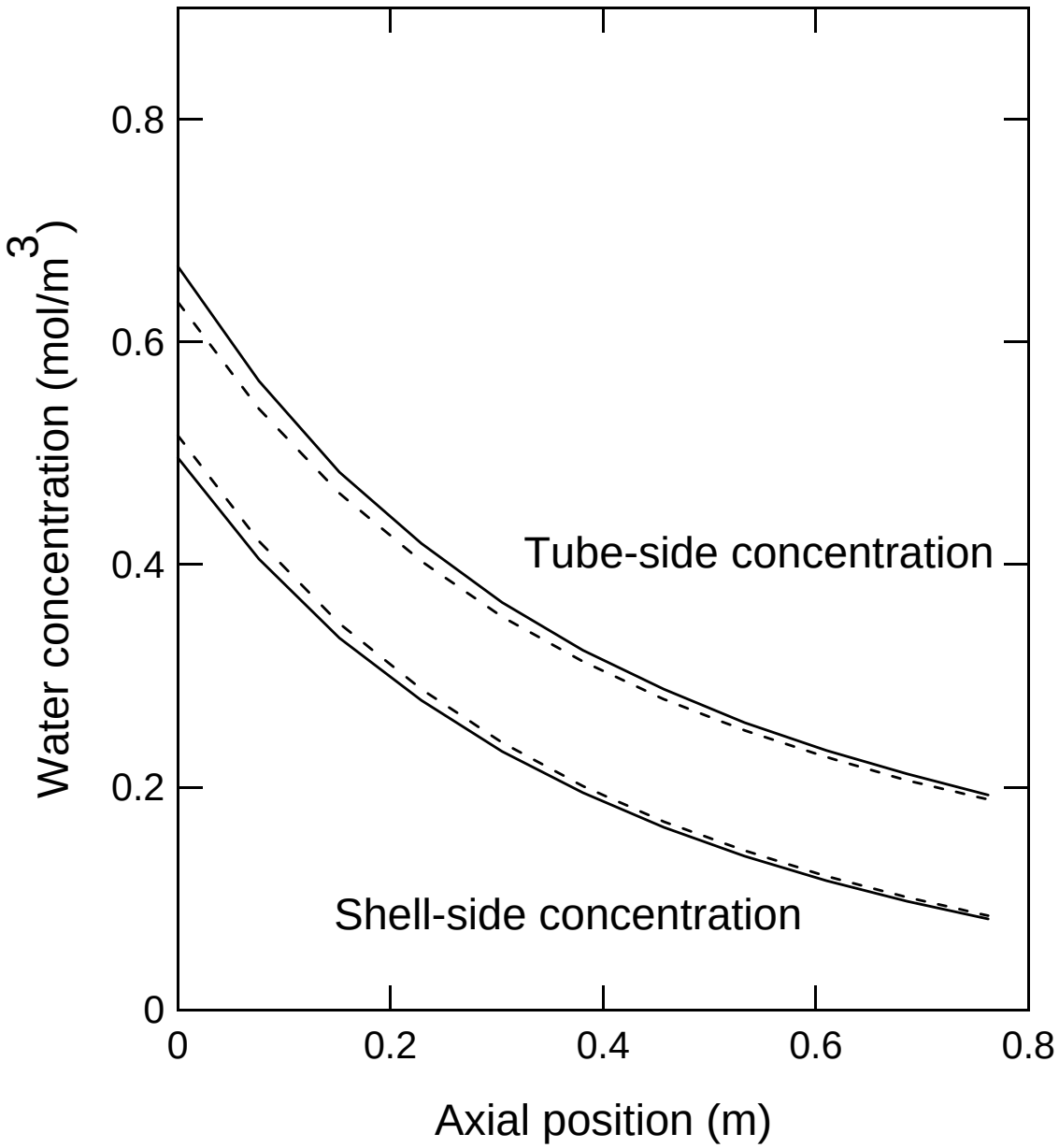

Figure 6.5: Water concentration profile along the length of the membrane for a tube side relative humidity of 45% and a V_s/V_t ratio of 1.1. Solid lines describe water concentration in the bulk fluid while dashed lines describe the water concentration in the tube and shell side films.

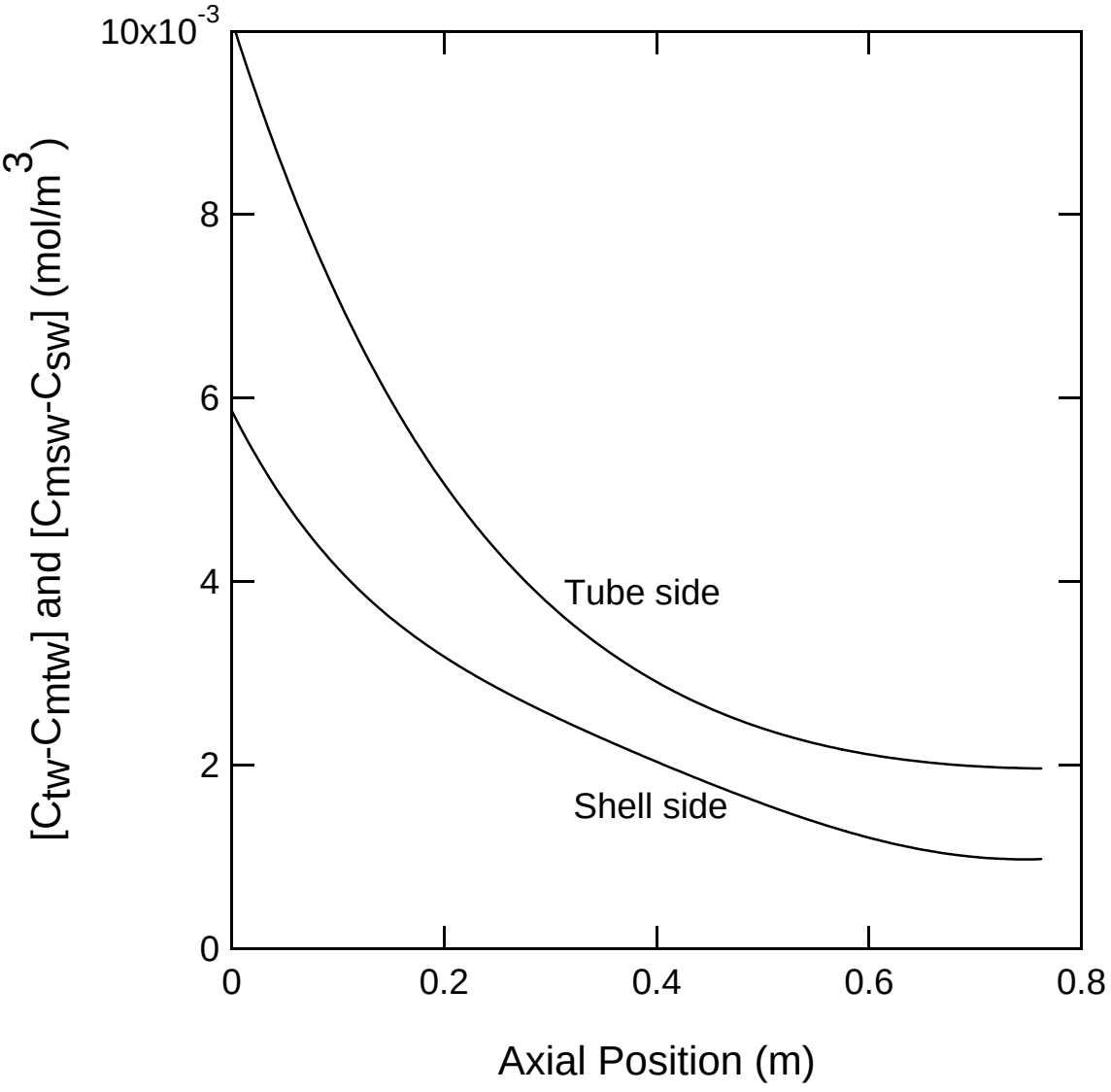

Figure 6.6: Difference between the calculated bulk concentration on the tube and shell side and their corresponding interfacial concentrations for the case shown in Figure 6.3.

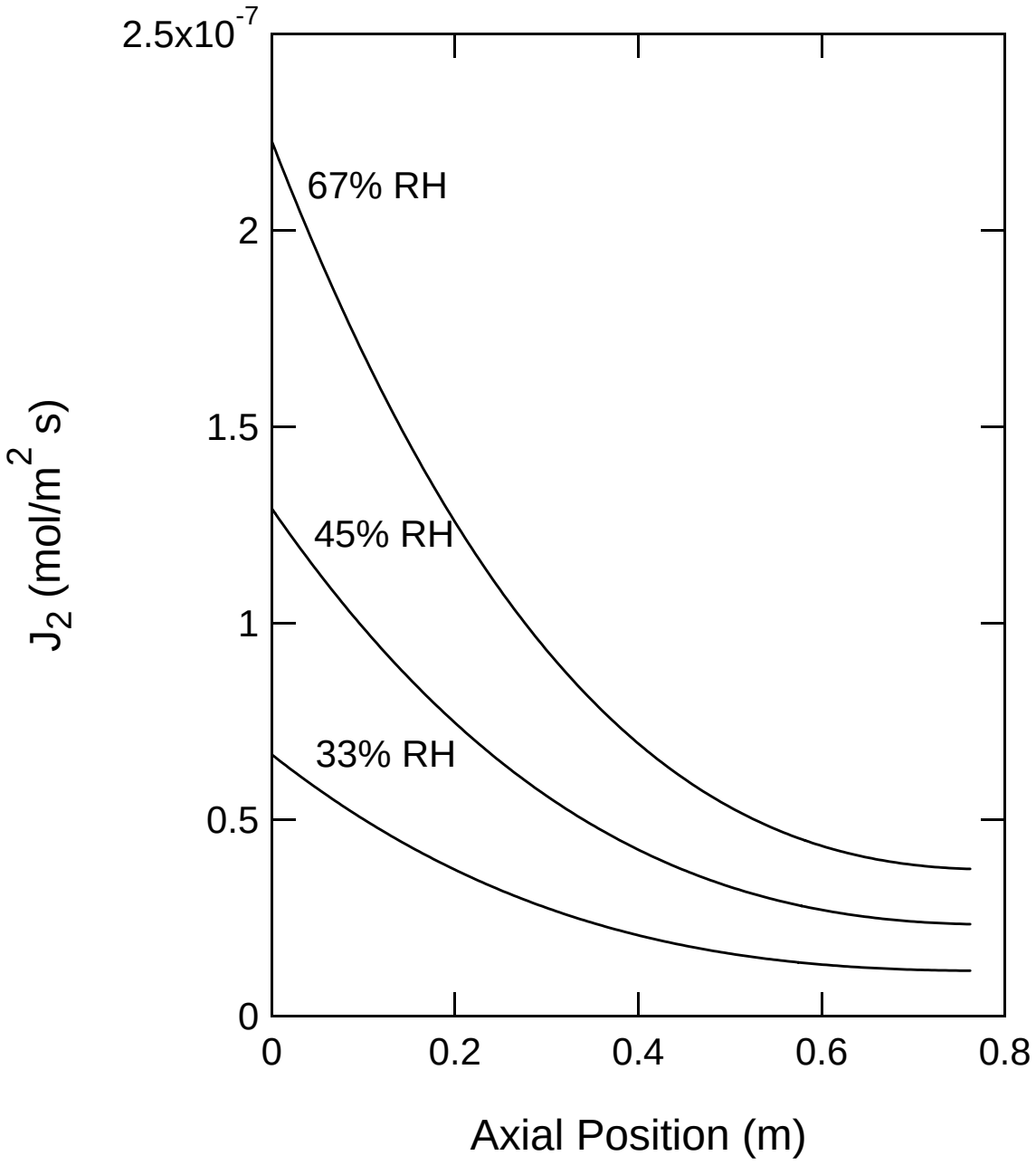

Figure 6.7: Flux of water through the membrane for various relative humidities and a V_s/V_t ratio of 1.1.

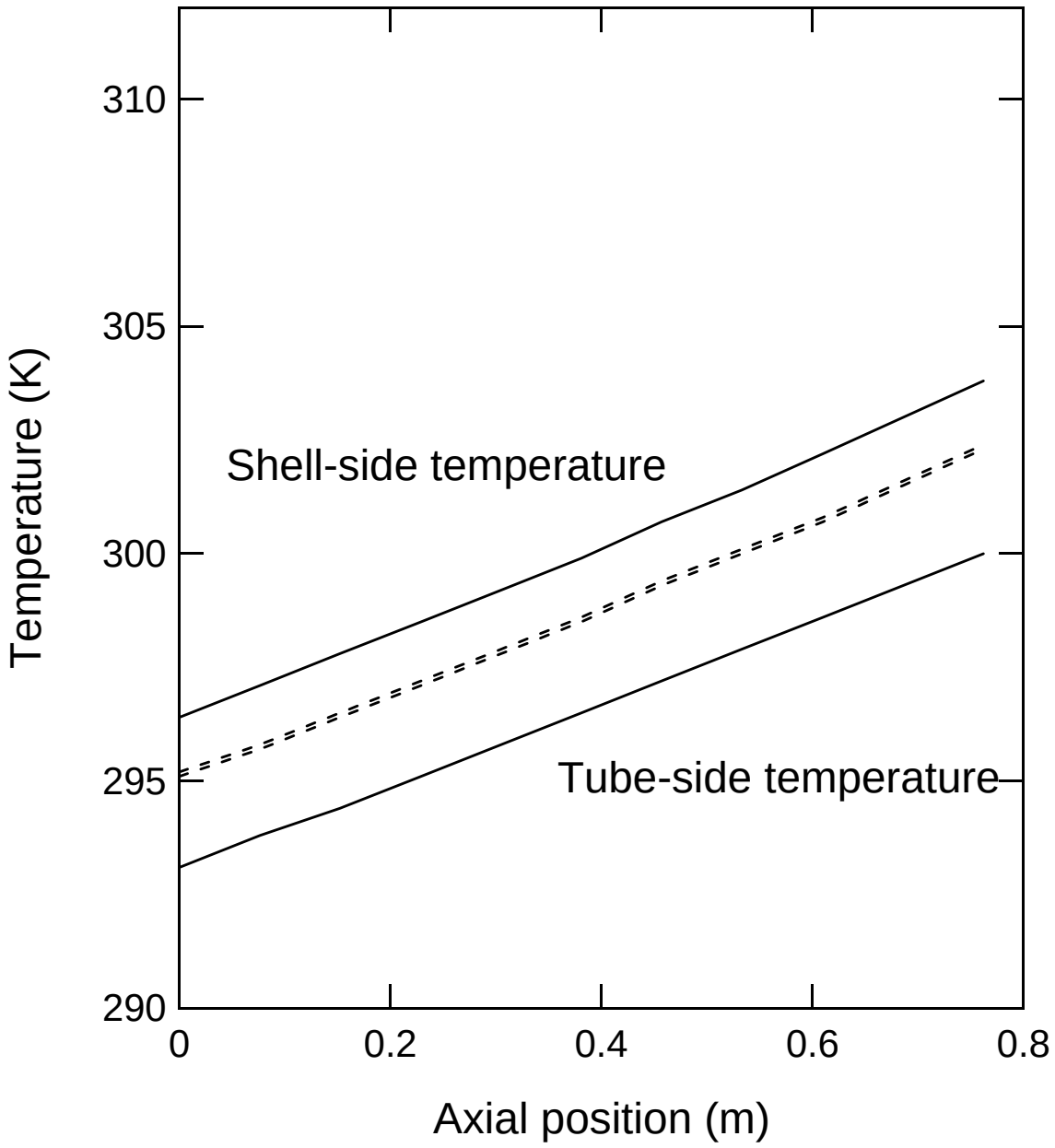

Figure 6.8: Temperature profile along the length of the membrane for a tube side relative humidity of 33% and a V_s/V_t ratio of 1.1. Solid lines describe the temperature in the bulk fluids while dashed lines describe the themperature in the tube and shell side films.

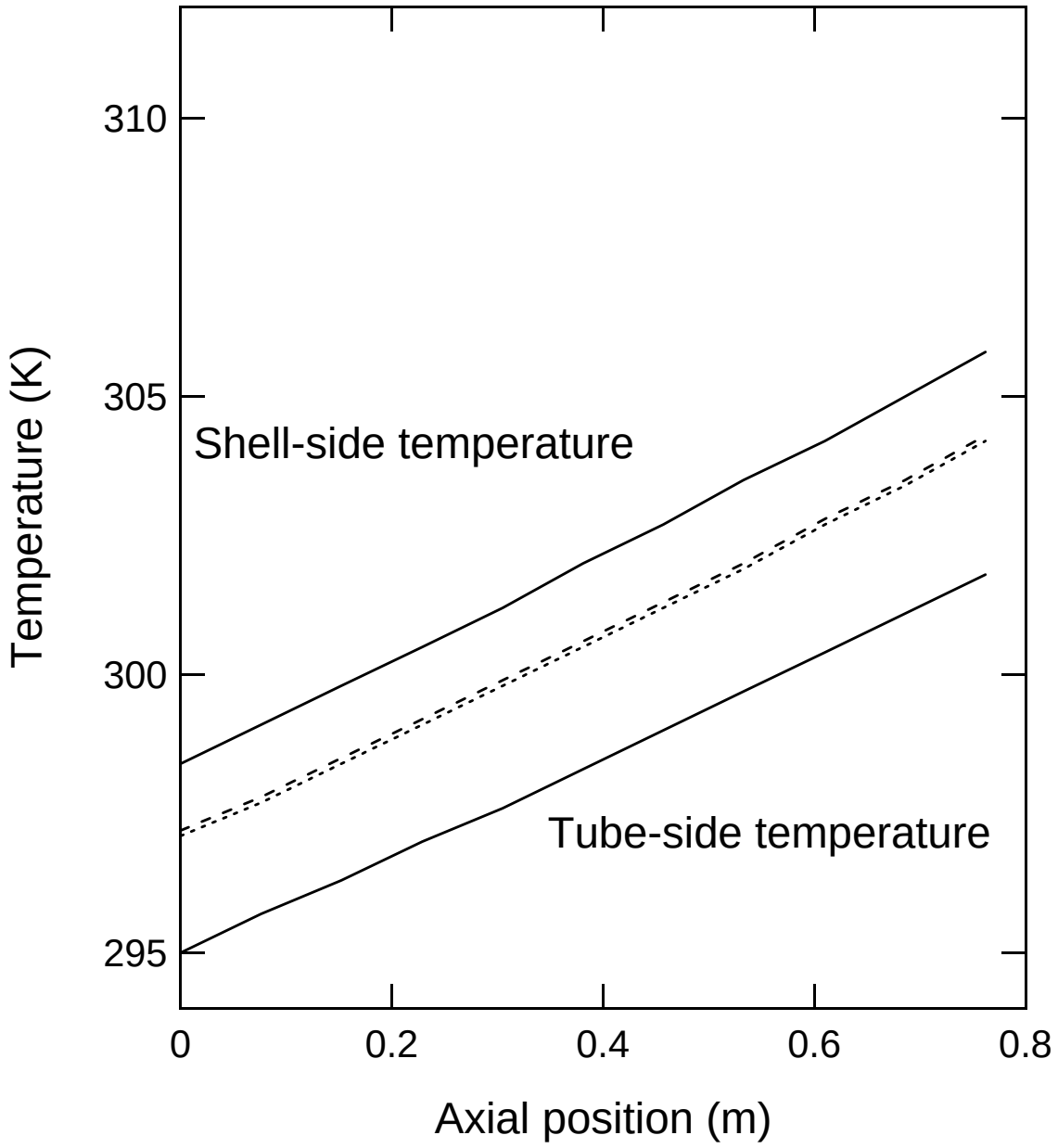

Figure 6.9: Temperature profile along the length of the membrane for a tube side relative humidity of 45% and a V_s/V_t ratio of 1.1. Solid lines describe the temperature in the bulk fluids while dashed lines describe the themperature in the tube and shell side films.

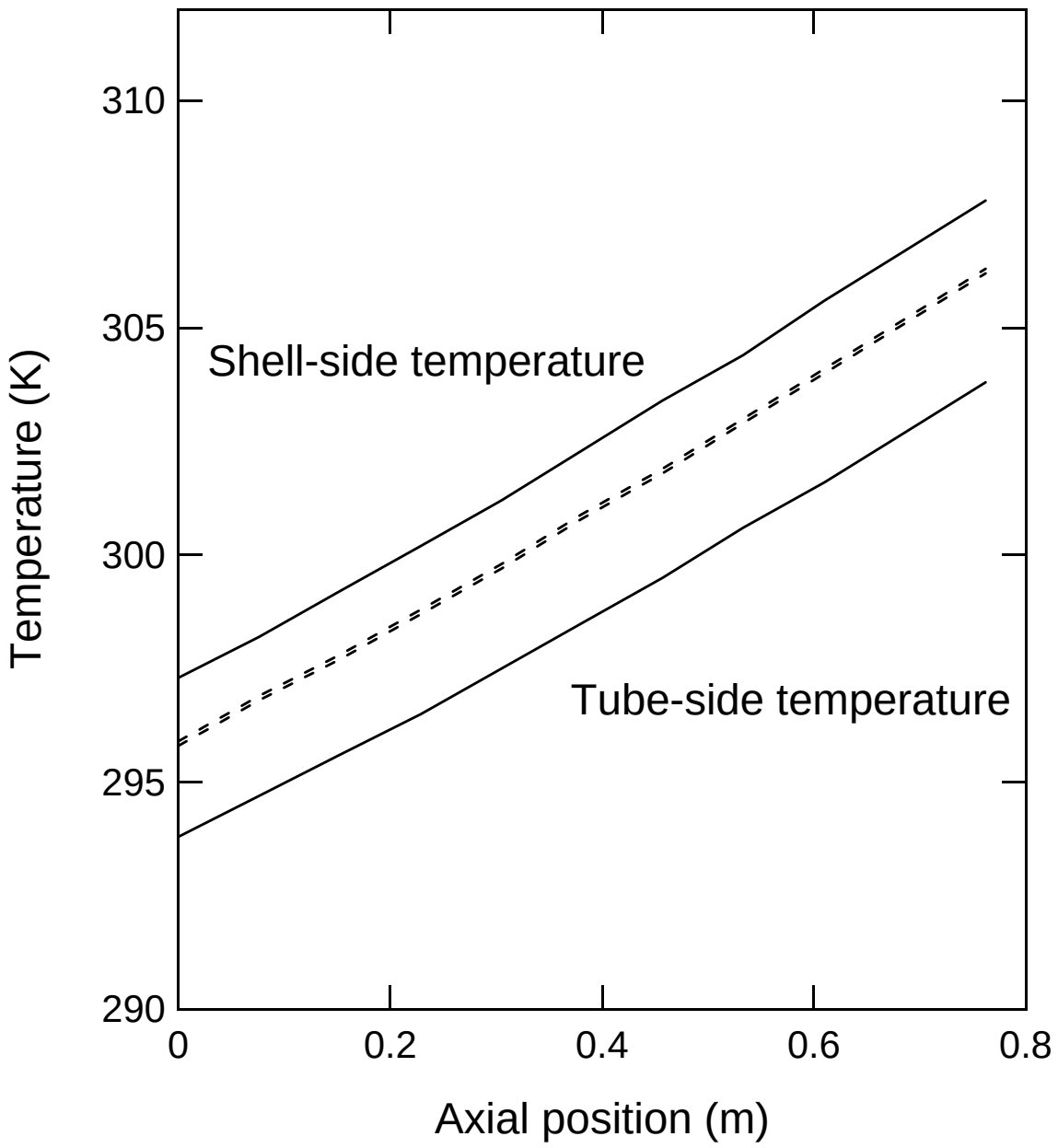

Figure 6.10: Temperature profile along the length of the membrane for a tube side relative humidity of 60% and a V_s/V_t ratio of 1.1. Solid lines describe the temperature in the bulk fluids while dashed lines describe the themperature in the tube and shell side films.

bottom as the module was mounted in a horizontal orientation. This temperature gradient led us to conclude that the flow of the shell-side purge gas was not evenly distributed through all sections of tubes across the cross section of the membrane module, meaning that the surface area utilized for the mass and energy transport was being limited by channeling effects on the shell side. This has a large impact on our model, in which it is assumed that the purge gas is distributed across the surface area of the tubes evenly.

The calculated values for the surface area utilization efficiencies for water permeation, i.e., η_M, are plotted for varying feed relative humidities against the ratio of purge to feed gas, V_s/V_t, in Figure 6.11. It can be seen that as the V_s/V_t ratio decreases, η_M decreases, suggesting that the flow distribution on the shell side becomes less ideal as the purge gas flow rate is reduced. Alternatively, as the feed relative humidity increases, η_M decreases implying that the membrane's performance should be improving as the membrane is hydrated but the transport due to forced convection on the shell side is not as effective as theory predicts. These are good indicators of flow maldistribution occurring on the shell side and that the membrane is not dehydrating the feed stream as predicted.

6.5 Conclusions

Mathematical models were developed and solved in conjunction with experiments for the dehydration of a feed stream using a multi-tube shell and tube membrane under counter-current operation in order to determine the effects of scale. The models accounted for two interfacial resistances and resistance in the membrane for both heat and mass transport. Several cases were examined in which the relative humidity of the feed stream varied from 33% to 60% as well as the V_s/V_t ratio varied from 0.7 to 1.1.

We determined that a lack of uniform flow pattern on the shell-side created by

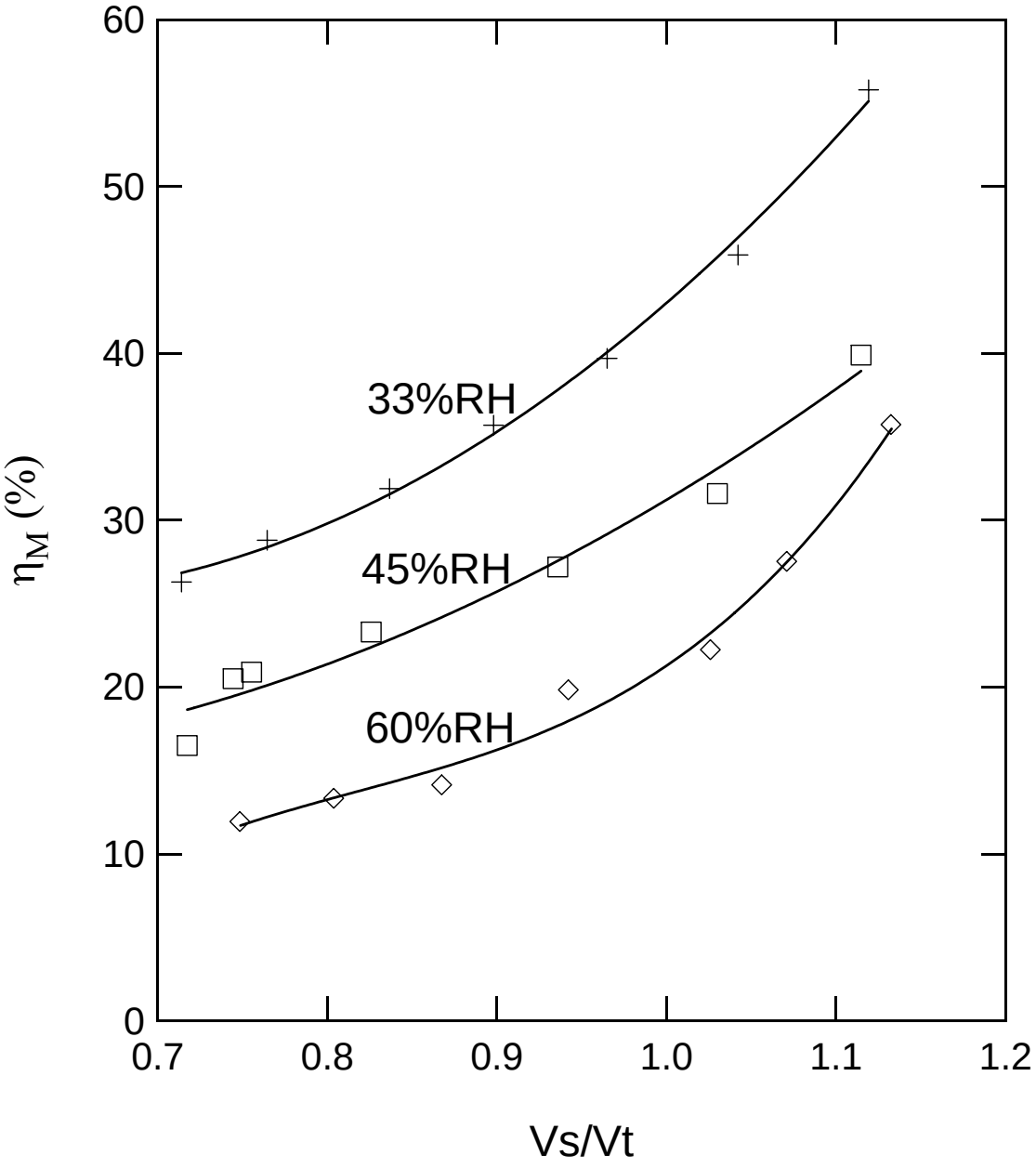

Figure 6.11: Calculated surface area utilization efficiencies of various feed relative humidities

irregular membrane packing caused the efficiency to decrease with increasing relative humidity and decreasing V_s/V_t ratio, resulting in the membrane's performance to be lower than predicted. We also determined that the interfacial resistances had little impact on the rate of mass transport, which was impeded mostly by diffusional limitations. Conversely, the rate of heat transport was mostly affected by interfacial resistances and not thermal conductivity limitations within the membrane.

Efforts could be made to generate a more uniform flow distribution pattern to improve transport by orienting the membrane vertically, and perhaps utilizing a baffle system on the shell side. In order for design of future membrane systems capable of handling large throughputs it is important to generate a uniform flow pattern in the shell side.

Notation:

A	measured surface area, m^2
A_{id}	surface area required for an ideal case, m^2
C_p	specific heat, J/kg K
c_t	total concentration, mol/m^3
D	diffusion coefficient through the membrane, m^2/s
D_{wa}	diffusivity of water vapor in air, m^2/s
dA_1, dA_2, dA_3	differential resistance areas, m^2
F^{tot}	total molar flow rate, mol/s
F^{air}	molar flow rate of dry air, mol/s
h	convective heat transfer coefficient, W/m^2 s
J_1, J_2, J_3	local molar fluxes, mol/m^2 s
k	convective mass transfer coefficient, mol/m^2 s
k_m	thermal conductivity of the membrane, W/m s
l_m	thickness of the membrane, m
M	molecular weight, g/mol
N_t	number of tubes in the membrane
P_w	partial pressure of water, kPa
q_1, q_2, q_3	local heat flux, J/m^2 s
Re	Reynold's number
Sc	Schmidt number
T	temperature, K
V_{std}	molar volume of an ideal gas at stp, m^3/mol
y	mole fraction
z	axial dimension

Greek Letters

η	overall efficiency
ω	mass flow rate, kg/s
ζ	function used in Gnielinski's correlation
μ_a	viscosity of dry air, kg/m s
ρ_a	density of air, kg/m^3

Subscripts

a	air
ms	shell-side interface
mt	tube-side interface
ref	reference state
s	shell side
t	tube side
w	water

References

[1] B.S. Garbow, K.E. Hillstrom, J. Jorge, Minpack Project, Argonne National Laboratory, March 1980.

[2] V. Gnielinski, New equations for heat and mass transfer in turbulent pipe and channel flow, International Chemical Engineering, 16 (1976) 359.

[3] M. Khandelwal, M.M. Mench, Direct measurement of through-plane thermal conductivity and contact resistance in fuel cell membranes, Journal of Power Sources, 161 (2006) 1106-1115.

[4] L. Mulloth, M. Varghese, B. Luna, J. Hogan, M.D. LeVan, J.R. Moate, Development of a low-power CO_2 removal and compression system for closed-loop air revitalization in future spacecraft, SAE International, Paper 2005-01-2944 (2005) 1-8.

[5] M.S. Rosen, L.M. Mulloth, D.L. Affleck, Y. Wang, M.D. LeVan, Development and testing of a temperature-swing adsorption compressor for carbon dioxide in closed-loop air revitalization systems, SAE International, Paper 2005-01-2941 (2005) 1-6.

[6] R.K. Shah, A.L. London, Supplement 1 to Advances in Heat Transfer; Academic Press: New York, 1978.

[7] T.E. Springer, T.A. Zawodzinski, S. Gottesfeld, Polymer electrolyte fuel cell model, Journal of the Electrochemical Society, 138 (1991) 2334-2342.

[8] X. Ye, M.D. LeVan, Water transport properties of Nafion membranes Part I. Single-tube membrane module for air drying, Journal of Membrane Science, 221 (2003) 147-161.

[9] X. Ye, M.D. LeVan, Water transport properties of Nafion membranes Part II. Multi-tube membrane module for air drying, Journal of Membrane Science, 221 (2003) 163-173.

[10] S.C. Yeo, A. Eisenberg, Physical properties and supermolecular structure of perfluorinated ion-containing (Nafion) polymers, Journal of Applied Polymer Science, 21 (1977) 875.

[11] T.A. Zawodzinski, L.O. Sillerud, S. Gottesfeld, Determination of water diffusion coefficients in perfluorosulfonate ionometric membranes, Journal of Physical Chemistry, 95 (1991) 6040.

CHAPTER VII

CONCLUSIONS AND RECOMMENDATIONS

The work presented in this dissertation considers the use of temperature swing adsorption in the capture and compression of CO_2 from a feed stream using a bed of 5A zeolite, the importance of uniform heating within a TSA bed and the impact nonuniform heating has on desorption equilibria within the bed, the development of a perturbation solution to describe breakthrough behavior in fixed-bed adsorption for a nonplug flow described by a constant pattern, the modeling of experimental data for a shell and tube Nafion® multi-tube membrane module with a vacuum on the shell side in lieu of a purge stream, and the effects of scale on the operation of a shell and tube Nafion® multi-tube membrane module under counter-current operation.

The principle findings of this research are:

Temperature Swing Adsorption Compression

- The minimum total volume of a two-stage TSA compressor is closely related to the equilibration pressure of the two stages.
- Initiating an adsorption half-cycle in a TSA bed immediately following desorption has a negative impact on performance and will blow any adsorbate accumulated in the fluid phase out of the bed.
- The value of the effective thermal conductivity has a significant impact on the performance of a TSA bed, and efforts can be made to increase a TSA bed's effective thermal conductivity through careful examination of the geometry.
- Imbalanced heating loads of a TSA bed negatively affects the bed's performance, therefore proper control of the energy supplied to the bed during desorption ensuring an even distribution throughout.

Breakthrough Behavior of Fluids with Slightly Favorable Isotherms

- A priori knowledge of velocity profiles is required in order to determine dispersion coefficients for fluid flow through a packed bed.
- Radial variations of concentration for constant pattern flow in a packed bed with a nearly linear isotherm are small compared to those in the axial direction, making the cross-sectionally averaged concentration indiscernible from the solution to the plug-flow model.
- The mixing-cup concentration moves slightly ahead of and behind what a simple plug-flow model predicts, and is based on the magnitude of the perturbation parameter in the velocity profile and the first order correction term.
- Radial gradients of the fluid-phase concentration will form based on the shape of the velocity profile, which influence the breakthrough behavior at the bed outlet, causing nonuniform breakthrough to occur across the bed outlet. However, transverse dispersion attenuates this effect in comparison with the extent of the deviations from plug flow in the velocity profile.

Dehydration of Gas Streams Using Shell and Tube Membrane Modules

- The Nafion® membrane remained intact and showed no degradation in integrity after being subjected to a pressure gradient of 133.3 kPa.
- Tube-side feed streams are successfully dehydrated when a vacuum is applied to the shell side in lieu of a purge stream.
- Relationships previously reported for the diffusion coefficient of water through Nafion® membranes overestimate the transport of water through the membrane when a vacuum is used on the shell side due to decreased hydration levels of the membrane.

- Fluid-phase interfacial resistances do not impact the rate of water transport through the membrane, which is instead affected by diffusional rate limitations of the membrane itself.

- Maldistribution of the purge gas on the shell side greatly reduces the performance of the membrane module when operated in a counter-current fashion.

- Degradation in dehydration performance of the counter-current shell and tube membrane module was found to occur as the value of the V_s/V_t ratio is decreased.

There are opportunities for portions of this work to be extended. My recommendations for future research are as follows:

Temperature Swing Adsorption Compression

- There is still a considerable amount to be learned regarding nonuniform heating of TSA beds. It would be useful to study and characterize the operation of a thermally integrated TSA bed composed of several sections of varying adsorbent.

Breakthrough Behavior of Fluids with Slightly Favorable Isotherms

- An extension to the study of the breakthrough behavior of nonplug flow through a packed bed exhibiting a constant pattern would be the use of an irreversible adsorption isotherm in the model. This would bound the model of breakthrough behavior in packed beds between two extrema.

Dehydration of Gas Streams Using Shell and Tube Membrane Modules

- It would be appropriate to study the effects that increased flow paths on the shell side through the use of baffles has on the dehydration performance of shell and tube Nafion® multi-tube membrane modules. Additionally, these modules should be tested in a vertical configuration.

- It would also be interesting to study the change in performance for Nafion® shell and tube membrane modules when the tubes are coiled around a solid core as previous research seems to indicate that the added centrifugal force has an impact on the water transport. See for example, L. Lium L. Li, Z. Ding, R. Ma, Z. Yang, Mass transfer enhancement in coiled hollow fiber membrane modules, Journal of Membrane Science, 264 (2005) 113-121.